Development of a Condition-Assessment Method of Deteriorated Bridge Decks Based on GPR Data and Structural Response

Dipesh Donda

A Thesis
In the Department of
Building, Civil, and Environmental Engineering

Presented in Partial Fulfillment of the Requirements
For the Degree of
Master of Applied Science
(Civil Engineering)

At Concordia University,
Montreal, Quebec, Canada

August 2021

CONCORDIA UNIVERSITY

SCHOOL OF GRADUATE STUDIES

This is to certify that the thesis prepared

By: Dipesh Pravinbhai Donda

Entitled: Development of a Condition-Assessment Method of Deteriorated Bridge Decks Based on GPR Data and Structural Response

and submitted in partial fulfillment of the requirements for the degree of

Master of Applied Science (Civil Engineering)

complies with the regulations of the University and meets the accepted standards with respect to originality and quality.

Signed by the Final Examining Committee:

______________________________ Chair
Dr. A. Bhowmick

______________________________ Examiner
Dr. A. Bhowmick

______________________________ Examiner
Dr. E. Erkmen

______________________________ Supervisor
Dr. A. Bagchi

Approved by

____
Dr. M. Nik-Bakht, Graduate Program Director

September 2, 2021 ______________________________
Dr. Mourad Debbabi, Dean of Faculty

ABSTRACT

Development of a Condition-Assessment Method of Deteriorated Bridge Decks
Based on GPR Data and Structural Response

Dipesh Donda

Bridges are at the heart of transportation systems connecting the roads to and between the mainlands. Thus, bridges are an integral part of the economic growth of any country. They are subjected to dynamic loads of the vehicles and the environmental effects. These loads cause stress and strain cycles causing its deterioration by initiating microcracking. The deterioration is then accelerated due to the chloride attack which causes the corrosion of the steel reinforcement resulting in cracking and delamination of concrete and ultimately leads to failure.

It is essential to analyze the bridge with its actual condition which is difficult with a visual inspection. This analysis can help in determining the degree of repairs needed and an approximate idea about its service life. The development of the Non-Destructive Test (NDT) methods helps assess the condition of the bridge without any kind of damage to the original structure. In the past few decades, the Non-Destructive Evaluation (NDE) with the help of Ground Penetration Radar (GPR) has gained popularity due to its ease in the evaluation of the larger areas such as bridge deck and parking lot in a shorter amount of time with sufficient training. The NDE using GPR for Structural Health Monitoring (SHM) has been still evolving with new improvements in its technology as well as the development of new methods for the analysis of its data. A positive step towards detecting the subsurface materials present in the cracks has been undertaken in this study. A methodology to detect the subsurface cracks/gaps in concrete using GPR has been developed here by preparing three concrete samples of dimensions 50 x 25 x 5 cm^3, 50 x 25 x 10 cm^3, and 50 x 25 x 20 cm^3 in the laboratory. The detection of reinforcement of 6 mm, 10 mm, 18 mm, 20 mm diameter, as well as a 21.8 mm Fiber Reinforcement Polymer (FRP) bar, are studied along with the detection of the air gap, water gap, and gap with the salt solutions of thickness 3 mm, 4 mm, 4.8 mm, 5.8 mm and 8.8 mm under the depth of 5 cm, 10 cm, and 15 cm. The amplitude values of these parameters are studied, and a comparison is made to check the ability of GPR to detect this material in cracks and/or delamination with changes in depths. This will be helpful in analyzing the GPR data with more reliability.

Along with this, a non-linear finite element model (FEM) of a bridge superstructure using a fiber element is developed. The FE model of the bridge deck is updated and analyzed using a GPR defect map. This procedure of model updating is less tedious than the previous method available in the literature and proves to be time-saving. This model updating procedure will prove to be helpful in estimating the capacity of the bridge and make a prediction for future deterioration with the help of NDE methods (here GPR).

ACKNOWLEDGEMENTS

This thesis is dedicated to my late grandparents. Thank you for believing in me and teaching me the values of life. Although being uneducated you valued it and allowed your grandchildren to pursue education. I give them all my respect and appreciation. I would also like to dedicate this thesis to my late cousin Anil.

I would like to express my deepest gratitude to my advisor, Dr. Ashutosh Bagchi, for his time, contribution, ongoing support, and advice, patience, assistance, as well as his moral support in helping me to graduate. I would like to give my sincere appreciation to Dr. Farzad Ghodoosi for allowing my work and make development to his project. I would like to show my appreciation and sincere thanks to Dr. Fawzi Latosh and Mr. Amjad Hossain for continuous support and guiding me. I would like to thank Mr. Alexander Tarussov for giving a practical knowledge to work with GPR and giving me some experience by allowing me to accompany for scanning a tunnel and a parking lot.

I would express my gratitude to wonderful colleagues Mohammed Abdul Rahman, Timir Baran Roy, Saikat Bagchi, and Amit Chandra for making this journey wonderful as friends. I would like to thank Ms. Azin Shakiba for allowing me to collaborate in her laboratory work. I would also like to thank Alexis Gosselin and Alexander McGilton the two amazing technicians at Concordia University for your continuous support.

At the last, special thanks to my parents, brother, sister, country, and friends for trusting and believing me. I want to acknowledge all their sacrifices and express my heartfelt gratitude.

TABLE OF CONTENTS

List of Tables

List of Figures

Chapter 1 Introduction

1.1 Introduction

The bridges are important for the economic growth of any country. They are one of the basic blocks of the transportation system which connects two roadways from water bodies, canals, over drainage bodies, crossing tunnels, etc. The National Highway System (NHS) of Canada has 38000 kilometers of road out of more than a million kilometers (two-lane equivalent) of the total road network. There are 8700 bridges in NHS, 60% of which are more than 30 years old. (Government of Canada 2015)

Due to the corrosion of reinforcing steel and the cracking and delamination of concrete, the load-carrying capacity of the bridge decreases. This increases the maintenance costs and decreasing the service life of the bridge (François and Arliguie 1999). The monitoring of the RC bridges is thus essential for conditional assessment and assessing its present capacity to carry loads (Tennyson et al. 2001). Earlier the conditional assessment of bridges was performed by visual inspection in various Bridge Management Systems (BMS) like MTQ, PONTIS, and BRIDGIT rating system. These visual inspections often result in an inaccurate condition assessment (Gattulli and Chiaramonte 2005). With the development of Non-Destructive testing methods (NDT) and evaluation methods (NDE), it has become comparatively easy to assess the condition of the bridge (Washer 1998). The Ground Penetration Radar (GPR) is an NDE method that uses electromagnetic waves for the evaluation of different materials present under the area of inspection (Daniels 2005). The use of GPR is one of the important methods for assessing the condition of underground pipes and in knowing about different materials present below the ground (Benedetto and Pajewski 2015). For reinforced concrete, the GPR amplitude is affected due to the presence of chloride and moisture. The detection of the cracks is an important aspect of the repairing and rehabilitation of an RC bridge deck. Attempts by researchers are made to detect the surface crack depths in concrete panels

(Yu and Vinayaka 2020). However, there is a lack of studies on GPR based assessment of subsurface crack and/or delamination containing air gap, water gap or a salt-solution.

1.2 Problem Statement

The challenges faced by the infrastructure engineers, researchers, and transportation authorities are the early-stage detection of defects in the concrete bridge decks as well as knowing the reduction in its capacity to carry further loads and their ability to perform satisfactorily. These objectives are explained briefly in the following sections:

1.2.1 Cracks in Reinforced Concrete Decks

The bridges are subjected to the dynamic loads of vehicles (Li 2005) and loads generated due to environmental effects (Yi, Li, and Gu 2010). These loads cause micro-cracks which then increase in length and width leading to deterioration in Reinforced Concrete (RC) Bridges. The harmful chemicals enter through these cracks leading to corrosion of reinforcement in concrete (François and Arliguie 1999). The use of de-icing salt is one of the major chemicals causing the deterioration of bridges in Canada and the northern states of the United States (Cusson, Lounis, and Daigle 2011). The chloride ions from this salt penetrate the concrete through the cracks and react with the reinforcing steel causing corrosion. This corroded steel rust has more volume than its parent composition thus increases pressure in the surrounding concrete. This increase in pressure leads to an increase in cracking in concrete along the length of reinforcement which leads to a spall of concrete. If left unchecked this could ultimately lead to failure in the bridge structure. Hence, the detection of cracks and/or delamination is important at their early stages of formation. It is not a general practice of considering the signal attenuation for the detection of cracks and/or delamination as any signal attenuation or amplitude change is interpreted with the rebar corrosion.

The presence of air, water, and/or salt-solution in cracks/delamination results in a significant change in amplitude values which is not considered in the current practice of GPR data analysis. The presence of corrosion, as well as the presence of delamination, changes the stiffness of the structure. The results obtained from the GPR data vary due to the presence of different materials in the cracks apart from the rebar corrosion, hence it is important to study these variances as the presence of delamination without rebar corrosion will have different reflection amplitude.

1.2.2 Steel Reinforced Concrete Decks

The use of GPR is done in assessing the condition of the bridge deck. From GPR test results the defect map of deterioration can be generated after processing the data. This result shows the amount of deterioration that occurred in the structure. These defect maps could be utilized to measure and predict the capacity of the bridge infrastructure (Ghodoosi et al. 2018). However, the methods which are available in the literature for the finite element modeling of the bridge superstructure require tedious calculations which are very time-consuming and more complex in nature.

1.3 Research Scope and Objective

The objective of this research is to bridge a gap between the assessment methods of concrete bridge decks using GPR test results and analyzing the actual condition of the bridge more accurately than the previously available methods. The GPR results obtained are a good source of information that could be useful in determining the actual capacity of the bridge by model updating. The scope of use of GPR for the detection of subsurface delamination and/or cracks in the concrete and the presence of air, water, and/or salt solution in it has been explored in this research. This objective of the research is achieved by designing a laboratory experiment to:

1. Analyze the amplitude of GPR due to attenuated signals caused by different diameters of rebars at different depths.

2. Analyze the amplitude of GPR due to attenuated signals caused by air, water, and salt solutions with varying gaps and depths.

3. Compare the amplitude values for rebar, air, water, and salt solution with different depths.

The GPR data obtained from the scanning of the bridge deck are interpreted subjectively by the decision-makers. In the past, depending on the percentage of the deteriorated area the decisions are made for the repairs and/or demolition of the bridge deck. Hence the need for structural modeling of the bridge is necessary to measure its capacity which provides an objective evaluation (Ghodoosi et al. 2018). However, the model updating from the literature has some limitation which needs to be addressed. This objective for the structural model updating is achieved here through the following tasks:

1. Study available model updating procedure for finite element model updating using GPR data.

2. Develop a more efficient and effective finite element model of the bridge superstructure with Non-Linear Fiber elements in SeismoStruct 2018.

3. Apply the deterioration from the defect maps to the bridge model.

4. Analyze this bridge model with the defects to obtain its capacity which will be helpful for planning and scheduling its repairs objectively.

1.4 Research Methodology

The three plain concrete slabs of dimensions 50 x 25 x 5 cm^3, 50 x 25 x 10 cm^3, and 50 x 25 x 20 cm^3 are prepared in the Structures lab of the Concordia University. The samples are placed one above the other with different combinations and placing, different sheets, rebars, make air, water, and a salt solution gap in order to simulate a crack between them comparative to the actual field conditions. The GPR is then used to scan the surface from the top of the sample. The ability to detect the presence of different materials in the concrete cracks using a GPR is studied in this research. The acquired knowledge from this lab experiment would be helpful to make some relation with the actual field results.

The Finite Element (FE) method has been used to model the bridge using the SeismoStruct software, where the superstructure elements are modeled with Non-Linear Fiber elements and it is analyzed to calculate its capacity. The analysis done here is a non-linear static pushover analysis to measure its capacity to withstand the load. The GPR maps obtained from the field can be utilized to understand the effects of deterioration on the capacity of the structure. The GPR defect map data is then applied to the FE model of the Bridge. After assigning the deterioration defects to the model by changing the sections of the elements, it is then analyzed with non-linear static pushover analysis. The results will give us information about the updated capacity of the bridge and its behavior under the serviceability conditions.

1.5 Thesis Overview

This thesis is divided into five chapters described briefly as:

1. The first chapter of this thesis contains a brief overview of the problem statement, research scope and objective, and research methodology.

2. The second chapter includes literature reviews of - (a) Deterioration procedure of the RC structures, (b) detailed procedure of chloride induce corrosion mechanism, (c) deterioration mechanism of RC bridge deck, (d) a brief overview of NDE methods, (e) in-detail explanation on GPR evaluation method, (f) review on experimental work using GPR, (g) details about the RC bridge superstructure understudy, (f) the finite element bridge model of the bridge available in the literature, (g) an overview on model updating procedure of RC structures using NDE, and (h) FE model updating of RC bridge deck using GPR data.

3. The third chapter includes the detailed methodology of the laboratory experimental arrangements used as well as the preparation of the FE model of bridge superstructure using fiber elements including its validation and calibration along with the model updating procedure using GPR defect map.

4. Chapter four of this thesis explains the results obtained from the laboratory experiment as well as from the Non-Linear analysis of the Deteriorated bridge superstructure.

5. The conclusions and further recommendations are briefly explained in the final chapter.

Chapter 2 Literature Review and Data Collection

2.1 Deterioration of Reinforced Concrete Structures

The deterioration mechanism of the concrete structure is due to the chemical effects of carbonation, sulfate, leaching, chloride attacks, corrosion of steel reinforcement, alkali-aggregate reaction while the physical effects are due to thermal cycles and freeze/thaw cycles; and mechanical process like fatigue, cracking, erosion and abrasion (Ellingwood 2005). The importance of the above-mentioned processes are described briefly and the chloride-induced deterioration in detail as follows:

2.1.1 Deterioration Caused by Carbonation

The process of carbonation occurs when the cement hydration products such as the calcium silicate hydrate (CSH) gel and calcium hydroxide react with the carbon dioxide present in the surrounding atmosphere and results in the formation of calcium carbonate (Ann et al. 2010). The carbonation of concrete itself does not result in deterioration of structural performance while it can enhance the compressive strength of concrete (Klemm and Berger, 1972). The deterioration in the structural performance of reinforced concrete begins when the carbonation reaches the depth of the rebar where it neutralizes the high alkalinity of the concrete pore solution and hydration products are dissolved, this results in the decrease in the pH and thus lowers the buffering capacity of the hydration. As a result, the passive film on the surface of the rebar gets damaged and with the increase in oxygen and moisture, the steel mass loss increases due to corrosion. The corrosion of reinforcing steel induces cracking and spalling of concrete cover and results in the reduction of the load-carrying capacity of the structure. All types of hydrates present in concrete including CSH are transformed due to carbonation. This results in a change in the void distribution in hardened cement and thus changes the strength and shrinkage of concrete (Akiyama et al. 2019). The rate of progress of carbonation is rapid in dry concrete, and corrosion of steel in wet concrete (JSCE, 2002).

2.1.2 Deterioration Caused by Chloride Attack

The chloride-induced corrosion of the reinforcement bars is the major cause of deterioration in reinforced concrete structures in chloride-rich environments (Akiyama et al. 2019). The bridge piers in a marine environment and the piers placed by the roadway are subjected to a spray of salt-containing water which results in chloride-induced corrosion (Engelund and Sørensen 1998). Whereas the concrete in the vicinity of the coastal line experiences chloride-induced corrosion due to the inland sea spray carried by the wind as far as 3 km (A. Neville 1995; K. A. T. Vu and Stewart 2000). One of the major causes of deterioration in the reinforced concrete bridge decks in North America is the use of deicing salts. The deicing salts are used to depress the freezing point of water in winter (Jones et al. 2020). As an example, 10 million tons of salt are used on highways each year in the United States (Broomfield 2007). In addition, one of the major causes of steel corrosion is the use of chloride-contaminated concrete. As an example, chloride-induced corrosion has deteriorated many concrete structures in Japan constructed with sea sand (JSCE 2002).

The chloride ion penetration into concrete is a complex process. The experimental and analytical investigations through comprehensive research show the effects of various influential parameters. These parameters include concrete composition, its microstructure and porosity, the amount of pore saturation, concrete cover depth to reinforcement, water-to-cement ratio, relative humidity, ambient temperature, free chloride content, concrete age, and binding capacity. There is interdependency and time dependency between some of these parameters because of the chemical reactions occurring in concrete over time (Papakonstantinou and Shinozuka 2013). Previous studies show wide ranges for steel bar corrosion rates due to the variety of factors determining the rate of corrosion, such as the environment, quality of concrete, crack width, concrete cover, and related uncertainties (Andrade and Alonso 1994; Andrade, Alonso, and

Gonzalez 1990; Hassan et al. 2010).

The alkaline solution contained in the pores of the hydrated cement paste protects the steel in sound concrete by forming a thin oxide film on the surface of the rebars (Bertolini 2008). When this passive film is removed or is damaged locally, corrosion initiation begins. Chlorides function as corrosion catalysts and are not consumed in the process, but they do accelerate the corrosion process. The passive layer of oxide on the steel breaks down as soon as the amount of chloride accumulates to a critical level at the reinforcement, and a localized attack can develop. Corrosion is a type of electrochemical reaction that involves anodic and cathodic half-cell reactions (Razaqpur and Isgor 2009). The iron in the steel gives up electrons at the anode, according to the half-cell reaction:

$$Fe \rightarrow Fe^{2+} + 2e^{-}$$

To maintain electrical neutrality, the electrons generated by the anodic process are consumed at the cathodic sites on the steel surface, along with water and oxygen. The cathodic reaction is as follows:

$$O_2 + 2H_2O + 4e^{-} \rightarrow 4(OH^{-})$$

Chloride ions can activate and form an anode on an exposed steel surface:

$$Fe^{2+} + 2Cl^{-} \rightarrow FeCl_2$$

$$FeCl_2 + 2H_2O \rightarrow Fe(OH)_2 + 2HCl$$

$Fe(OH)_2$ ferrous hydroxide can also be made by:

$$Fe^{2+} + 2OH^{-} \rightarrow Fe(OH)_2$$

as well as the formation of ferric hydroxide $Fe(OH)_3$:

$$4FeOH_2 + 2H_2O + O_2 \rightarrow 4Fe(OH)_3$$

Finally, it forms hydrated ferric oxide (also known as red rust):

$$2Fe(OH)_3 \rightarrow Fe_2O_3 \cdot H_2O + 2H_2O$$

The final corrosion product is $Fe_2O_3 \cdot H_2O$, however other iron oxides are also present. There is an electric potential for each half-cell reaction. The difference between the cathodic and anodic potentials causes an electric current, defined as corrosion current, to travel through the concrete pore solution, comprising the movement of ions (Papakonstantinou and Shinozuka 2013).

Chloride ions, water, and oxygen are used in the reactions for chloride-induced corrosion. These components must therefore be present in the concrete pores near the steel surface for corrosion to occur. Because oxygen cannot easily enter fully or completely saturated concrete, the rate of diffusion and availability of oxygen at the cathodic site controls the corrosion current in these conditions. Chloride-induced corrosion is frequently localized, indicating that the anodic and cathodic reactions have divided to form macrocells. This is owing to the process of chloride attack, as well as high levels of moisture (due to the hygroscopic nature of chlorides), which leads to low electrical resistance in the concrete and efficient ion transport (Papakonstantinou and Shinozuka 2013).

The volume of the various iron oxides is 2–6 times that of the original iron (Jaffer and Hansson 2009). The tensile capacity of the concrete is exceeded by the stress due to the rust which results in the cracking of concrete. Increased crack widths enable increased penetration of corrosive materials (e.g., water, air, and salts) and increase the rate of corrosion which can lead to delamination and ultimately spalling of the concrete around the steel bar. Finally, this process leads to serviceability degradation and structural performance deterioration (Akiyama et al. 2019).

Detailed chloride-induced corrosion mechanism is discussed in ***Section 2.2***.

2.1.3 Deterioration Caused by Sulfate Attack

Concrete cracking, spalling, increased permeability, and strength loss are all causes of sulfate attack. Concrete in sulfate-containing environments must therefore be resistant to sulfate attack over an extended period of time for satisfactory performance (Monteiro and Kurtis 2003). Chemical attacks due to sulfate can be divided into two categories based on their modes. One form occurs when cement hydrates and chemically aggressive compounds react and transform the hydrates into soluble chemicals, causing the concrete to deteriorate. Acids, inorganic salts, and corrosive gases, such as hydrogen sulfide and sulfurous acid gas (JSCE 2002), trigger this sort of chemical attack by reducing the strength of the matrix due to CSH degradation. Decalcification of the cement paste hydrates due to sulfate penetration, particularly CSH, or sulfate attack on CSH and CH in the presence of carbonate ions to create thaumasite. Thaumasite development is accompanied by a loss of strength, resulting in the change of hardened concrete into a friable mass due to the destruction of a large amount of the CSH. This reaction can happen with any form of sulfate salt and is accelerated by humid environments and cold temperatures (Tixier and Mobasher 2003).

The other mechanism is concrete deterioration caused by expanding compounds formed when cement hydrates in the concrete react with elements that trigger a chemical attack, resulting in compounds like ettringite. Sulfate salts are responsible for this chemical attack. Because of the low tensile strength of concrete, expansion strain caused by the creation of ettringite during sulfate attack can induce cracking and poor performance. Sewer systems, structures in hot spring resorts, chemical plants, acidic rivers and acidic/sulfuric soil areas, water treatment and water utilization facilities, where leaching of alkalis from concrete is induced by contact with soft water, structures exposed to seawater, and structures where deicing salts are applied and are all examples of such deterioration phenomenon (JSCE 2002).

2.1.4 Deterioration Caused by Alkali-Aggregate Reaction

The alkali-aggregate reaction (AAR) reduces the service life of concrete structures by reducing their durability. The AAR is one of the primary reasons for highway concrete structure deterioration. The AAR, according to Gillott and Asgeirsson 1975, can be split into three categories of reactions: alkali-silica, alkali-carbonate, and alkali-silicate. The AAR is a chemical reaction that occurs in the presence of water between alkali hydroxide in the concrete pore solution and specific silica-rich compounds within the aggregate to generate an expansive gel. Internal pressure builds up when the gel swells, causing the aggregate and paste matrix to crack. The AAR has structural implications in concrete due to two factors: first, the appearance or development of microcracks inside the concrete matrix, which has a negative influence on strength development over time; and second, the creation of restraining pressures against expansion inside the concrete mix or from internal and external confinement, which has a confining action (Kubat, Al-Mahaidi, and Shayan 2016). The type of aggregate and the kind of environment determine the speed of deterioration (Gjørv 2014). It can take as little as 2 to 5 years for faster-reacting aggregates, such as porous flint, to show indications of cracking, whereas slower reacting aggregates, such as sandstone, can take up to 10 to 20 years (Akiyama et al. 2019).

2.1.5 Deterioration Caused by Frost Attack

The water which enters through cracks in concrete expands when it freezes, this frost results in the degradation of concrete occurring over a long period of time from the freezing and thawing cycles. Microcracking, scaling, and pop-out usually occur at the concrete surfaces of frost-attacked structures. Microcracks and scaling also occur in situations where the quality of the concrete is weak, or air pockets have not been properly entrained. Sometimes, pop-outs are seen where the aggregate quality is low. The degree of degradation caused by frost attack is determined by numerous factors — namely, material-related factors such as the concrete mix proportions (e.g., cement content, air content, water-to-cement ratio) and aggregate quality; structure-related factors such as cross-section shape and steel reinforcement amount; factors associated with environmental situations under which structures are used, such as the extent of water supply, impact of insulation, temperature change (particularly the lowest and highest temperature), and frequency of freezing and thawing cycles (Akiyama et al. 2019). In many countries, this form of degradation still causes problems with durability (Gjørv 2014). Frost damage puts strain on the structural aesthetics while also degrading the mass transfer resistance of concrete. Steel corrosion can start earlier under the impact of frost attack in places where chloride attack and frost attack damage are an issue (JSCE 2002).

2.2 Chloride Induced Corrosion Mechanism of Reinforced Concrete Structures

The three stages of reinforcement corrosion progression can be easily recognized from this simple discussion of the corrosion process: cracking of concrete at an early age, the corrosion initiation period, the rust permeation or crack initiation period, and the crack propagation phase (Cusson, Lounis, and Daigle 2011). The initiation period is the amount of time it takes for chlorides from the environment to reach the reinforcement level, pass through the concrete cover, and accumulate in sufficient quantities to break the protective passive layer on the steel surface and commence active corrosion. During this period, no damage is expected to occur. The time it takes for rust to form and generate the required internal stresses that lead to cover concrete cracking is defined by the crack initiation period, and the crack propagation stage, undeniably, is defined by the crack expansion process, which is usually described in terms of cover crack width expansion (Papakonstantinou and Shinozuka 2013). ***Figure 1*** shows corrosion of reinforced concrete members due to chlorides.

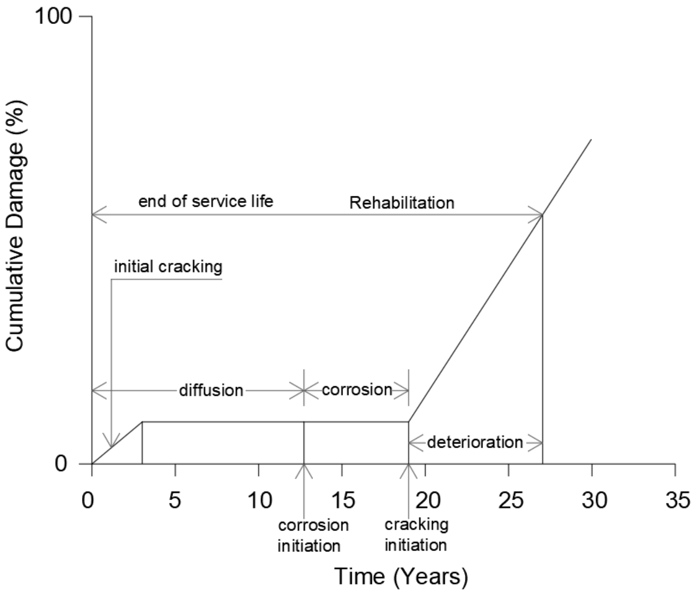

Figure 1: *Chloride Induced Deterioration of RC Member - Adopted from (Y. Liu and Weyers 1998)*

The chloride diffusion analysis can be used to determine the quantity of penetrated chloride content through the protective cover depth (Oh, Lew, and Choi 2007). Furthermore, when the chloride content around the reinforcement surpasses a certain threshold, steel bar corrosion begins, resulting in concrete deterioration and a decline in bridge deck performance (Masi et al. 1997). The following five parameters have the greatest impact on a service life prediction of the steel-reinforced concrete deck: the surface chloride content of the concrete (C_s), the concrete permeability represented by the effective chloride diffusion coefficient (D_c), the threshold concentration of chloride at the reinforcement (C_{th}), steel rebar corrosion rate (λ), and the steel reinforcement concrete cover (Cusson, Lounis, and Daigle 2011). These variables are extremely unpredictable both in space and over time, unpredictable to measure and estimate, and difficult to identify (Ghodoosi et al. 2018). The appropriate field data for those locations with similar environmental conditions as Canada, where a significant amount of deicing salt is used during the long and cold winter seasons, are selected from the literature in this thesis. The surface chloride concentration has a greater impact on the structural service life than the chloride content threshold value (Khatri and Sirivivatnanon 2004). In this thesis, the model to calculate the diameter of the rebars due to chloride induced corrosion are discussed below through the corrosion initiation period and corrosion propagation. The calculations involved in this thesis for corrosion initiation are given in ***Appendix C***.

2.2.1 Corrosion Initiation Period

When the chloride concentration at a depth equal to the cover depth reaches a threshold or critical value, this is the time of initiation of corrosion (Guo et al. 2006). Fick's second law of diffusion which is a simpler one-dimensional model is often used to model the chloride diffusion in the reinforced concrete structures (Papakonstantinou and Shinozuka 2013). At a distance of x depth from the surface, the chloride content $C(x,t)$ is given by the following equation:

$$\frac{\partial C(x,t)}{\partial t} = \frac{\partial}{\partial x}\left(D_C \frac{\partial C(x,t)}{\partial x}\right) \qquad \textit{Equation 2.1}$$

This equation changes to the following after applying the boundary conditions $C(0,t) = C_s$ i.e., the surface chloride content and $C(x,0) = 0$:

$$C(x,t) = C_s\left[1 - erf\left(\frac{x}{2\sqrt{t\,D_c}}\right)\right] \qquad \textit{Equation 2.2}$$

The error function (*erf*) is twice the cumulative distribution of a normal distribution with a mean of zero and variance of 0.5 which is given by the following equation:

$$erf(\omega) = \frac{2}{\sqrt{\pi}} \int_0^{\omega} e^{-x^2}\, dx \qquad \textit{Equation 2.3}$$

The protective passive layer around the reinforcement will be dissolved when the chloride concentration reaches its critical threshold (C_{th}), and the steel reinforcement corrosion process will initiate. The time to corrosion initiation (t_i) of the steel reinforcement will be obtained from ***Equation 2.2*** by replacing the threshold value of chloride concentration.

For the New York state, the maximum value of surface chloride content of concrete C_s is 8.8 kg/m^3 (Weyers 1998). This value is used as the C_s in this thesis for the calculation of the time of corrosion initiation. The effective chloride diffusion constant, D_c, corresponding to the above level of C_s, is 84 mm^2/year (Weyers 1998). For the computations in this thesis, the chloride diffusion coefficient is considered as a single (mean) value. However, depending on the concrete used, this parameter might vary significantly, and hence has an impact on the time it takes for the chlorides to reach the reinforcement (Ghodoosi et al. 2018). The permeability of concrete or the water-cement ratio should be used to calculate this coefficient. Most models assume it is constant for convenience, but it can change with time (Ghodoosipoor 2013). The critical chloride concentration that causes the protective passive coating around the steel reinforcement to dissolve is known as the chloride threshold, C_{th} of the reinforcements. The most commonly used value for the C_{th} is 0.71 kg/m^3 (Weyers 1998). For the computations in this thesis, this value of the chloride threshold of steel bars is used. This parameter, on the other hand, might vary based on the steel type and amount of cement used in the concrete, and thus has an impact on the time it takes for chlorides to reach the threshold value (Ghodoosipoor 2013).

2.2.2 Time to Crack Initiation

It is the period of time between the start of corrosion and the appearance of the first apparent crack of about 0.05 mm. Many investigations have demonstrated that crack initiation happens quickly once corrosion begins, but it takes a considerable time for a crack to spread to the limit crack width (Mullard and Stewart 2009). The critical amount of corrosion products, which consists of the amount of corrosion products needed to fill the interconnected void space around the reinforcing bar plus the amount of corrosion products needed to generate sufficient tensile stresses to crack the cover concrete, is usually considered in the calculation of a time to corrosion cracking (Liu and Weyers 1998).

For a constant corrosion rate the time-to-cracking after initiation of corrosion is given by the equation below (Liu and Weyers 1998):

$$t_{cr} = \frac{W_{crit}^2}{2\,k_p} \qquad \textit{Equation 2.4}$$

where, k_p = rate of rust production, and

W_{crit} = the critical amount of corrosion products

$$k_p = 0.098\left(\frac{1}{\alpha}\right)\pi D i_{cor} \qquad \textit{Equation 2.5}$$

In which $\boldsymbol{\alpha}$ is the ratio of molecular weight of steel divided by the molecular weight of corrosion products, D is the diameter of steel rebar (mm) and i_{corr} is the annual mean corrosion rate (mA/ft^2). The W_{crit} can be calculated by the following equation:

$$W_{crit} = \rho_{rust}\left(\pi\left[\frac{C\,f_t'}{E_{ef}}\left(\frac{a^2+b^2}{b^2-a^2}+\nu_c\right)+d_o\right]D+\frac{W_{st}}{\rho_{st}}\right) \qquad \text{Equation 2.6}$$

where ρ_{rust} is the density of the corrosion products, C is the concrete cover depth, f_t' is the tensile strength of the concrete, E_{ef} is an effective elastic modulus of the concrete, ν_c is Poisson's ratio of concrete, d_o is the thickness of the pore band around the concrete/steel interface, W_{st} is the amount of steel corroded, ρ_{st} is the density of steel, $a = (D + 2d_o)/2$ is the inner radius of a thick-walled concrete cylinder, and $b = C + (D + 2d_o)/2$ is the outer radius of a thick-walled concrete cylinder. The E_{ef} is given by the following equation:

$$E_{ef} = \frac{E_c}{(1+\varphi_{cr})} \qquad \text{Equation 2.7}$$

where E_c is the elastic modulus of the concrete and φ_{cr} is the creep coefficient of the concrete.

Hence the time of cracking (t_{1st}) from after the completion of the structure is

$$t_{1st} = t_i + t_{cr} \qquad \text{Equation 2.8}$$

2.2.3 Time to Crack Propagation

It is the amount of time it takes for a crack to propagate from the first visible crack (0.05 mm) to the limit crack width (t_{ser}) (Mullard and Stewart 2009). For cracks, up to 1 mm in width, an empirical model developed by Vu et al. 2005 to estimate the time to excessive cracking for RC structures subjected to corrosion is presented (K. Vu, Stewart, and Mullard 2005) in this thesis.

The equation to estimate the time for cracks to propagate to a limit crack width of reinforced concrete is given below (K. Vu, Stewart, and Mullard 2005):

$$t_{ser} = k_R \times 0.0114\, i_{corr(real)} \left[A \left(\frac{C}{w_c}\right)^B\right] \textit{(years)} \qquad \textit{Equation 2.9}$$

where $i_{corr(real)}$ is the actual corrosion rate (μA/cm^2), A and B are constants, C is the clear concrete cover (mm), w_c is the water-cement ratio, k_R is the rate of the loading correction factor.

$$k_R \approx 0.95 \left[exp\left(-\frac{0.3\, i_{corr(exp)}}{i_{corr(real)}}\right) - \frac{i_{corr(exp)}}{2500\, i_{corr(real)}} + 0.3\right] \qquad \textit{Equation 2.10}$$

where $i_{corr(exp)}$ is the accelerated corrosion rate.

2.2.4 Severe Cracking Time

It is the time (t_{sp}) it takes for concrete surface cracking to achieve a limit crack width (usually 1 mm) since corrosion initiated, and it equals the total of crack initiation (t_{1st}) and cracks propagation (t_{ser}).

$$t_{sp} = t_{1st} + t_{ser} = t_i + t_{cr} + t_{ser} \qquad \textit{Equation 2.11}$$

2.2.5 Reinforcement Corrosion

To estimate the decrease in steel bars, many models have been presented. All of the models suggested fall into one of two categories: uniform corrosion models and pitting corrosion models. The uniform corrosion model implies that the corroded rebars' geometrical cross-section will remain the same as a circular cross-section. A uniform corrosion model is adopted in this thesis for convenience.

The deteriorating process caused by reinforcement corrosion is expected to result in a uniform decline in the bar diameter of the reinforcing steel D_t which is given by the following formula (Stewart and

Rosowsky 1998a):

$$D_t = \begin{cases} D_i & ; t \leq T_i \\ D_i - 2\lambda(t - T_i) & ; T_i \leq t \leq T_i + \left(\frac{D_i}{2\lambda}\right) \\ 0 & ; t > T_i + \left(\frac{D_i}{2\lambda}\right) \end{cases} \qquad \textit{Equation 2.12}$$

Where D_i is the initial bar diameter, T_i is the time of corrosion initiation, λ is corrosion rate at the surface of rebar, and i_{corr} is the corrosion current density.

A governing parameter is the current density i_{corr} proportional to corrosion. A uniformly distributed random variable with a mean value of $i_{corr} = 1.5$ µA/cm^2 for the current density was proposed by (Stewart and Rosowsky 1998a). The corrosion rate could be expressed as $\lambda \approx 0.0116 \bullet i_{corr}$ mm/year if steel reinforcement corrosion results in a consistent decline in bar diameter. In this thesis considering the values of $i_{corr} = 1.5$ µA/cm^2, the corrosion rate would be $\lambda = 0.0174$ mm/year.

2.3 Deterioration Mechanism in Reinforced Concrete Bridge Deck

It is critical for the well-being of humanity to maintain and secure reliable infrastructure for everyday usage. With the aging of the structures, operation and maintenance have grown particularly complex. Health monitoring is the process of evaluating and tracking structural integrity and analyzing the extent of deterioration in a structure (P. C. Chang, Flatau, and Liu 2003). Much has been done in the past in terms of infrastructure monitoring, inspection, maintenance, and design code standards. For example, in the USA, almost 600,000 bridges are examined every two years and rated based on their condition (Pines and Aktan 2002). The Federal Highway Administration established a rating system (0–9) for bridges, with 9 being a freshly completed bridge and 0 representing a failed bridge. More than 40% of national bridges are structurally poor or non-functional, according to this assessment (Pines and Aktan 2002). Furthermore, the average bridge life in the United States is 42 years, despite the fact that bridges are intended and built to last at least 50 years (Herrmann 2013). As a result, there is a critical need for concrete bridge health monitoring and maintenance (Pines and Aktan 2002).

Shrinkage, vehicle loads, and corrosion can all cause deterioration. Concrete must be able to shrink freely as it dries, but this is impossible with RC decks due to the restraint imposed by the longitudinal girders. The elastic strain of the concrete deck will be increased due to the restricted shrinkage. Furthermore, additional tensile stresses will arise in the concrete decks as a result of dynamic loads from vehicles. The concrete will crack as a result of the tensile strains caused by both shrinkage and traffic. First, transverse cracks will appear in the deck, causing it to function as a one-way beam that will break as traffic loads increase (Oh, Lew, and Choi 2007).

When water and oxygen are present, the mechanism of deterioration caused by chloride attacks is dependent on location to occur. In the beginning, chloride ions penetrate the concrete cover at a pace that varies depending on the quality of the concrete and the surrounding conditions. Due to the alkaline nature of concrete, a thin passive coating of oxide forms to protect the steel reinforcement bars in concrete from corrosion. When the chloride concentration reaches a certain level, however, the passive layer is destroyed. When the passive layer is gone and oxygen and water are present, corrosion begins. Around steel bars, a rust layer will develop. Due to its large volume of rust than the original steel, such a rust layer (ferrous hydroxide) would extend the outer surface of the steel, increasing internal tensions in the concrete and resulting in longitudinal cracks. These cracks will spread, causing the concrete to spall (A. M. Neville 1996).

It is well known that corrosion of reinforcement and/or spalling of the concrete cover can result in a loss of strength and serviceability by lowering the area of steel bar or bond (Stewart and Rosowsky 1998b).

Corrosion of steel bars reduces moment strength as the cross-sectional area of the reinforcing bar reduces. (MacGregor, Mirza, and Ellingwood 1983) examined a probabilistic forecast of rebar area loss, finding that roughly 70% of rebar area will be lost due to corrosion after 20 years of service. As a result, the nominal moment strength has been decreased by 50%.

2.4 Non-Destructive Evaluation Methods

In highway bridges, concrete deterioration, steel corrosion, changes in boundary conditions, and the weakening of structural connections with time are all serious challenges. If a damaged bridge is not repaired, the structural integrity and serviceability of the bridge will deteriorate over time (Islam et al. 2014). As a result, regular inspections and health monitoring of highway bridges are necessary. The health monitoring of structures, particularly bridges, may be divided into two categories: global and local health monitoring. Only the occurrence of deterioration is recognized in global health monitoring, whereas the extent, location, and degree of damage are determined in local health monitoring (P. C. Chang, Flatau, and Liu 2003). For the safe and sound functioning of infrastructures, both global and local health monitoring approaches are necessary (Rehman et al. 2016). Engineers and owners can use nondestructive testing (NDT) and nondestructive evaluation (NDE) to evaluate and monitor aging structures quickly and effectively. These approaches are used to identify damage and to monitor the health of structures on a local level. Furthermore, NDT can prevent structures from collapsing unexpectedly and prematurely (Rehman et al. 2016).

NDT techniques are employed in the construction sector for the following reasons, according to ACI 228.2R-98 (American Concrete Institute 2013): (i) new construction quality control, (ii) correcting the complications, (iii) existing structure condition evaluation, and (iv) repair operations quality assurance.

Non-destructive tests are categorized into five parts based on test sources, test type or technique, and test purpose. Based on the test sources NDT techniques are classified as (Rehman et al. 2016):

i. The audio-visual methods include visual inspection, chain dragging, and coin tapping.,

ii. The stress-wave methods include acoustic emission, impact echo, sonic test based on stress waves, Ultrasonic Pulse Velocity (UPV) method, and Impulse Response (IR).

iii. The Ground Penetrating Radar (GPR), Electromagnetic conductivity technique, Half-cell potential test, Infrared Thermography, and Electrical Resistivity (ER) measurement are the Electromagnetic methods.

iv. The deterministic methods comprise of proof load test and core cutting (semi-destructive method).

v. Other methods include dynamic/vibration testing, and radiography (nuclear NDT).

The Non-Destructive Evaluation procedures used in Structural Health Monitoring to identify interior voids, gaps, and cracks which can also be used to detect concrete delamination are metal tapping, chain dragging, infrared thermography, electromechanical sounding, ground-penetrating radar (GPR), and impact echo.

The choice of an NDE method employed for a specific structure depends on the cost of operation, area to be covered, the time required, level of desired accuracy, reliability, and simplicity (Jana 2007; Rehman et al. 2016). In an ideal world, a method that can identify all significant flaws and abnormalities in the structure would be used. As a result, the technique of NDT must be chosen depending on the information desired (Rehman et al. 2016). Metal tapping and chain dragging are more prevalent among the others, particularly when investigating localized delamination (e.g., a warehouse floor or a parking structure). Delamination in a petite region can be detected using impact echo (e.g., in a concrete core). Infrared thermography is helpful in a laboratory specimen where the sample can be preheated or in the field on a clean, debris-free surface on a bright sunny day with substantial temperature differences. Unlike all of these methods, which are unable to detect internal flaws beneath the first layer of delamination, GPR can detect multiple layers of defects across the entire thickness of a concrete member. With further technological advancements and adequate training, GPR can be successfully used to detect delamination over many large structures, including bridge decks (Jana 2007). The Ground Penetrating Radar evaluation method is used in this thesis and is explained in detail in the next section.

2.5 Ground Penetrating Radar (GPR) Evaluation Method

The identification of buried utilities was one of the earliest GPR investigations in civil engineering (Caldecott et al. 1988; Morey 1974; Osumi and Ueno 1988). Simultaneously, several early pavement applications were reported (Hironaka, Hitchcock, and Forrest 1976; Kovacs and Morey 1983). The number of applications and advancements of the methodology has expanded dramatically since these early works. GPR has shown to be an effective technique in the study of a wide range of structures and infrastructures, and it is currently used in a huge number of situations: road and pavement analysis, void and cavity identification, bridge and tunnel research, assessment of the actual building and cultural property, archaeological surveys, forensics and mine detection, geotechnical assessments, and water management analysis. In many situations, GPR testing is used in conjunction with other NDT techniques (Pérez-Gracia 2016).

GPR is the most popular and widely used non-destructive test for bridge decks and pavements (Alani, Aboutalebi, and Kilic 2013; American Concrete Institute 2013; Barnes, Trottier, and Forgeron 2008; Solla et al. 2012; S Yehia et al. 2014). GPR provides an electromagnetic (EM) wave-reflection survey. GPR is a fast and accurate method for determining the in-depth characteristics of subsurface layers, and it can be used to detect damages, voids (more than 1 in. deep and 1 in. diameter) (Sherif Yehia et al. 2007), cracks, and their lengths, cavities, delamination, recognizing steel reinforcement and its diameter (Diamanti, Giannopoulos, and Forde 2008), member thickness, identifying regions of high moisture content, layer settlement, and strain-induced deformation (Alani, Aboutalebi, and Kilic 2013; Cantor 1984; Orlando, Pezone, and Colucci 2010; Pérez-Gracia, García, and Abad 2008).

2.5.1 Principle of GPR

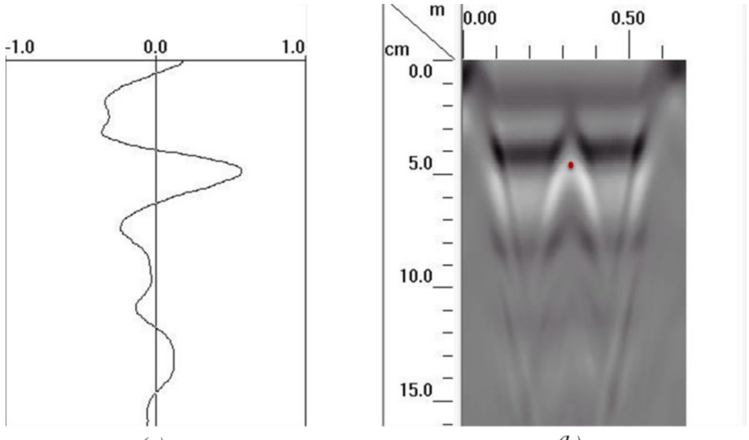

(a) (b)

Figure 2: *GPR Data (a) A-Scan and (b) B-Scan*

A geophysical approach based on the transmission of a very brief electromagnetic pulse (1–20 ns) in the frequency region of 10 MHz–5 GHz is known as ground penetrating radar (ASTM D6432 2019; Pérez-Gracia 2016). An antenna, a control unit, a display unit, and a data recording device are all common components of a GPR (American Concrete Institute 2013). A transmitting antenna sends an electromagnetic pulse into the surface, which is partially reflected and partly transmitted into deeper layers when it contacts substances with various dielectric characteristics. The reflected signal (trace or A-Scan) is then registered from a receiving antenna, which can be either separate or in the same antenna box as the transmitter where, in plot X-Y, X represents the amplitude while Y represents the time. ***Figure 2(a)*** shows an A-scan of GPR data which is the amplitude obtained at the peak of the hyperbola of the B-scan. A B-scan is created by averaging such A-scans throughout the whole length of a bridge section and recording them at regular intervals which gives reflected signals in X-Z representations in which, the antenna movement along the survey line is shown by the X-axis, and the two-way travel time of the pulse emitted is represented by the Z-axis (Pérez-Gracia 2016). ***Figure 2(b)*** shows a B-scan of rebar in GPR data. Scans generated by moving the antenna(s) over the ground's surface are overlapped in orthogonal directions to form a radar profile known as a C-Scan which is a planar view of the GPR data. Another image called a D-scan image could be generated by imaging the data points gathered at the same time by all of the antennas. A multichannel GPR system can be helpful for obtaining such D-scan which is the 3D GPR data (Kim et al. 2021).

2.5.2 Velocity and Two-Way Travel Time of GPR Signal

The time taken by the electromagnetic pulse of the radar from the transmission to receiving back by antenna after getting reflected from the media interface is known as two-way travel time (TWTT). A GPR trace is the record of the amplitude of EM energy that has been reflected and reported as a function of two-way travel time from interfaces between materials with distinct EM properties (ASTM D6432 2019). Part of the electromagnetic energy is reflected when a propagating electromagnetic radar wave hits a discontinuity in the electromagnetic (EM) characteristics of the medium. The dielectric properties of natural and constructed materials are mainly attributed to the characteristics that control the propagation and loss of electromagnetic waves through such materials. Materials' electrical conductivity (σ), magnetic permeability (μ), and dielectric constant or relative permittivity (ε) are all examples of EM characteristics. These characteristics are essential factors that can affect how a radar wave propagates, reflects, and attenuates across various mediums (Pérez-Gracia 2016). This dielectric constant of material varies considerably with the temperature, density, water content, frequency, salinity, and other conditions (ASTM D6432 2019). Electromagnetic properties of concrete depend on porosity, water content, age, and frequency of the waves. The relative permittivity (ε) of the concrete ranges from 5 to 10 and the Wave Velocities ranges from 0.095 - 0.134 m/ns (ASTM, 2019).

Using the following relationship, the propagation speed through the material can be estimated (ASTM D6432 2019).

$$\mathrm{v} = \mathrm{c}/\sqrt{\varepsilon} \qquad \textit{Equation 2.13}$$

where c is propagation velocity in free space (3.00×10^8m/s), v is propagation velocity through the material, and ε is the relative permittivity or dielectric constant of the material.

If the time it takes for an electromagnetic pulse to travel from the transmitting antenna to the reflector in the ground and back to the receiving antenna is measured, and the velocity of that pulse in the subsurface medium is known, and the depth of the material can be calculated. To convert two-way travel times into depths, for a given velocity (υ) in a medium with measured two-way travel time (t) the following equation can be used (Pérez-Gracia 2016):

$$\mathrm{d} = \upsilon\ \frac{\mathrm{t}}{2} \qquad \textit{Equation 2.14}$$

2.5.3 GPR Classification

GPR system is classified into three types based on the type of antenna used for data collection (ASTM D6087 2015; ASTM D6432 2019; Pérez-Gracia 2016):

i. Air- Launch Antenna system: Uses air-launched horn antennas with center frequencies 1 GHz and 2 GHz. It can operate at high speeds as it is mounted on a mobile vehicle. Antennas are usually elevated 0.3 - 0.5 m off the ground. Their penetration depths are about 0.9 and 0.75 meters, respectively, and they have been extensively investigated as a pavement quality tool (Lahouar and Al-Qadi 2008; Saarenketo and Scullion 2000) and in railroad inspection (Loizos and Plati 2007).

ii. Ground-Coupled Antenna system: Uses ground-coupled antenna with central frequencies ranging 10 MHz - 4 GHz. When compared to air-coupled systems, ground-coupled systems offer significant benefits, such as improved signal penetration and vertical resolution. These antennas should keep contact with the surface or be suspended slightly above it to provide a better performance, which lowers data collecting speed to around 5 - 30 km/hr depending on the configuration. These antennas offer a wide variety of uses such as detection of reinforcing bars in concrete (Sbartaï et al. 2012), to geological applications, such as the analysis of materials and structures in volcanic areas (Gómez-Ortiz et al. 2007).

iii. Bore-hole antenna system: GPR examinations of deeper formations, such as fracture classification, foundation examinations, cavity and crack identification, and tunneling inspection, are all done using this technology (Pérez-Gracia 2016).

In the monostatic mode, a single-dipole antenna can be used to both send and receive signals. For transmitting and receiving, the bi-static mode uses different antennas. These antennas may be located in a single enclosure where the distance is constant between the two antennas or indifferent enclosures where it is possible to adjust the distance between the two antennas. Usually, in two antenna structures, both the antennas have the same direction and polarization, but often the receiver antenna is oriented perpendicular (orthogonal) to the transmit antenna with its electric field, resulting in insensitivity to reflection from horizontal layers and linear characteristics (such as wires, cables, rebars or pipes) that are aligned with either antenna, but high sensitivity to off-alignment linear elements (ASTM D6432 2019).

For reinforced concrete, the ability to map the rebar will be maximized by aligning antennas with the rebar in concrete, but alignment perpendicular to the rebar will eliminate scattering reflections from the rebar, to see through or past the rebar to get the concrete thickness. The response of horizontal layers is minimized by cross-polarized antennas (perpendicular to each other) (ASTM D6432, 2019).

2.5.4 Frequency Selection

The transmitting antenna frequency is an essential factor in determining the depth range of penetration. The antenna frequency used in a GPR survey should be carefully selected since there is a balance to be made between a low-frequency antenna that provides deeper signal penetration but worse resolution and a higher frequency antenna that provides greater resolution but shallower penetration (Pérez-Gracia 2016). The antenna frequency selection depends on the penetration depth, the spatial resolution, and the portability of the system employed in the analysis (ASTM D6432 2019). Antennas having a better signal-to-noise ratio and broader bandwidth are preferred for both greater penetration depth and higher resolution. Most high-frequency antennas are shielded to have less noise in recorded data whereas low-frequency antennas are rarely shielded (less than 100 MHz) (ASTM D6432, 2019).

2.5.5 Modes of Operation

The basic model of operation for the radar study is determined by the aim of the study. In radar surveys, two modes of operation are typically used, and both are referred to as the reflection profiling method while the third mode is used very little (ASTM D6432, 2019).

i. Data is acquired in the first mode, as the antenna(s) are towed along the survey line.

ii. In the second mode, both with fixed transmitter/receiver separation, the radar data is collected at particular points along the survey line.

iii. The third mode that is rarely used is the accumulation of common midpoint (CMP) data at points along with the profile (varying transmitter-receiver separation). By collecting data on a grid, a three-dimensional perspective view can be built.

2.5.6 Amplitude and Attenuation

The transmitted wave travels through media until it hits dielectric discontinuities, at which portion of the energy is reflected and the trace (radar-wave including all depth reflections) is recorded by the receiving antenna. The amplitude value is used to describe the strength or intensity of the reflection. The larger the dielectric difference between two distinct mediums, the higher the amplitude. Every trace is recorded independently. The control unit, on the other hand, may process all of the individual traces (A-Scans) into a 2D picture (B-Scan or radargram). It is done by applying a color palette to the amplitude values that have been recorded. A greyscale color palette is shown in ***Figure 2(b)***, with the black color representing the smallest amplitude and the white color representing the highest amplitude. The intermediate values are transformed into distinct tonal grey shades. The strength of the field reflected on the discontinuities, the distance between the target and the antenna, and the EM magnetic characteristics of the medium all influence the amplitude of the received signal. The first parameter determines the amount of energy that will travel to the antenna after it has been reflected. The second aspect controls the wave's attenuation as a function of geometrical spreading. The third component, which is dependent on the frequency of the wave, causes the energy to be attenuated owing to absorption and conversion into heat (Pérez-Gracia

2016).

The widely used method for GPR data analysis is amplitude analysis. GPR equipment is used to measure the amplitudes of the profiles at the asphalt-concrete interface, top and/or bottom reinforcing bar layer, and slab bottom (Dinh et al. 2014). The ASTM D6087 standard outlines a method for creating degradation maps using amplitude values (Tarussov, Vandry, and De La Haza 2013). There are two different accepted methodologies of GPR data processing based on the amplitude of reflection. The first method, the attenuation technique of bottom deck reflection, measures deterioration based on the relative amplitudes of reflection from the bottom of the bridge deck relative to the surface of the bridge deck. In order to determine deterioration in the second process, the top reinforcing reflection attenuation technique utilizes the relative reflection amplitudes from the top layer of reinforcing (ASTM D6087 2015).

The reflections at the concrete-rebar boundary provide a characteristic hyperbolic signature. The apex of these hyperbolas corresponds to the position of the rebar in the concrete bridge deck (Krause et al. 2007). The amplitude values are selected at the peak of these hyperbolas to evaluate the degree of concrete deterioration. Benedetto (2013) developed a technology that uses amplitude values to identify moisture content and may be used as a preventive approach to detect corrosion and delamination in the early stages.

Electrical conductivity, dielectric and magnetic relaxation, scattering, and geometric spreading losses all contribute to the attenuation of radar signals. The quantity of water in the substance and the concentration of free ions (salinity) in the solution are the primary determinants of conductivity. When inhomogeneities in the ground scatter EM radiation in unexpected directions, attenuation occurs. Scattering can be severe if the magnitude of inhomogeneity is proportional to the wavelength of EM radiation (Olhoeft 1984).

Various medium interfaces, such as concrete/rebar, concrete/air, and concrete/water, will display different positive amplitude values at the same depth due to the differentiating EM characteristics of these material interfaces (Donda et al. 2021). The above principles are applied to the tests conducted in our lab, and conclusions are derived based on the differences in amplitude values.

2.5.7 Advantages of GPR

The following are the major benefits of the GPR method: (i) it is non-destructive and non-invasive when compared to other geophysical approaches, (ii) the data collecting is quick, (iii) vertical and horizontal resolution is precise, (iv) its transport is simple, (v) results are shown in real-time, and (vi) high-resolution imaging of the subsurface is possible (Pérez-Gracia 2016).

2.5.8 Disadvantages of GPR

Nonetheless, despite its potential, this technology has limits. Signal attenuation, data interpretation difficulties, reflection multiples and diffractions, ringing noise, and X-marks on spots caused by a long wire in the vicinity are some limitations of the GPR (Pérez-Gracia 2016). Because this test generates a huge quantity of data, an expert interpreter/analyst is necessary (Rehman et al. 2016).

2.6 Review on Experimental Work using GPR

The use of Ground Penetrating Radar (GPR) in the Non-Destructive Evaluation (NDE) of structures has significantly increased in the past decades. Several attempts are made by the researchers to detect the surface and subsurface deterioration of the concrete using GPR. The explanation below provides brief literature on the development of methods by researchers for detection of size, location, and depth of rebar, corrosion of rebar, effects of chloride-induced corrosion, change in amplitude and frequency due to corrosion, the detection of hyperbolas with image processing, and the use of neural networks for the analysis of GPR data.

Researchers have tried to: measure the radius of steel rebar in concrete by measuring power reflectivity (C. W. Chang, Lin, and Lien 2009), detect the rebar size in an oil/water emulsion tank with different orientation of antennas (Shaw et al. 2003), locate the rebar and estimate its cover thickness (H. Liu et al. 2020; Wiwatrojanagul, Sahamitmongkol, and Tangtermsirikul 2017; Xiang, Ou, and Rashidi 2020), compare the amplitude and frequency of corroded and non-corroded reinforcement (Hong, Lai, and Helmerich 2015), quantitatively estimated three 16 mm diameter corroded rebar in an emulsion tank (Hasan and Yazdani 2016), quantified corrosion of rebar in a pre-corroded concrete slab for single rebar size (A Zaki et al. 2020), long term monitored reinforcement corrosion in rebar for a large concrete slab by inducing pitting corrosion in rebars at selected locations (Hong et al. 2017) using a Ground Penetrating Radar. Researchers in past have used the galvanostatic method of inducing corrosion of rebars in concrete to study corrosion-induced cracking (K. Vu, Stewart, and Mullard 2005), corrosion monitoring using the half-cell potential method (Wilson and Yu 2013), compared the galvanostatic method with the artificial climate environment method (Yuan, Ji, and Shah 2007). (Ahmad Zaki et al. 2018) tried to assess rebar corrosion of four 20 mm diameter rebar by using the galvanostatic method to induce corrosion by passing electric current in an in-situ concrete slab using a GPR. The detection of the cracks in reinforced concrete is also an important aspect for the repairing and rehabilitation of an RC bridge deck. Attempts by researchers are made to detect the surface crack depths in concrete panels (Yang et al. 2020; Yu and Vinayaka 2020).

There are many limitations to the literature available on GPR for deterioration detection and measurement in RC structures. This review helps to analyze the previous works done and develop a procedure for identifying defects with better reliability. The lab experiments discussed in ***Section 3.2*** compare variances of GPR reflections measured with different materials and at different depths. This is a stepping-stone towards measuring the deterioration of concrete in a controlled lab environment.

2.7 Details of the Reinforced Concrete Bridge Under Study

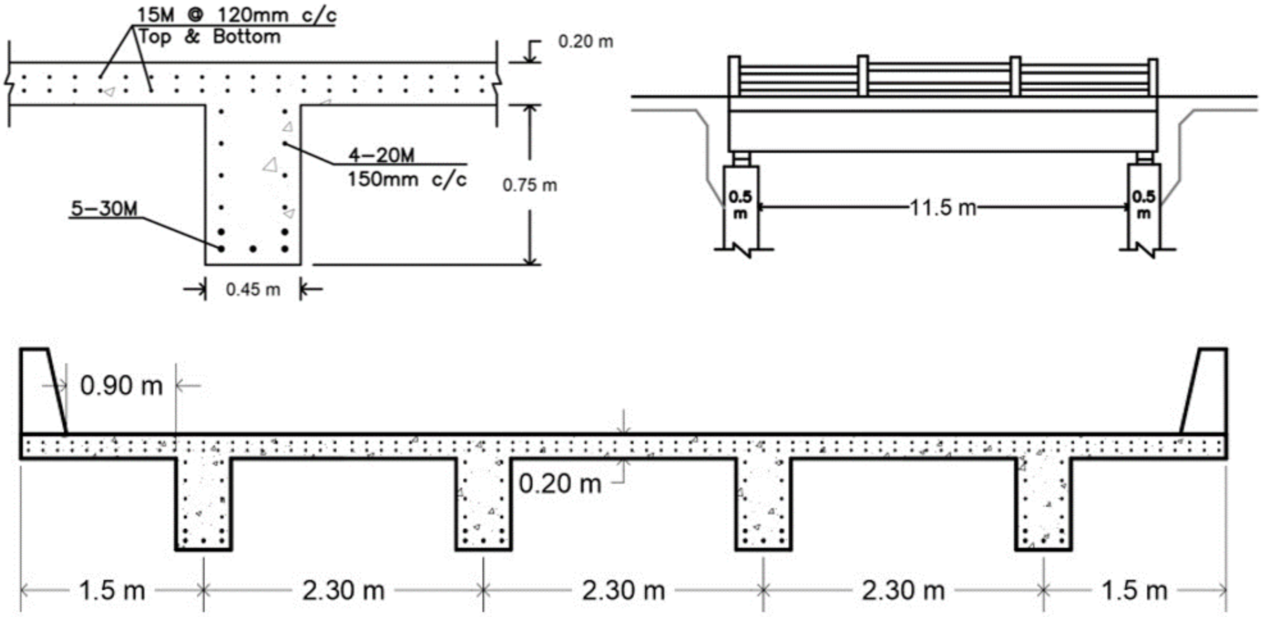

Figure 3: *Geometry and Cross Section for the Case Study Bridge with 12 m span – Adopted from (Ghodoosi et al. 2018; Ghodoosipoor 2013)*

The simplified technique and CL-625 loading of the Canadian Highway Bridge Build Code (CHBDC-S6 2014) were used to design a simply supported concrete bridge superstructure given by Ghodoosipoor (2013). The 12 m span bridge described in Ghodoosi et al. (2018) and Ghodoosipoor (2013) is used in this thesis. The detailed procedure of design of a similar bridge of span 17.5 m is given in Appendix of Ghodoosipoor (2013). ***Figure 3*** shows the geometry of a bridge with a 12 m span (Centre-to-Centre of Bearings) as well as the cross-section of T-section main beams. The 0.2 m thick concrete slab is supported by four simply supported rectangular concrete beams (roller support on one side and hinge support on the other) spaced 2.3 m apart. The concrete cover is considered to be 60 mm on all surfaces to fulfill the code requirements and for simplicity. At two ends and quarters of the span on each side, four designed concrete diaphragms are placed in the transverse direction.

2.8 Finite Element Bridge Model in SAP2000

The Non-Linear Finite Element (FE) model of bridge developed by Ghodoosipoor (2013) using SAP2000 is used as a reference in this thesis. A plane grid of longitudinal (major T-section beams parallel to carriageway) and transverse members (perpendicular to the roadway) makes up the FE model. This grillage model developed in SAP2000 is considered to be more efficient than the shell models. The benefit of employing frame components in the model is that the plastic hinge properties may be allocated to them; as a result, the hinge properties can be calculated and assigned as user-defined hinge properties in the program for each plastic hinge. To capture the influence of all the features and defects in the bridge, the simplified grillage model was closely correlated with the shell-based complete model (Ghodoosipoor 2013). ***Figure 4*** shows the grillage model of the bridge superstructure.

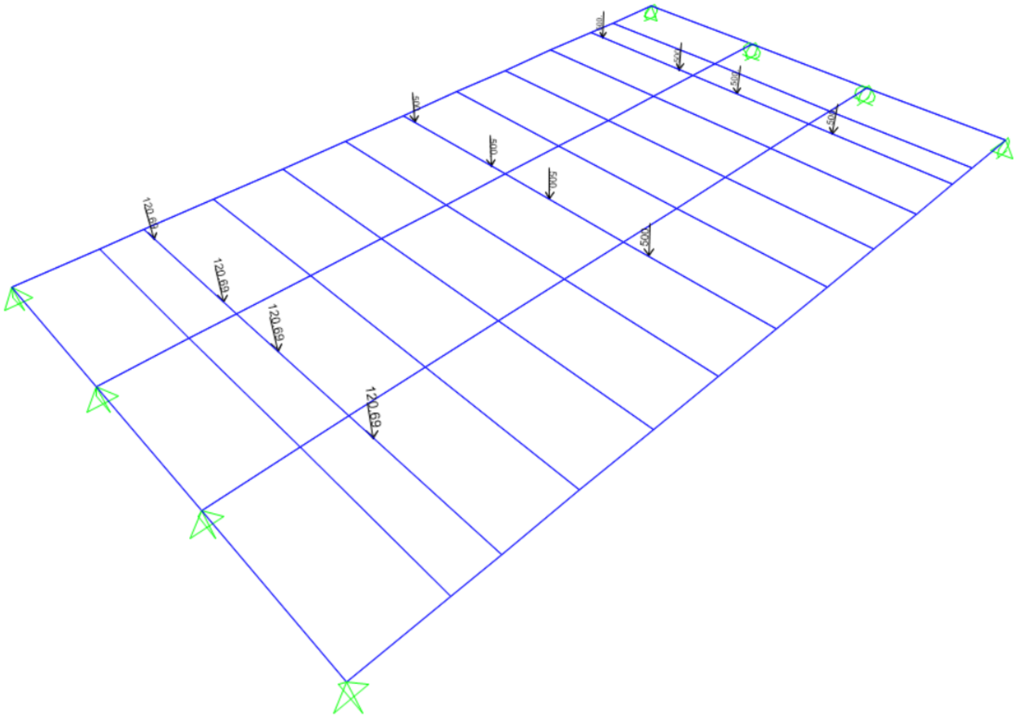

Figure 4: *Finite Element Grillage Model of Bridge Superstructure in SAP2000 – Adopted from (Ghodoosi et al. 2018; Ghodoosipoor 2013)*

2.8.1 Load Models

The regular load combination for highway bridges in the presence of the dead, live, and dynamic loads at the same time. Wind, earthquake, and collision load combinations necessitate a different strategy, which is outside the scope of this thesis.

2.8.1.1 Dead Load

Two dead load components are considered in this thesis. The first is the dead load component DL_1 acting due to the self-weight of the cast-in-place concrete. The second dead load component DL_2 acting due to the weight of the wearing surface of bitumen with the thickness of 10 cm. The specific weights of the wearing surface (γ_w) and the concrete (γ_c) are adopted to be 23.5 kN/m^3 and 24 kN/m^3 respectively.

2.8.1.2 Live Load

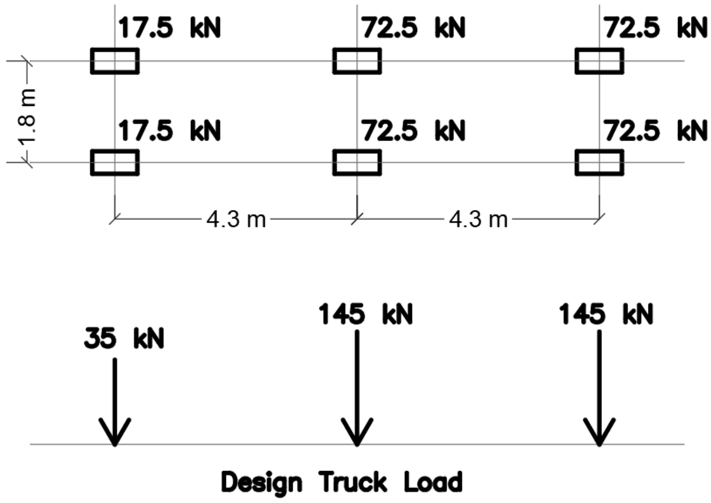

Figure 5: *Design Truck Load (Similar to HS20 Truck) -Adopted from (Czarnecki and Nowak 2007)*

The live load model (Czarnecki and Nowak 2007; Nowak 1993; Nowak, Board, and Council 1999) developed for the calibration of AASHTO LRFD (2004) is used in this thesis for the Reinforced Concrete

Bridge Deck System. The design truck's nominal gross weight is 325 KN. The design truck has three axles with nominal weights of 35 KN, 145 KN, and 145 KN, respectively (Similar to the standard HS20 truck presented in AASHTO). The critical loading situation occurs when two fully correlated vehicles (in terms of weight and axle spacing) with a particular center-line distance of the outermost wheels (in the current research 1.2 m) pass the bridge (Nowak, Board, and Council 1999). The influence line theory is used to calculate the maximum bending moment and shear caused by such vehicles. The curb distance (transverse position of truck on the bridge deck) follows a lognormal distribution (Czarnecki and Nowak 2007). The centerlines of two neighboring trucks' wheels are kept 1.2 meters apart in this thesis. ***Figure 5*** shows loads of the truck and the transverse location of the two trucks shown in ***Figure 6*** used in this thesis.

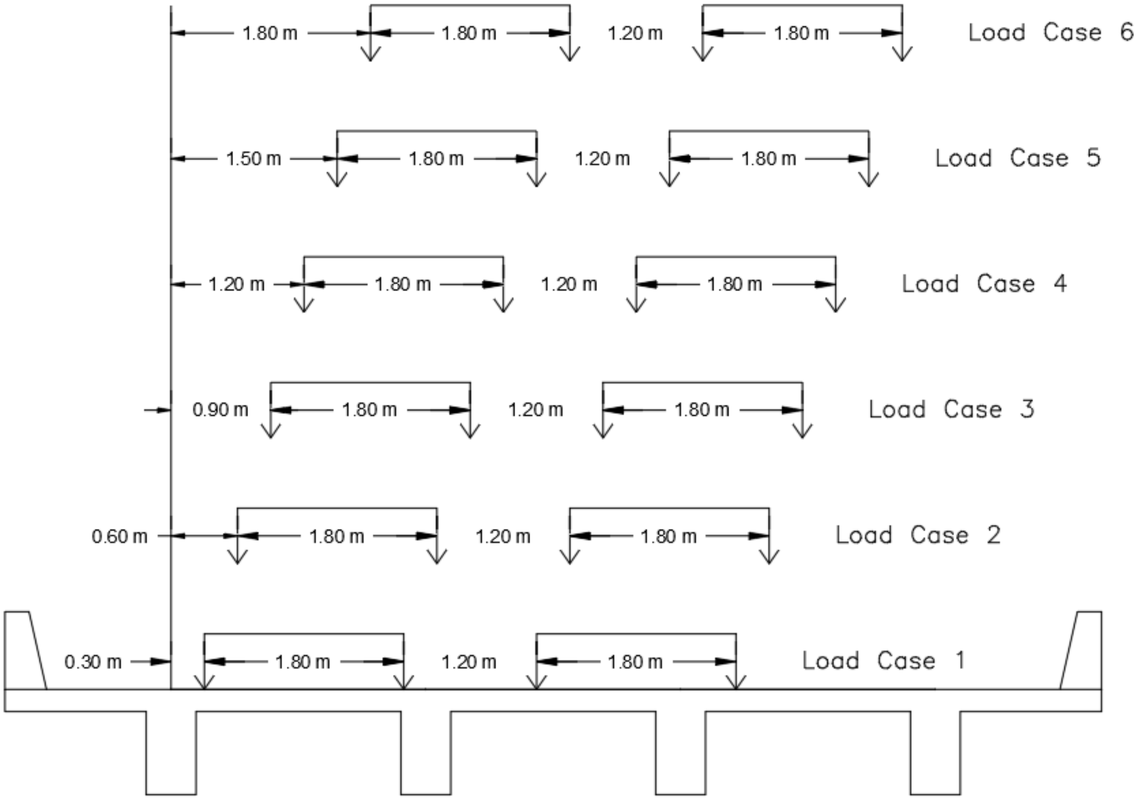

Figure 6: *Load Cases Used for Analysis - Adopted from (Czarnecki and Nowak 2007)*

2.8.2 Non-Linear Finite Element Pushover Analysis

The maximum bending moment is generated by placing two side-by-side trucks in the longitudinal direction. Based on the influence line calculations, the longitudinal crucial position of trucks has been discovered. The Gross Vehicle Weight (GVW) of two side-by-side trucks that induce failure is used to determine the bridge resistance. To determine such loads, the incremental loading pushover technique is used. The anticipated value of the GVWs determined for different transverse locations is used to calculate the capacity of the bridge superstructure system. In this thesis, six transverse positions have been considered which are shown in ***Figure 6***.

2.8.3 Modes of Failure of Reinforced Concrete Bridge Superstructure

In this thesis, the bridge model developed in the SeismoStruct 2018 is calibrated with the model available in the literature (Ghodoosi et al. 2018; Ghodoosipoor 2013). Hence, similar modes of failure are employed in this thesis.

Bridge collapse, according to (Czarnecki and Nowak 2007), happens when the non-linear deflection in any of the major components of the bridge reaches 0.0075 of the span length. The flexural and shear failures are also examined in this thesis in order to establish the ultimate limit state for the structural elements, in addition to controlling the deflection of each member. If the rotation of the plastic hinge of a specific section of a reinforced concrete structure exceeds a specified value θ_p, that section is said to have failed in the flexural mode. θ_p is expressed as a function of the curvature of the section at the beginning of yielding φ_y, the maximum curvature of the section in the final state φ_u, and the length of the plastic hinge l_p in this scenario. ***Equation 2.16***, where H is the section depth, is the simplest version of the plastic hinge length of a concrete section (Park and Paulay 1975) considered in this thesis.

$$\theta_p = (\varphi_u - \varphi_y)l_p \qquad \text{Equation 2.15}$$

$$l_p = 0.5H \qquad \text{Equation 2.16}$$

In Ghodoosipoor (2013), the procedure to convert the idealized tri-linear Moment-Curvature relationship into a bi-linear representation of the Moment-Curvature is given. The bi-linear Moment-Curvature relation is used for the SAP2000 model. From the trilinear curve, a bilinear representation of the Moment-Curvature relation is derived, where both diagrams indicate an equal amount of absorbed energy. The initial cracking point is defined as a point for which the tensile stress in the outermost edge of the section exceeds $0.4\sqrt{f_c'}$, the normal density concrete cracking strength (CHBDC-S6 2014). The section has the uncracked stiffness EI_g before the cracking point is reached and then the stiffness of the section reduces to EI_{cr}. The effective stiffness of the section is represented by EI_{eff}. The section is considered as yielded when the tension steel yields first (Park and Paulay 1975). The ultimate state point also the failure point of the section is defined as the moment at which the concrete reaches an ultimate strain of 0.0035 in compression or the tension steel strain level exceeds the ultimate strain of 10% (CHBDC-S6 2014).

According to the findings of Ghodoosipoor (2013), the ultimate state of a newly constructed bridge girder is determined by compression failure due to crushing of concrete; whereas, the collapse of a highly corroded girder at the end of service life of the bridge is typically determined by tensile failure in reinforcing steel. It is worth noting that the mechanical characteristics of steel reinforcement do not vary with time, but the effective cross-sectional area of reinforcement shrinks because of corrosion. Shear hinges are installed in the major girders of the bridge superstructure to account for shear failure. The shear hinges have little ductility due to the brittle shear fracture of concrete. When the force approaches the shear strength of the member calculated in accordance with CHBDC-S6, the section shears immediately

(Ghodoosipoor 2013).

The calculation of conversion of tri-linear Moment-Curvature relation to bi-linear Moment-Curvature relation is given in ***Appendix B***. These calculations are utilized to assign the flexural and shear hinges to the SAP2000 model. However, the need of doing these calculations and hinges assignments is eliminated in the newly developed bridge model in SeismoStruct 2018. In SeismoStruct the elements are modeled as fiber elements hence the modeled section comprises numerous uniaxial fiber elements and hence eliminates hinge assignment to the sections. Also, instead of using the tri-linear or bi-linear models, the results obtained in SeismoStruct are curvilinear providing the realistic behavior of the section.

2.9 Model Updating of Reinforced Concrete Structures with NDE Techniques

Structural damage is an inherent feature of engineering structures, and it is prone to propagate, attributed to a variety of environmental and mechanical causes. Structures age and have a shorter design life as a result of short and long-term damages, making the monitoring process a crucial component for structures (Chen and Ni 2018). Visual inspection was used to monitor structural deterioration and changed through time as the areas of structural health monitoring (SHM) and structural damage detection (SDD) advanced. In order to make the monitoring process more practical, a variety of approaches have been developed to identify, locate, and quantify structural deterioration (Amezquita-Sanchez and Adeli 2016; Chesné and Deraemaeker 2013). Damage is typically described as a change in geometric or material properties of a system that impairs its performance, safety, durability, or operational life (Cosenza and Manfredi 2000; Frangopol and Curley 1987). Damage, according to this definition, does not always imply a full failure of a system, but rather a relative decrease of its functionality, resulting in suboptimal performance (He and Zhu 2011; Kaouk and Zimmerman 1994; Zimmerman and Kaouk 1994). Damage may build if no remedial action is done, eventually leading to failure. Depending on the type of damage, systems may fail gradually or suddenly (Çatbaş, Kijewski-Correa, and Aktan 2013; Farrar and Worden 2010). For example, corrosion and fatigue failures generally take a long time to manifest, but earthquakes and fire-related damage can cause sudden failure (Farrar, Doebling, and Nix 2001).

Due to the overwhelming number of bridges that must be examined at the state level, bridge management is particularly difficult. To allocate resources to bridge maintenance and guarantee their usability during their lives at a fair cost, reliable methods of evaluation are required. Nondestructive testing (NDT) and monitoring can give useful information regarding the present state of bridges. Many monitoring and testing approaches have been developed in recent decades to enhance structural response expertise. A careful study of prior work indicates the significant issue of converting measurement data into knowledge that can be used to identify structures and make decisions (Bayane et al. 2021).

Traditional bridge assessment approaches in the context of infrastructure health monitoring, such as a condition-based survey utilizing visual inspection, which is often employed by industry, have limitations in determining the entire degree of inflicted damage to structures (Helmerich et al. 2012). In the lack of structural design information and drawings (as is often the case with older structures), traditional approaches have proven to be more difficult to use (Thakkar, Ghosh, and Singh 2006). It is also well recognized that the complexity of bridge constructions necessitates a more rigorous and detailed approach when long-term structural integrity and functionality are required (Lam, Ng, and Veidt 2007). For the successful repair and maintenance of bridge structures, a variety of methodologies for assessing the response of the structure have become employed extensively (Diamanti, Giannopoulos, and Forde 2008; Lynch et al. 2004)

Gucunski and Nazarian (2010), Parmar and Sharp (2009), and L. Liu and Guo (2005) are a few examples of using non-destructive bridge health evaluation technologies such as Ground Penetrating Radar (GPR), Acoustic Emission, and Tomographic Imaging. Finite Element (FE) methodologies have also been shown to be effective in simulation and analyzing the behavior of bridges in the context of structural health evaluation. Impact echo, ultrasonic surface waves, ground-penetrating radar, half-cell potential, and electrical resistivity are the five NDE technologies used to collect the data and they proposed that this data be integrated into finite element models by loosening deck layer constraints and softening deck stiffness, respectively (Gucunski and Nazarian 2010).

Various researchers have combined several NDE methods and utilized the results for the structural model updating of the bridges. Conde et al. (2017) integrated laser scanning, ground penetration radar, sonic tests, and ambient vibration testing and developed an updated finite element model of a historical arch bridge. Sánchez-Aparicio et al. (2019) used terrestrial laser scanners, the sonic and impact-echo methods, the ground-penetrating radar, and the multichannel analysis of surface waves to develop a FE model of masonry arch bridge. (Wolert et al. 2020) did non-destructive testing on a 100-year-old Reinforced Concrete Flat Slab Bridge. The researchers utilized a standard tape measure, a laser distance meter, an ultrasonic pulse velocity (UPV) thickness measurement equipment, and an advanced concrete cover meter (ACCM) to detect rebars and measure their diameters and spacings. Ground-penetrating radar (GPR) detected top reinforcement, which necessitated lane closure. The performed load test to get the vibrational and deflection characteristics of the bridge. By using these data they updated the FE model by changing the properties of concrete and steel (Wolert et al. 2020).

2.10 Model Updating of Reinforced Concrete Deck Using GPR Deterioration Map

A study done by (Dabous et al. 2017; Salam 2014) proposed an integrated approach for detecting concrete bridge faults that combines infrared (IR) thermography with ground-penetrating radar (GPR) technology. Integrating findings can increase fault identification and quantification confidence, and hence improve the bridge condition rating process's dependability (Dabous et al. 2017). In a case study of a concrete bridge deck in the city of Laval, Quebec, Canada, this integrated system was implemented when the life of the bridge was about 45 years. The acquired data were compared to those obtained during a comprehensive and visual assessment of the bridge before its demolition.

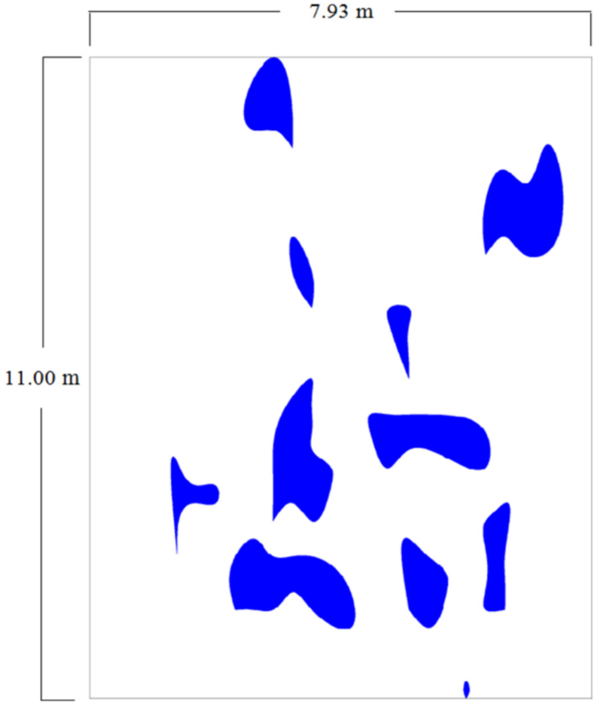

Figure 7: *Defect map based on the GPR results (Salam 2014)*

The investigation was limited to a 77-square-meter portion of the bridge deck. Both IR Thermography and GPR technologies were used to inspect the segment. On the same part of the bridge, a thorough assessment utilizing hammer sounding and visual inspection was carried out. The apparent surface defects on the selected portion were identified by a visual inspection. Then, using hammer sounding, a comprehensive investigation was carried out to locate and quantify the degree of internal delamination. For verification, the findings of the Infrared Thermography (IR) and GPR testing were compared to the results of the visual and hammer-sounding examinations. In the account of the inspection results, it was decided to rebuild the bridge deck. The GPR findings were interpreted using the RADAN program. The locations of possible faults were entered into AutoCAD as lines, with each line corresponding to the start and end of each signal attenuation region. A defect map was created from the locations where spall and delamination were found using the GPR test (Dabous et al. 2017). ***Figure*** *7* shows the defect map generated with the help of GPR.

Ghodoosipoor (2013) developed a non-linear finite element model of a bridge discussed in ***Section 2.7*** and ***Section 2.8*** to calculate the reliability-based deterioration model of the bridge superstructure system. As the defect map's dimensions were comparable to those of the finite element model of the 12 m bridge superstructure, a finite element model updating procedure was introduced by Ghodoosi et al. (2018).

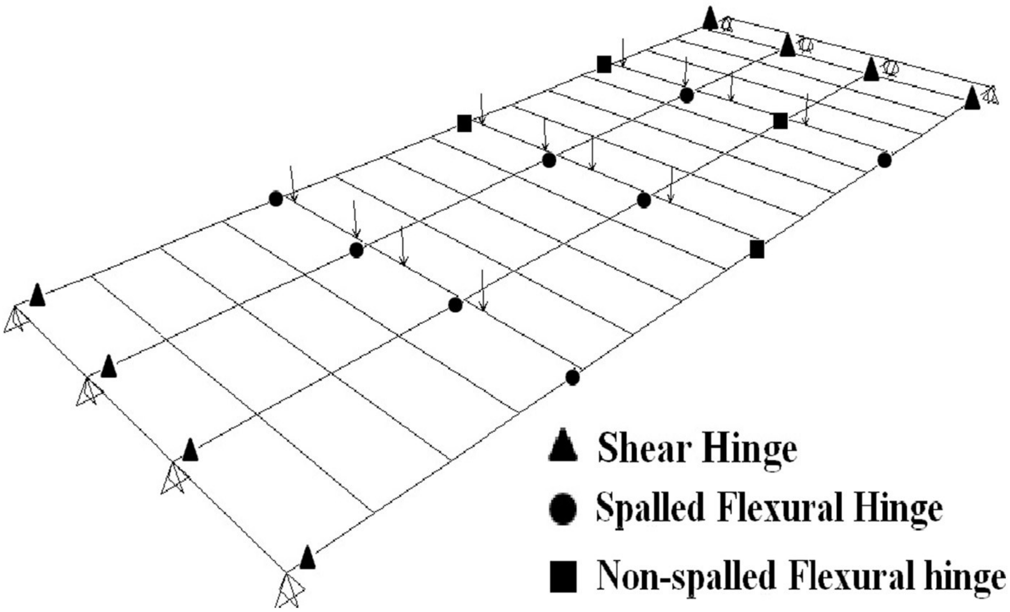

Figure 8 *Updated Finite Element Model of a Bridge using GPR Defect Map (Ghodoosipoor et al. 2018)*

An assumption was made in this approach that as the GPR test for the soffits of the bridge superstructure was complicated for application uniform chloride contamination was assumed. Because the depth of the spalled cover reduces the concrete compression zone, a spall or delamination reduces the flexural capacity of the bridge deck. A consistent decline in bar diameter of $\lambda \approx 0.0116\ i_{corr}$ was evaluated here, with a mean value of i_{corr}=1.5 μA/cm^2. The top surface defect map was considered to be incorporated into the non-linear FE model of the bridge superstructure as illustrated in ***Figure 8***. The whole concrete cover was delaminated in the regions marked on the defect map, which is a conservative assumption. Spalled and non-spalled flexural plastic hinges were examined in the study. Non-spalled plastic hinges were those with no delamination recorded on the top surface while the spalled plastic hinges have the top surface spalled according to the defect map. Three flexural plastic hinges were installed in the major T-section beams parallel to the highway, one in the center and two in each quarter of the beam along with two shear hinges modeled at each corner (Ghodoosi et al. 2018). The calculations involved in this thesis for the calculation of the flexural plastic hinges are given in ***Appendix A***.

Despite this method provides a fair degree of accuracy in model updating and evaluation of the capacity of the bridge, there are some limitations. Apart from changing the sections of the bridge, this method involves the assignment of plastic hinges to the girder sections which in itself is a tedious procedure as it needs manual calculations for the estimation of the behavior of the plastic hinge. Also, the model assumes a bi-linear behavior of the flexural hinge which is not realistic in the actual case. This thesis focuses on developing a fiber-based finite element model in SeismoStruct to eradicate these limitations of modeling described in ***Section 3.4***. and a methodology for model updating is discussed in ***Section 3.5*** which includes only the change in the sections of the bridge.

Chapter 3 Methodology

3.1 Introduction

The use of Ground Penetrating Radar as a Non-Destructive Evaluation Technique in Structural Health Monitoring has increased and has been evolving over the past few decades. The GPR has capabilities to perform a structural evaluation of concrete along with detection of surface as well as subsurface flaws. The ease with which GPR can be helpful for scanning large structures such as bridges, parking lots, tunnels, etc. has made its use popular and has got attention from the bridge management agencies. Many laboratory experiments are performed to make improvements to the use of GPR for the detection of deterioration in reinforced concrete structures. The data obtained from NDE techniques are used by the researchers for finite element model updating of the structures which can help decision-makers to plan for a cost-effective restoration and retrofitting schedule. The objective of this thesis is to explore the possibilities of using GPR for the detection of subsurface deterioration using the Ground Penetrating Radar and provide a novel finite element model of bridge superstructure for model updating.

This thesis contains two separate methodologies which the first methodology contains a brief description of the laboratory experiment in which an attempt is made to analyze the subsurface materials of concrete which can be helpful in the future for detection of subsurface flaws in concrete. The second methodology consists of the development of a non-linear fiber-based finite element model of a bridge superstructure and a procedure for the finite element model updating using a GPR defect map.

The approach utilized in the first methodology of laboratory experiment is given in the flow chart shown in ***Figure 9***. In the first phase of the laboratory experiment, the planning involves selecting the size of plain concrete slabs as well as for deciding the study parameter. The concrete slabs are cast in the laboratory when the plan is finalized, cured for two weeks, and then dried. The parameter amplitude, which is derived from evaluating the data received from GPR scanning, is used to investigate materials such as sheets, rebars, air gaps, water gaps, and salt solution gaps underneath the concrete surface. The data interpretation and results are the final steps of the laboratory experiment. ***Section 3.2*** includes a thorough explanation of concrete slabs, sheets, rebars utilized as well as air, water, and salt solution gap thicknesses, as well as the arrangement employed in the laboratory.

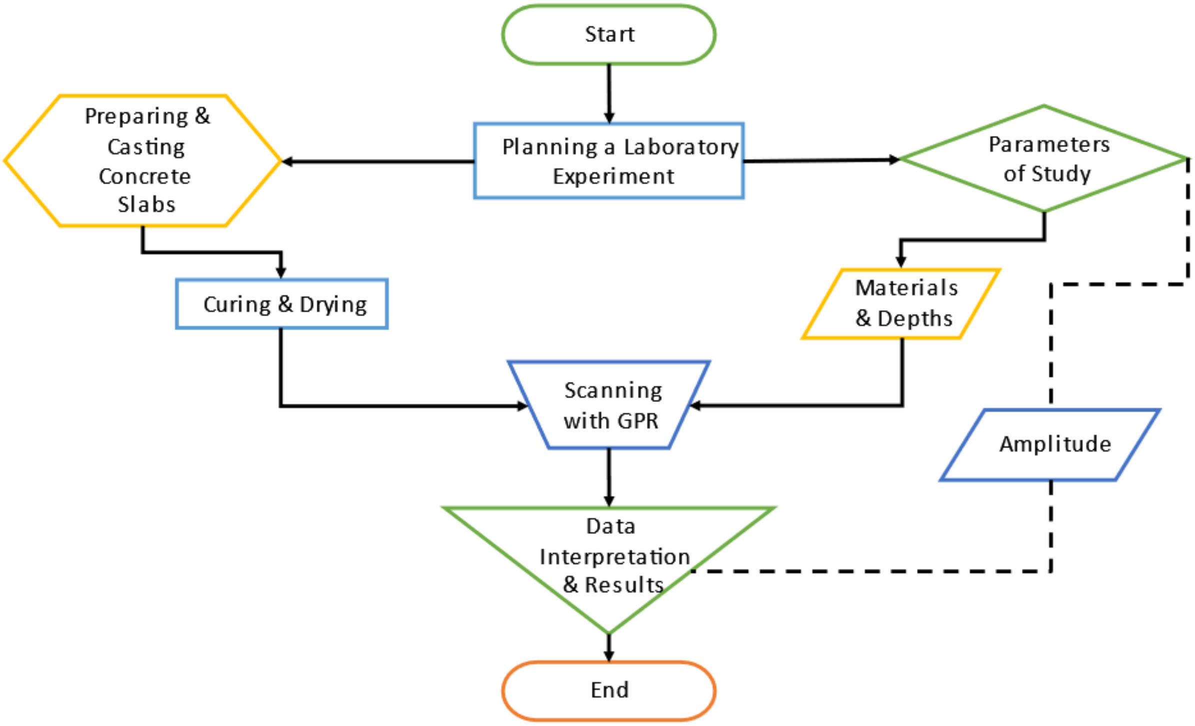

Figure 9: *Flow chart of the methodology used in the laboratory experiment*

The flow chart shown in ***Figure 10*** shows the methodology employed for the development of the finite element fiber model of bridge superstructure along with its model updating using a ground-penetrating radar deterioration map. The first step involves collecting the data and defining the bridge superstructure model along with the structural parameters. Along with this step, data is collected of a deterioration map of a bridge portion scanned using the Ground Penetrating Radar available in the literature. The next step involves defining a procedure to develop a Fiber-based Finite Element Model. The validation of results is made using linear static analysis and non-linear pushover analysis. After the validation, the full Fiber-based Finite Element model of the bridge superstructure is developed, and it is calibrated using the previous finite element model available in the literature. After the calibration of the bridge model is performed, the method for model updating using the Ground Penetrating Radar image is defined and applied. The last step involves the data interpretation and discussion of results.

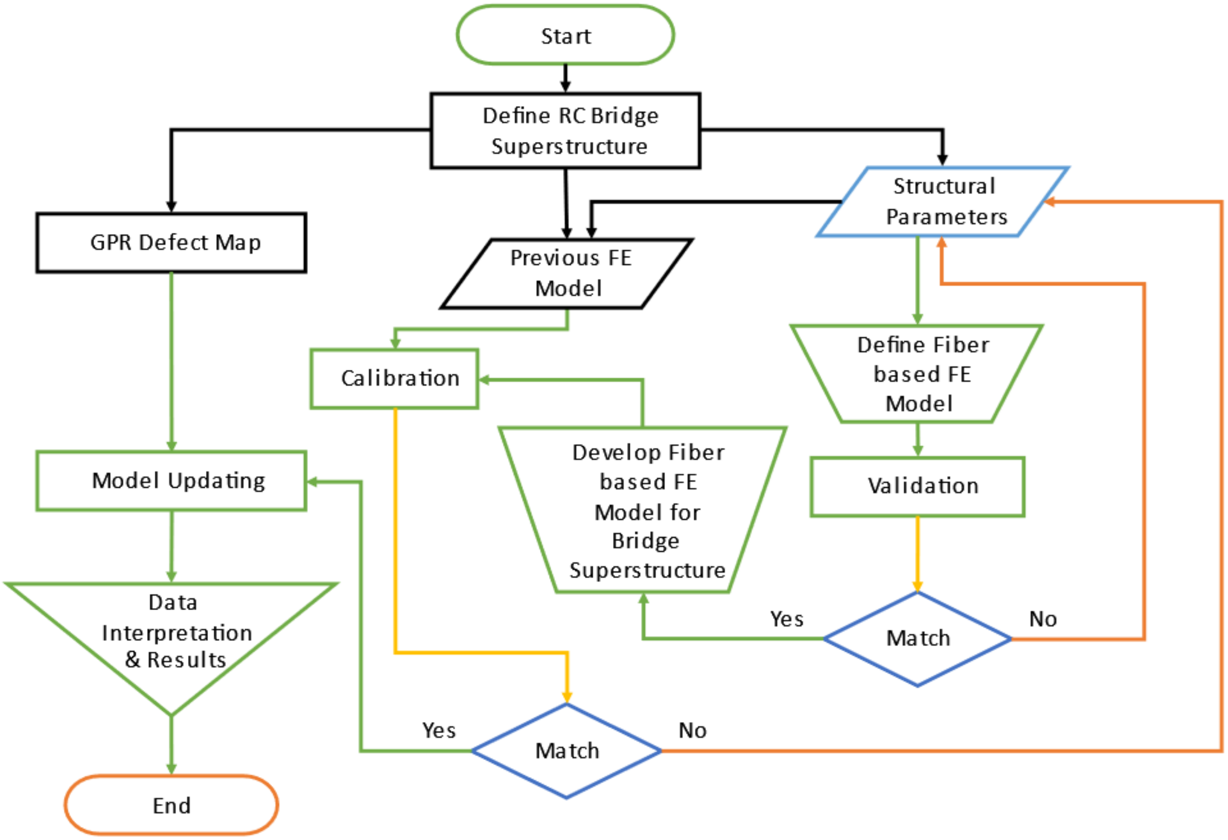

Figure 10: *Flow Chart of Methodology for Developing Finite Element Bridge Superstructure Model and its Model Updating*

3.2 Methodology for Detection of the Sub-Surface Materials in Plain Concrete Slabs

The details about the test slabs, materials under the study as well as the experimental arrangement employed in this study are explained in the following sub-sub sections:

3.2.1 Concrete Slabs

The research experiment was planned and executed at the Structures lab of Concordia University. This experiment involved preparing and casting three plain cement concrete slabs of the plane dimension of 25 x 50 cm with the depths of 5 cm, 10 cm, and 20 cm respectively using Quikrete which is a high early strength commercial grade concrete premix. In preparing the formwork of the slabs, a smooth plastic sheet was added at the bottom of the formwork in order to have a smooth surface on one side of each slab. The required amount of water was mixed with the premix and poured for casting the slabs. The 28-day compressive strength of concrete obtained for the slabs was 35 MPa. These slabs were cured for two weeks and then they were left to dry in the lab. ***Figure 11(a)*** shows these slabs which are stacked on top of each other, slab 1, 2, and 3 are 5 cm, 10 cm, and 20 cm thick, respectively (Donda et al. 2021).

(a) *(b)* *(c)*

Figure 11: *(a) Plain concrete slabs; (b) Sheets used; and (c) Rebars used under study (Left to Right; 6 mm, 10 mm, 18 mm, 20 mm, & FRP 21.8 mm) (Donda et al. 2021)*

Three different arrangements of slabs were used in this experiment. Arrangement one for the study of 5 cm depth involved placing slab 1 on top of slab 3 while putting the material under the study sandwich between the slabs. Similarly, the second arrangement included slab 2 placed on top of slab 3 to study the material at the depth of 10 cm. And the last arrangement involved the study of material at 15 cm depth which consists of using the combination of slab 1 and slab 2 on top of slab 3 while putting the material under the study above slab 3. Due to the small size of the concrete slabs, an attempt to study the depth of 20 cm by placing slab 3 above slab 2 was done, however it did not give reliable results due to the fact that the reflections from the side walls interfered. Hence, only three depths 5 cm, 10 cm, and 15 cm were studied in this experiment (Donda et al. 2021).

3.2.2 Sheets and Rebars Used in this Study

In this analysis, three different types of sheets were used: white paper, brown cardboard, and foam sheets with thicknesses of 0.4 mm, 2.88 mm, and 5 mm, respectively. These sheets were sandwiched between the slabs individually, as well as the fourth kind, by stacking all three sheets together, and scanning was done according to the arrangements described in the previous section. The thickness of these sheets was measured after the experiment since they are compressible. In this study, four rebars with diameters of 6 mm, 10 mm, 18 mm, and 20 mm, as well as an FRP bar with a diameter of 21.8 mm are utilized. Because of the small dimension of the slabs, it was observed that the hyperbolic reflections of the rebar overlapped when two or more rebars were placed in-between the slabs as a result only one bar was used individually for each scanning test. The sheets used in this experiment are shown in ***Figure 11(b)***, while the rebars are shown in ***Figure 11(c)*** (Donda et al. 2021).

3.2.3 Study of Air Gap and Water Gap

Concrete may contain air entrapped in its cracks/gaps along with some impurities during a hot summer day. Taking this into consideration an experimental setup was established to study variations in the GPR signal amplitudes due to the air gap. Five different air gap sizes (3 mm, 4 mm, 4.8 mm, 5.8 mm, and 8.8 mm) were studied at the depths of 5 cm, 10 cm, and 15 cm by using the arrangements explained in ***Section 3.2.1***. These air gaps were created by using the metal strip pairs of 1 mm, 3 mm, and 4.8 mm in thickness and placing them along the length of the slab (this prevents interference of the GPR signals) near each edge on slab 3 and then placing the slabs on top of this arrangement which creates a uniform air gap between the slabs. ***Figure 12(a)*** shows the metal strips employed in this arrangement.

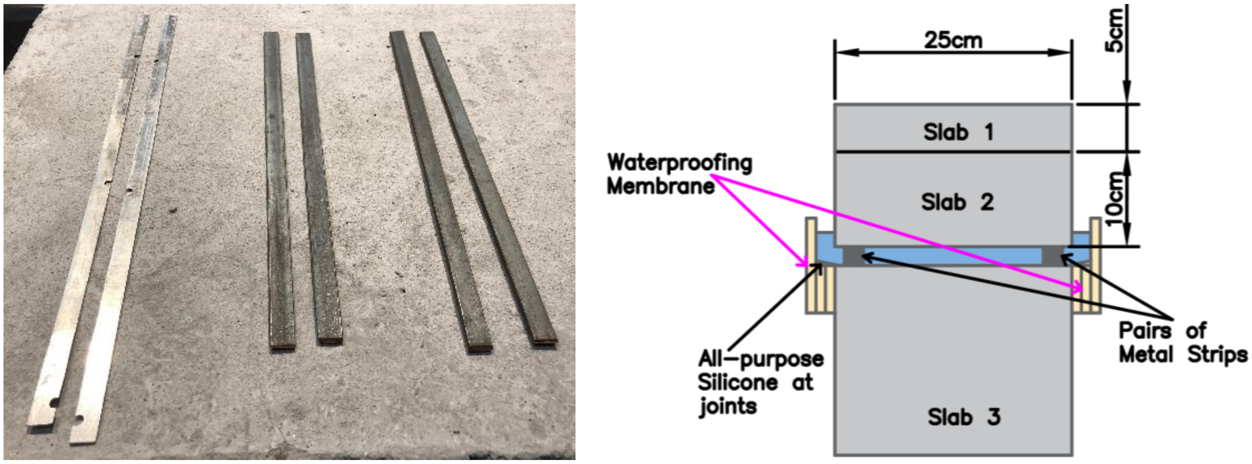

(a) *(b)*

Figure 12: *(a) Metal strips used in the arrangement (Left to Right; Pair of sizes 1 mm, 3 mm, & 4.8 mm thickness); and (b) Schematic diagram showing an arrangement to create water gap (Donda et al. 2021)*

Entrapping of water in the cracks in concrete caused by penetration of rainwater runoff, drainage water intrusion inside tunnels, or melting of snow in colder regions due to the usage of de-icing salts can result in the formation of water gap in concrete. Hence, in this experiment, an attempt is made in the laboratory to study the changes in the GPR signals due to the subsurface water gap. The water gap between the slabs is created here through a special arrangement. The metal strips used to create air gaps were used to make similar water gaps. The prevention of water leakage was done by using a multi-purpose waterproofing membrane and the joints are further sealed using all-purpose silicone. Two layers of membrane strips are added initially surrounding to the slab 3 of 20 cm depth to make clearance to place slab on top of slab 3. An additional layer of membrane is added such that it is sufficiently higher to ensure a miniature water-pool arrangement. The joints between the water-proofing membrane itself as well as with the slab are made watertight by using all-purpose silicone. Water is added after making the arrangements of metal strips to create a uniform gap of 3 mm, 4 mm, 4.8 mm, 5.8 mm, and 8.8 mm on which the other slabs are placed (Donda et al. 2021).

3.2.4 Solution with Various Concentrations of Salt

When deicing salt used to melt snow dissolves in water and enters the cracks, or when water that enters the crack dissolves dry salt already present in the concrete cracks, a salt solution may form in between the cracks. As a result, a lab experiment was undertaken to investigate the influence of various salt solution concentrations on the reflected amplitude of GPR. The same gaps of 3 mm, 4 mm, 4.8 mm, 5.8 mm, and 8.8 mm were utilized with the arrangement shown in ***Figure 12(b)*** for the water gap. Instead of using clear water, this study utilized six different concentrations of salt solution of 1%, 3%, 5%, 10%, 15%, and 20% to see how they affected the reflection amplitude. The experiment involved increasing the concentration of a salt solution in a sequence. Also, after collecting data for a specific salt concentration, the slabs were washed with tap water and then air-dried for 3 days before repeating the experiment with a higher concentration, to ensure that no salt from the previous setup was present. This experimental setup was utilized for slab depths of 5 cm, 10 cm, and 15 cm.

3.2.5 GPR Scanning Configurations

GSSI Model 51600S Ground Penetrating Radar with a central frequency of 1.6 GHz was employed for scanning the slabs. The central frequency of GPR systems is usually quite closest to the frequency where the spectral amplitude peaks. The timing between transmitter firings is the pulse duration of a GPR antenna. The pulse duration of the antenna utilized is 0.7 nanoseconds. The pulses per second or cycles per second emitted by the antenna are referred to as sampling frequency. The antenna generates 512 scans per second with 16 bits per sample, and in the experiment, a frequency of 333 scans per second is used. The dielectric permittivity of a material, which is a fundamental physical characteristic, describes its electrical polarizability. By dividing the material permittivity by the free space permittivity, the relative dielectric permittivity, also known as the dielectric constant, of a material is estimated. The dielectric constant is set at 6.0, and the time range is set to 6 nanoseconds during the scanning of the slabs. The depth range of 35 cm was set to ensure that the scan results are accurate to the whole depth. The antenna is placed on a handheld mini cart with a survey wheel, allowing for the recording of distance data. The antenna is connected to a GSSI SIR-4000 control unit via a controller box. ***Figure 13*** shows a GPR antenna installed on a small cart that was utilized to conduct the scanning for the experiment. The scanning is done along the longitudinal direction of the slab (i.e., along 50 cm), with the amplitude values at selected points of the reflected signal, referred to as B-scans, being investigated further for analysis (Donda et al. 2021).

Figure 13: *GPR antenna mounted on a handheld mini cart used to scan along the length of the slab*

3.3 Finite Element Modeling Procedure

In this thesis, a more precise finite element model of the bridge superstructure is developed for a reinforced concrete bridge superstructure system designed as per the Canadian Highway Bridge Design Code (CHBDC-S6 2014). A capacity of a deteriorated bridge from its structural model will assists decision-makers in more accurately and rationally predicting the timing for potential major interventions.

The bridge superstructure system described in ***Section 2.7*** and ***Section 2.8*** is modeled in SeismoStruct 2018. SeismoStruct is an award-winning non-linear finite element package used in many kinds of research (SeismoSoft 2018). The SeismoStruct can analyze a three-dimensional model with geometric nonlinearities and considers distributed material inelasticity using fiber elements in static as well as non-linear analysis. SeismoStruct considers the inelasticity along the length of the member as well as its cross-section (Ali 2019). The use of this software will be advantageous considering the distributed inelasticity along the entire bridge, it will eliminate the plastic hinge calculation and comparatively more detailed analysis could be done by assigning reduction in the area of reinforcement and reducing the section due to delamination and spalling at a particular location based on the data available from different Non-Destructive Evaluation testing methods, here GPR.

The deflection of a steel-reinforced element in a non-linear condition is limited to a specific value (i.e., 0.0075 of the span length) and the rotation (curvature) of plastic hinges is limited to a collapse threshold, where flexural failure is obtained either by concrete crushing in compression (0.0035 strain value) or steel ruptures in tension (0.10 strain value) in order to assess its capacity as discussed in ***Section 2.8.3***.

3.3.1 Structural Parameters

The yield strength of the reinforcing steel is considered f_y = 400 MPa with the modulus of elasticity E_s = 200 GPa. The Poisson's ratio of the steel is considered as υ_s = 0.3. The coefficient of thermal expansion is taken as $\alpha_s = 11.7 \times 10^{-6}$ °C^{-1}. The specific weight of steel is considered as γ_s = 78 kN/m^3. The fracture or buckling strain of steel is considered as 0.10 which is 10% as discussed in ***Section 2.8.3***. The non-linear Menegotto-Pinto steel model (Menegotto and Pinto 1973) is used for modeling the reinforcing steel in SeismoStruct.

The compressive strength of concrete is considered as $f_c{}' = 40$ MPa. The modulus of elasticity for concrete E_c is calculated considering the specific weight of cast in place concrete γ_c as described in the dead load model (***Section 2.8.1***) (CHBDC-S6 2014) is given by:

$$E_c = \left(3000 \times \sqrt{f_c'} + 6900\right) \times \left(\frac{\gamma_c}{2300}\right)^{1.5} \qquad \textit{Equation 3.1}$$

The Poisson's ratio of the concrete is considered as $\upsilon_c = 0.2$. The coefficient of thermal expansion is taken as $\alpha_c = 1.0 \times 10^{-5}$ °C^{-1}. The tensile strength of concrete is considered $0.4\sqrt{f_c'}$ as discussed in ***Section 2.8.3***. The ultimate strain in compression is considered as 0.0035. The non-linear Mander et. al. (Mander, Priestley, and Park 1988) concrete model is used in the thesis for modeling in SeismoStruct. The uniform concrete cover for the bridge girder sections of 60 mm is considered.

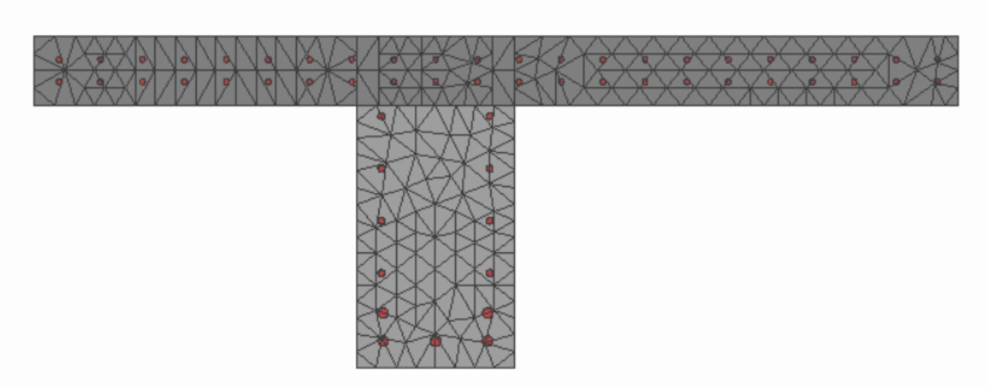

Figure 14: *Discretization of Fiber Elements of External Girder of a New Bridge.*

The longitudinal bridge girder sections are modeled using section-type Reinforced Concrete Jacketed T-Section (rcjts). These sections are cautiously selected from the beginning as these sections will be helpful to model the deteriorated sections as discussed in ***Section 3.5.3***. The element class of Inelastic Displacement-based Frame Element (infrmDB) is used for the girder sections with 500 section fibers. ***Figure 14*** shows the discretization of the external girder of the new bridge. The concrete (in grey for beam and dark grey for deck with triangular elements) and reinforcement bars (in red circles) are considered as individual fibers for the analysis. The displacement-based 3D beam-column element type infrmDB can be used to represent members of space frames with geometric and material nonlinearities. As the finite element model of the bridge involved the interconnected girder sections of small lengths, the infrmDB element provides more accurate results in this case (SeismoSoft 2020). The transverse members including the diaphragms are modeled as Elastic Frame Element (elfrm) due to the reason that they were found to respond in their elastic range during the analysis. This thus helps in reducing the computational time to some extent. The elastic properties were taken similar to that of the previous SAP2000 model. Here one end of the bridge girders is supported by hinge support and the other end by roller support. The dead load and live load mentioned in the ***Section 2.8.1*** are applied to the bridge model. The non-linear static pushover analysis is performed applying increment to the live load due to the trucks. Since the SeismoStruct 2018 is not able to consider the drift-based performance criterion, the deflection limit (0.0075 of span length) is checked manually from the analysis results. While the flexural failure due to crushing of concrete and rupture in steel is defined in performance criteria for which the program gives warnings when a criterion is reached. In this thesis, only material inelasticity is considered while the geometric nonlinearities are not in the scope of this thesis.

3.3.2 Validation

Two simply supported reinforced concrete T-beams (same as the internal and external girder used for the bridge) with the same span length of 12 m as shown in ***Figure 15*** are modeled in two different non-linear analysis programs, SeismoStruct 2018 and SAP2000. Besides hand calculation is performed for further validation of the results. The inelastic behavior in the SAP2000 model is applied by assigning plastic hinges by calculating the non-linear moment-curvature relation for the section and two shear hinges near the supports. Hence these values of moment-curvature are directly compared with the values obtained from the SeismoStruct results. Here two models are developed for the same girder in SAP2000, first with one flexural hinge at its center and the second one with many flexural hinges (at joints same as those connecting transverse elements in the bridge model) to study and compare the effect of concentrated plasticity at a single point and distributing plasticity at many locations along the length of the girder. Here the SAP2000 results are compared to SeismoStruct to show that the results obtained in SeismoStruct are more realistic along with its modeling being simple by eliminating hinge assignment. ***Figure 16*** shows the non-linear finite element models of the internal girder in SAP2000 and SeismoStruct.

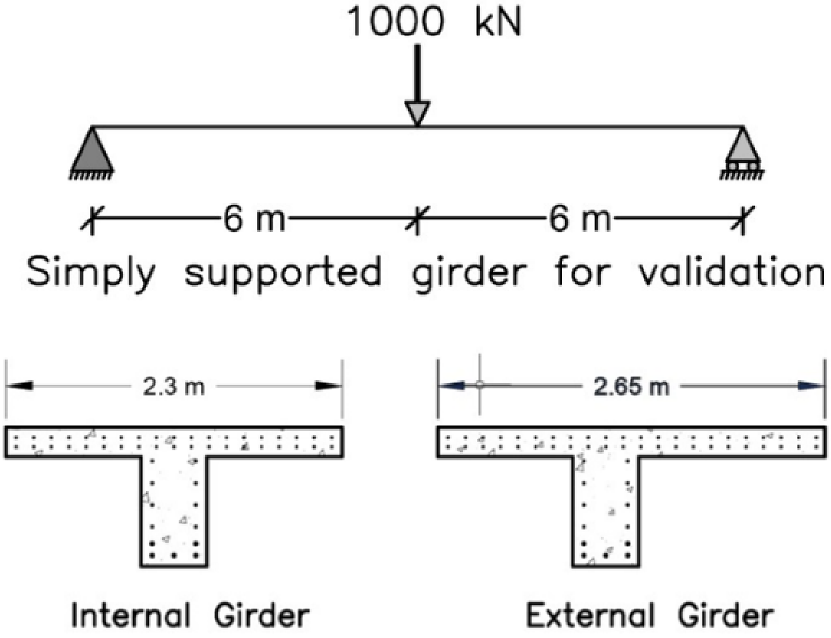

Figure 15*: Simply Supported Girders used for Validation*

The deflections of the girder section are calculated manually using the effective moment of inertia (I_{eff}) up to the yielding point as it is an accurate tool for comparison of the response of element in its elastic limit. The I_{eff} is given by the following equation (Park and Paulay 1975):

$$I_{eff} = \left(\frac{M_{cr}}{M_a}\right)^3 I_g + \left[1 - \left(\frac{M_{cr}}{M_a}\right)^3\right] I_{cr} \qquad \textit{Equation 3.2}$$

where $M_{cr} = f_{cr}\, I_g / y_t$ is the cracking moment, f_{cr} is the tensile strength of concrete, I_g is the gross (uncracked) moment of inertia, y_t = distance of the tension face from the neutral axis, I_{cr} = moment of inertia of cracked section, and M_a = moment due to the applied load. Deflection at midspan for a point load acting at the center of the girder is given by:

$$\delta_{0.5L} = \frac{PL^3}{48\, E_c\, I_{eff}} \qquad \text{Equation 3.3}$$

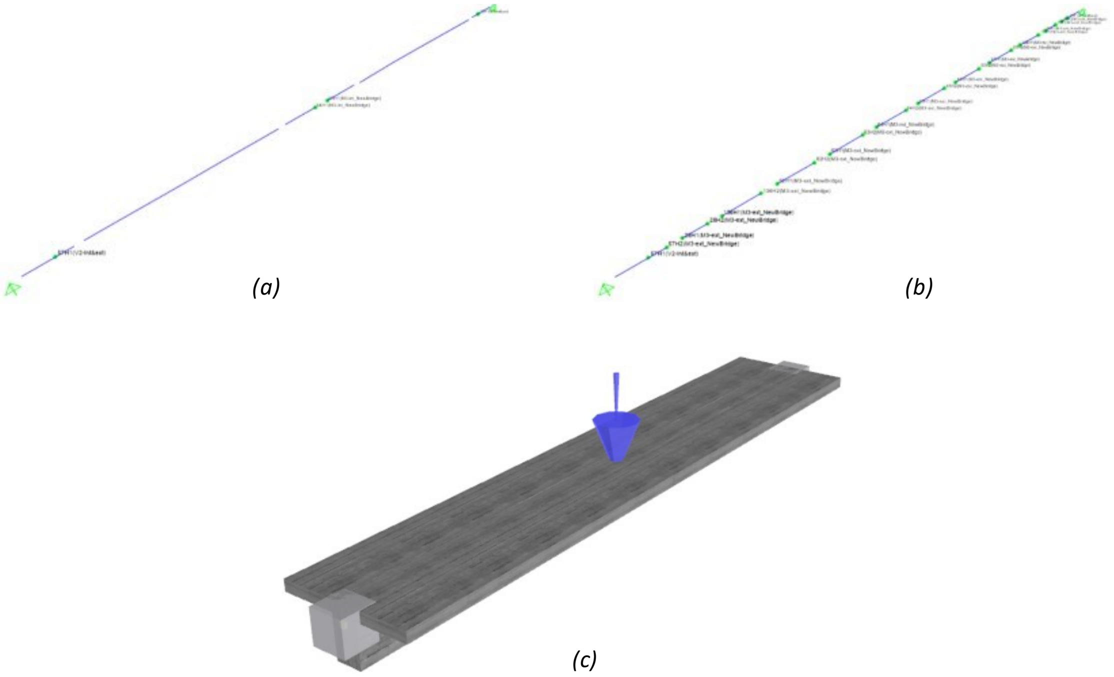
(a)

(b)

(c)

Figure 16: *Finite Element Non-Linear Models of Internal Girder in (a) SAP2000 - with one flexural hinge, (b) SAP2000 - With several flexural hinges, and (c) SeismoStruct*

At the element level, these models developed in SAP2000 and SeismoStruct are able to represent non-linear behavior. The objective of this verification is to ensure that the non-linear behavior of the bridge girder is accurately modeled. The 3D model of the bridge utilizing such components in individual girders is expected to perform well after the element level model has been validated. By applying a concentrated point load of 1000 kN at the center of the simply supported beam, a vertical pushover analysis (uniformly increasing vertical loads) has been performed on the beams by an increment of 1 kN load per step.

Table 1: *Moment-Curvature Comparison for Non-Linear Behavior of the Girder Sections*

Internal Girder						
State	**Manually**		**SeismoStruct**		**% Difference**	
	Moment	**Curvature**	**Moment**	**Curvature**	**Moment**	**Curvature**
Cracking	238.86	0.00014	237.01	0.00012	-0.78%	-18.47%
Yielding	1431.36	0.00280	1431.10	0.00277	-0.02%	-0.85%
Ultimate	1916.65	0.05756	2028.10	0.05327	5.81%	-7.45%

External Girder						
State	**Manually**		**SeismoStruct**		**% Difference**	
	Moment	**Curvature**	**Moment**	**Curvature**	**Moment**	**Curvature**
Cracking	243.82	0.00014	243.01	0.00011	-0.33%	-16.90%
Yielding	1440.51	0.00277	1440.10	0.00276	-0.03%	-0.29%
Ultimate	1953.78	0.06034	2067.10	0.05161	5.80%	-14.47%

The moment-curvature values obtained from SeismoStruct were compared with the one implemented in SAP2000 for both girders as shown in ***Table 1***, and a graph of the load-deflection curve for the internal girder is plotted for comparison as shown in ***Figure 17***. A similar graph was obtained for the external girder as well which is not shown here.

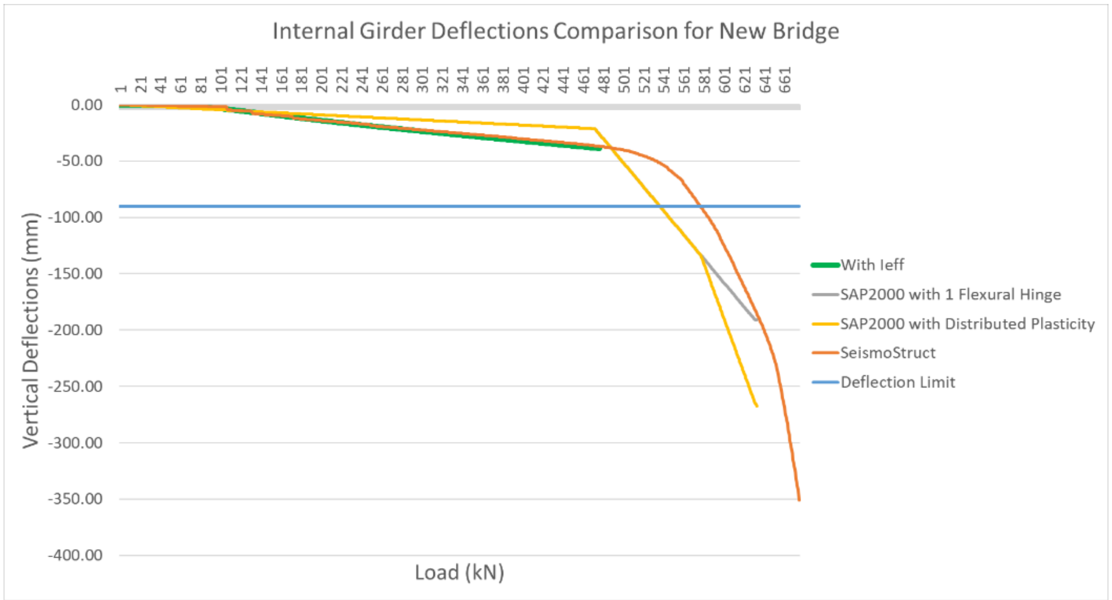

Figure 17: *Load Deflection Curve for Internal Girder*

The ultimate load and associated curvature values of plastic hinges calculated using two different software systems agree. The curvature values of the sections obtained by hand calculations when compared to the ones obtained from SeismoStruct are within the agreeable limit. The plastic hinge in the middle portion of the girders reaches its full capacity (limit of rotation) when the point loads reach **676 kN** and **689 kN** for internal and external girders, respectively. It was observed that the girder modeled in SeismoStruct carries 5.8% more load at ultimate which is considerable, this is due to the fact that it considers a non-linear material model for both concrete and steel. The deflection failure of 0.0075 of the span lengths is achieved before the section fails in the flexural mode. This is clear from ***Figure 17*** which shows that for both SAP2000 and SeismoStruct the failure in deflection is observed first rather than flexure. The deflection failure is obtained at **578 kN** and **584 kN** loads for internal and external girders in SeismoStruct. Also, it is clear that when one plastic hinge is assigned to the girder in SAP2000 its load-deflection behavior is bi-linear while the application of several hinges across the member length to distribute the plasticity results in a tri-linear load-deflection behavior. It is apparent from ***Figure 17*** that the deflection values obtained in the elastic zone from SeismoStruct are very near to the ones obtained from manual calculations using I_{eff} while it is different from SAP2000 due to the fact that its original trilinear moment-curvature relationship is converted into a bilinear moment-curvature relationship.

3.3.2.1 Validation using Response-2000

For further validation of the results for the girder, analysis is performed by comparing the results obtained from the Response-2000 program developed by Evan Bentz at the University of Toronto. Response-2000 is a simple sectional analysis program that determines the strength and ductility of a reinforced concrete cross-section under shear, moment, and axial loads. Using the research based on modified compression field theory, all three loads can be examined simultaneously to determine the whole load-deformation response of the section. Response-2000 can calculate the strength of conventional beams and columns as well as or better than previous techniques, and it can also make shear strength estimates for sections that are hard to analyze, such as circular columns and tapered web beams. Response-2000 allows the engineer to study beam and column behavior with a new degree of confidence and accuracy, due to its quick input and output, windows-based interface, and sufficient graphical output for simple checking of results (Bentz 2000).

Since the Response-2000 allows the modeling of the symmetric section, only the internal girder of the bridge section is modeled for comparison. ***Figure 18*** shows the cross-section of the internal girder modeled in Response-2000 while ***Figure 19*** shows the moment-curvature relationship results of the section.

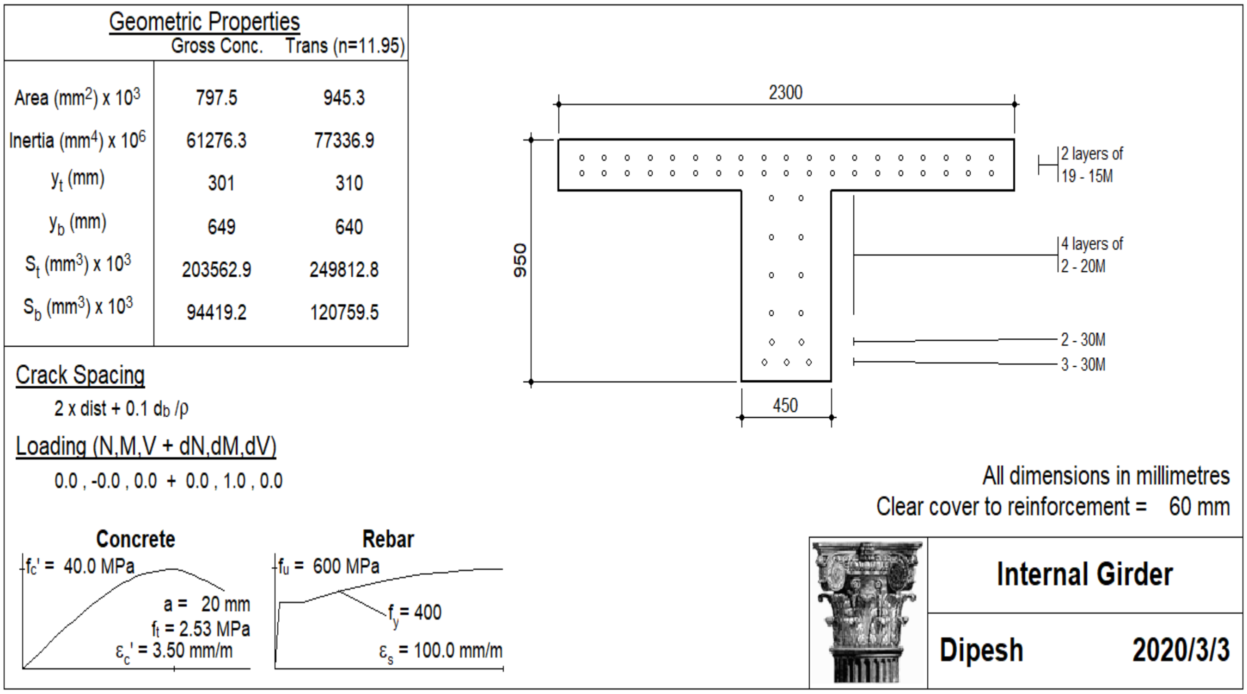

Geometric Properties

	Gross Conc.	Trans (n=11.95)
Area (mm^2) x 10^3	797.5	945.3
Inertia (mm^4) x 10^6	61276.3	77336.9
y_t (mm)	301	310
y_b (mm)	649	640
S_t (mm^3) x 10^3	203562.9	249812.8
S_b (mm^3) x 10^3	94419.2	120759.5

Crack Spacing

2 x dist + 0.1 d_b/ρ

Loading (N,M,V + dN,dM,dV)

0.0 , -0.0 , 0.0 + 0.0 , 1.0 , 0.0

Concrete

f_c' = 40.0 MPa

a = 20 mm

f_t = 2.53 MPa

ε_c' = 3.50 mm/m

Rebar

f_u = 600 MPa

f_y = 400

ε_s = 100.0 mm/m

All dimensions in millimetres

Clear cover to reinforcement = 60 mm

Internal Girder

Dipesh **2020/3/3**

Figure 18: *Internal Girder modeled in Response-2000*

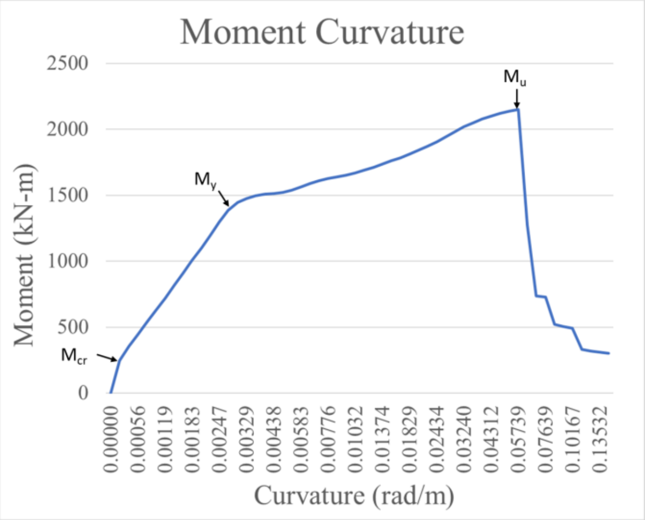

Figure 19: Moment Curvature Relation of Internal Girder obtained from Response-2000

Table 2 shows the results obtained from Response-2000 and SeismoStruct for comparison. Since the values obtained from Response-2000 are obtained for specific instances the comparative values are compared. It is important to note at the instance of the ultimate moment and curvature values calculated in Response-2000 the top concrete in compression had a strain value of -0.00382 which is slightly more than the failure mode in our case. While the corresponding values obtained from SeismoStruct were obtained at an instance just before the crushing of concrete in compression i.e., an instance before concrete reaching the strain value of -0.0035. Hence, from the results, it can be deduced that the behavior obtained from both the analysis program are fairly identical.

***Table 2**: Results comparison for Internal Girder obtained from Response-2000 and SeismoStruct*

Internal Girder						
State	**Response-2000**		**SeismoStruct**		**% Difference**	
	Moment	**Curvature**	**Moment**	**Curvature**	**Moment**	**Curvature**
Cracking	249.06	0.00014	237.01	0.00012	-4.84%	-14.89%
Yielding	1445.329	0.00299	1431.1	0.00277	-0.98%	-7.36%
Ultimate	2148.543	0.05738	2028.1	0.05327	-5.61%	-5.61%

3.4 Methodology of the Development of Non-Linear Reinforced Concrete Bridge Superstructure Model Using Fiber Elements

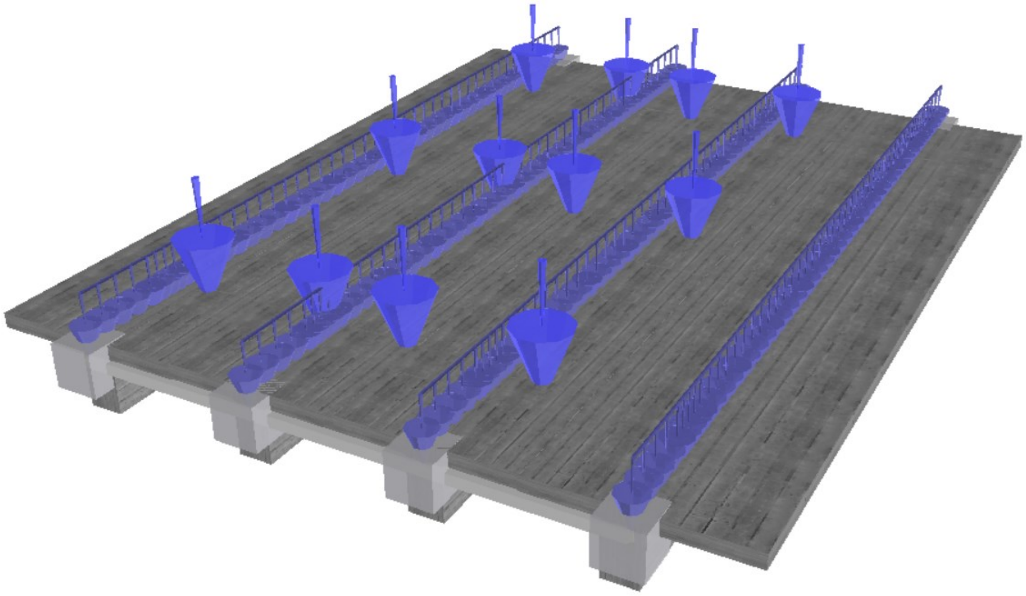

***Figure 20:** Finite Element Model of Bridge Superstructure in SeismoStruct*

After validating the results obtained for the bridge girders the full-scale bridge superstructure model is expected to work well. A 3D model of steel-reinforced concrete decks has been created in SeismoStruct 2018. The model developed in SeismoStruct 2018 based on the grillage analogy (Stallings and Yoo 1992) with non-linear bridge girder sections in the longitudinal direction while the transverse elements were modeled elastic (with the same stiffness as that of elements in SAP2000) as their behavior did not affect the performance of the entire bridge superstructure. The advantage of doing this was that it enhanced the processing time of the analysis. The advantage of this model is that a plastic hinge assignment is not required as the plasticity is distributed across the fiber components and controlled by the 3D yield criterion. ***Figure 19*** shows the 3D Finite Element Model of Bridge Superstructure modeled in SeismoStruct 2018.

3.4.1 Calibration

A similar 3D model of the steel-reinforced concrete bridge has been created in SAP2000 as shown in ***Figure 4***. The SAP2000 model is based on the grillage analogy (Stallings and Yoo 1992) as a planar grid of longitudinal (major T-section beam girders parallel to the highway) and transverse (perpendicular to the roadway) components, which was earlier calibrated with a comparable 3D model using shell elements by Ghodoosipoor (2013). The use of the grillage model with frame components, SAP2000, needs to assign the plastic hinge characteristics to the elements. For each plastic hinge in SAP2000, the hinge attributes must be calculated and assigned as user-defined hinge properties in the program. Here an attempt has been made to correlate both the SeismoStruct and SAP2000 models with each other. The stiffness of the elements is decreased to 40% of their original stiffness in the SAP2000 Model to account for the cracking effect. For the SeismoStruct model, the program is able to consider the cracking effect in performing a non-linear analysis, however for calibration by performing a linear static analysis in SeismoStruct the modulus of elasticity of concrete is reduced by 40% of its original elasticity. The Dead load and Live load are considered in the load distribution, as stated in ***Section 2.8.1***. Each truck has the same axle arrangement as the design truck, according to AASHTO as shown in ***Figure 5***. In terms of wheel spacing and axle loads, the AASHTO HS-20 design load and the Canadian CL-625 design load are significantly different, although they produce about the same design moments and shear forces (Wacker and Groenier 2010). The two tracks are arranged in a longitudinal orientation such that they create the highest bending moment. The wheels of the two neighboring trucks are 1.2 meters apart from their centerline. The two trucks are moved with six different transverse positions as shown in ***Figure* 6** as described by (Czarnecki and Nowak 2007).

3.4.1.1 Linear Static Analysis

Both the models exhibit the same deflection for different transverse locations of the two side-by-side design trucks (shown in ***Figure 6***) as described by Czarnecki and Nowak (2007). In order to capture the influence of all the features in the bridge superstructure, the SeismoStruct model is closely correlated with the previous SAP2000 model. ***Table 3*** shows the difference in deflection obtained in the SeismoStruct model when compared with the SAP2000 model for linear static analysis. It is apparent from the values that the maximum difference in deflection was observed in Girder – D for load case 6 which was -7.13%. The difference is well within the acceptable limit and hence both these models can be considered closely correlated.

Table 3: *Deflection Comparison for 3D Finite Element Model of New Bridge for Calibration*

Deflection Comparison at Center Nodes for Girders				
Load Case	**Girder - A**	**Girder - B**	**Girder - C**	**Girder - D**
Case 1	-4.29%	-0.94%	1.33%	3.34%
Case 2	-1.63%	-0.24%	0.68%	1.52%
Case 3	0.56%	0.43%	0.05%	-0.33%
Case 4	2.73%	1.04%	-0.62%	-2.55%
Case 5	4.43%	1.55%	-1.30%	-4.69%
Case 6	6.13%	2.01%	-2.09%	**-7.13%**

3.4.1.2 Non-Linear Pushover Analysis

The capacity of the bridge superstructure system was estimated using a non-linear pushover analysis of the Finite Element Model of the bridge. The magnitudes of truckloads depicted in ***Figure 6*** are gradually increased to attain the ultimate system capacity. When the flexural capacity of any girder is attained owing to concrete crushing in compression or tensile failure in reinforcing steel, or when any major girder deflects 0.0075 of the span lengths during a vertical pushover analysis (consistently increasing vertical loads), the system failure is reached. The yield strength of the reinforcing steel f_y, the modulus of elasticity of reinforcing steel E_s, the compressive strength of concrete f_c, the modulus of elasticity for concrete E_c, and the dimensions of the reinforced concrete members are the main structural parameters affecting the capacity of the bridge superstructure system used are described in ***Section 3.3.1***. The results of this thesis demonstrate that deflection control (0.0075 of the span length) is dominating mechanism of failure for a typical reinforced concrete bridge superstructure rather than the flexural collapse of structural components. During the simulations, it was discovered that the ultimate condition of a reinforced concrete bridge girder was determined by concrete crushing in compression (0.0035 strain value). The bridge capacity is determined by the gross vehicle weight (GVW) of two side-by-side trucks, which results in failure. The capacity of the bridge superstructure system was obtained as GVW of **1033.47 kN** due to the bridge girders failing in deflection. It was observed that the ultimate failure of the bridge superstructure was obtained at GVW of **1362.89 kN** with a difference of -8.73% when compared with those of SAP2000. Hence it was observed that after the deflection limit is reached the structure can still withstand 31.87% more live load.

The observations for linear and non-linear analysis conclude that the non-linear finite element model prepared in SeismoStruct is closely correlated to the previous SAP2000 model. For the rest of the simulations, the calibrated model of SeismoStruct based on the grillage analogy will be used to estimate the capacity of the bridge superstructure because it takes less computational time and is simpler as it does not need calculations to assign plasticity than the SAP2000 model.

3.5 Modeling Deteriorated Bridge Superstructure Model

Assuming that the drains are well maintained throughout the life of an overpass bridge, the only scenario considered in this thesis is when de-icing salt reaches the top surface of the beam through the permeable wearing surface and becomes airborne due to traffic beneath the bridge in the case of conventional steel-reinforced bridge decks. As a cautious assumption, all of the soffits of the beam and slab are contaminated with de-icing salt is assumed in this thesis. Corrosion of steel reinforcement leads to a decrease in bar diameter, resulting in a loss in structural element capacity. Spall or delamination results in a reduced capacity due to the concrete compression zone being reduced due to the depth of the spalled cover. The lower depth of the cross-section by one or both covers due to the spalling of the top or bottom cover results in reduced shear capacity (K. A. T. Vu and Stewart 2000). In this thesis, it is supposed that when delamination occurs, the spalled debris remains attached to the structure and does not fall down; as a result, the spalled zone does not contribute to the capacity of the bridge, but it is still regarded as a component of the dead load.

3.5.1 Deterioration in Reinforced Concrete

Due to the use of salt-based de-icing chemicals, the corrosion of steel reinforcement is the primary cause of deck deterioration. Early-age concrete cracking, corrosion initiation of steel reinforcement, cracking of the concrete cover, and delamination or spalling is the primary phases of damage to any reinforced concrete bridge deck exposed to chlorides. The surface chloride content of concrete C_s; effective chloride diffusion coefficient of concrete D_c; chloride threshold of the reinforcement C_{th}; corrosion rate of steel reinforcement λ; and concrete cover of steel reinforcement are the five variable parameters that primarily affect the prediction of service life of a steel-reinforced concrete deck, as discussed in ***Section 2.2***. In this thesis, the appropriate mean values of the field data are taken from the literature for the New York state, which is similar to the environmental situation in Canada, where significant amounts of deicing salt are utilized throughout the long and harsh winters, as explained in detail in ***Section 2.2.1***. Rebar corrosion and the subsequent spall and delamination of a concrete element are found to be significantly influenced by the concrete cover (Ghodoosipoor 2013). In this thesis, the reduction in the stiffness of the deteriorated bridge sections is performed by the reduction in rebar area due to corrosion and section loss due to the spalling.

Equation 2.2 is used to calculate the time for initiation of corrosion for the given bridge given in ***Section 2.2.2.*** The values of the parameters used in this ***Equation 2.2.2*** are given in ***Section 2.2.1***. After estimating the time for corrosion initiation, the rebar corrosion is considered and calculated for the bridge life span of 45 years with the help of ***Equation 2.12***. The value of the parameters used for the calculation of the area of rebar is given in ***Section 2.2.5***. The bridge age of 45 is considered in this thesis because the GPR defect map given in ***Section 2.10*** was made by scanning the portion of the bridge when it was at 45 years of age. The calculation of corrosion initiation and rebar corrosion are given in ***Appendix C***.

3.5.2 Uniform Deterioration Models

In this thesis, two uniform deteriorated bridge models are prepared in order to compare the results with the ones obtained from the deteriorated bridge model with defects modeled from the GPR map. In the first model, it is assumed that the soffit of the bridge deck has severely deteriorated while the top deck is with minor deterioration due to the rebar corrosion without any delamination. Hence in this bridge model, the concrete cover for the soffit of the bridge is considered as spalled while the top cover is considered intact. Also, the rebar area is calculated at the life span of the bridge at 45 years. In order to consider this for modeling, the bottom cover of the bridge section is removed while the load acting due to the spalled cover is added to the dead load of the bridge girders. Also, the reduced rebar area calculated is modeled for the girder sections used. This reduction in cross-section as well as the rebar cross-section results in the reduction in the structural strength of the bridge superstructure. ***Figure 20*** shows the bridge model with soffit deterioration where the soffit cover showed in light grey color is not considered in the sections modeled.

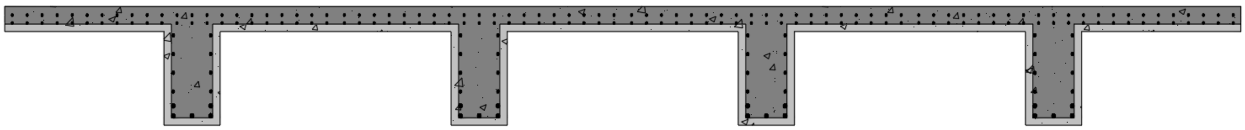

Soffit Deterioration At t = 45 years

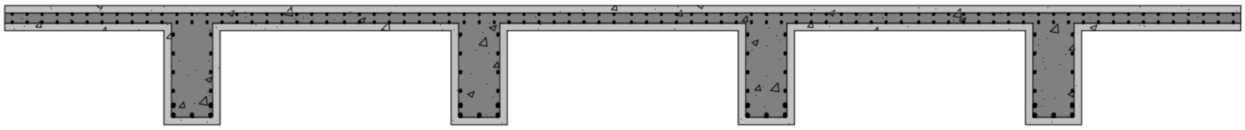

Full Deterioration At t = 45 years

Figure 21: *Bridge Model with Soffit Deterioration and Full Deteriorated at Life Span of 45 Years*

In the second uniform deteriorated bridge model, it is assumed for most unfavorable circumstances i.e., the top concrete as well as the bottom soffit cover are both spalled and do not contribute towards the structural strength of the bridge. For modeling the top, as well as the bottom concrete cover of the bridge sections, are removed, and the rebar area is reduced similar to the case of the bridge model with soffit deterioration and their load is added to the dead load. ***Figure 20*** shows a bridge model with full deterioration in which the top cover and the bottom cover of the bridge shown in light grey color are considered as spalled.

3.5.3 Procedure to Model Deteriorated Bridge with GPR Defect Map

In this model, a procedure similar to the one for uniform deterioration models is applied. Instead of assuming the uniform deterioration of the entire bridge deck, here only the deterioration of the portion of the bridge deck is considered as obtained from the GPR defect map. While the soffit is considered as uniformly spalled and the area of rebars at 45 years of the life span of the bridge are calculated and assigned. The deteriorated sections of the external girder used in this case are shown in ***Figure 22***. Similar sections were utilized for the internal girders as well.

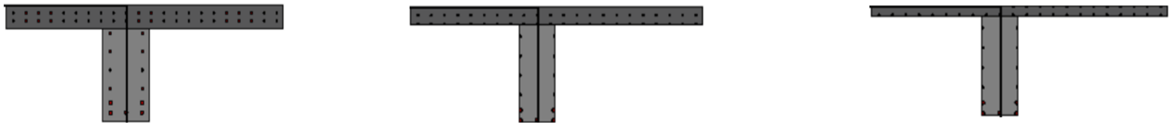

a) External Girder Section b) With Soffit Deterioration c) Full Deterioration

d) Internal side Deterioration e) Cantilever side Deterioration

Figure 22: *Deteriorated Sections Employed in Modeling*

Figure 22 shows five different sections: (a) External girder section: it shows the full girder section of the new bridge just after the construction, (b) Soffit Deterioration: this section is used when the top deck portion is intact while the soffit cover is considered spalled, (c) Full Deterioration: this section is used when it is assumed that both the top as well bottom concrete cover of the bridge section has spalled, (d)

Internal side Deterioration: this section has spalling only on one portion of bridge deck here on its internal side, and (e) Cantilever side Deterioration: here only the cantilever side of the deck of external girder is considered spalled. It is important to note here that the sections (b)-(e) all have been modeled considering their soffit as spalled and their area of reinforcement is calculated at 45 years considering uniform corrosion.

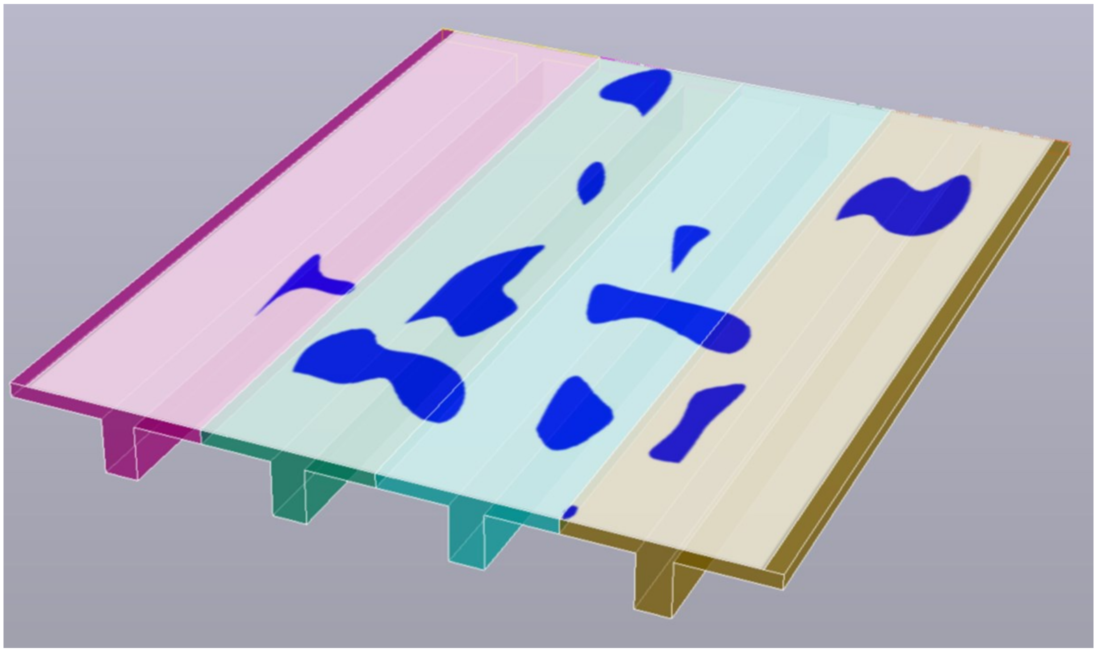

Figure 23: *Overlapping GPR Defect Map on Bridge Deck*

After defining these sections which will be used for deterioration modeling the next step is to find the locations on the bridge deck for their application. In order to do this the first step involves the superposition of the bridge deck with the GPR deterioration map. ***Figure 23*** shows the 3D bridge deck model superimposed by the GPR defect map given in ***Figure** 7*. This overlapping was performed in AutoCAD.

The second step involves super-positioning the grid of the grillage model in order to make the decision of applying the particular deteriorated section to a particular element. ***Figure 24*** shows such overlapping along with the explanation is provided about the section used for the external girder: where ***(a)*** shows the use of full deterioration section for bridge girder elements having delamination on both sides of its central line, ***(b)*** shows the use of soffit deterioration section where bridge elements do not possess delamination on its deck, and ***(c)*** shows the use of internal side deterioration section where the bridge elements have their delamination only on its internal portion. The use of these elements provides a better approximation for the modeling as the only thing needed is the change in the sections at important locations.

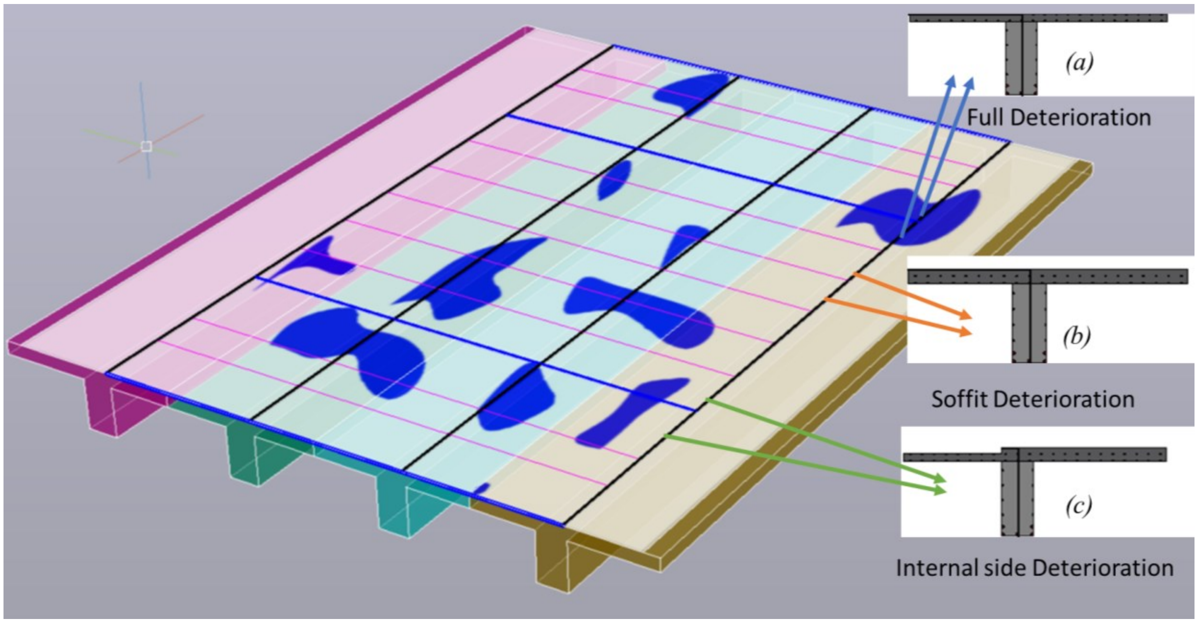

Figure 24: *Model Updating by Changing Sections by Using GPR Defect Map*

The bridge deterioration model provided in SAP2000 (explained in ***Section 2.10***) is also prepared for comparison. The problem with the SAP2000 model is the application of spalled and non-spalled hinges (also its calculations) which needs careful observation and decision effort for the modeling. Another disadvantage of this model is that the plasticity is concentrated at the locations where the flexural hinges are assigned. Both these disadvantages of deterioration modeling in SAP2000 are addressed by only changing the sections of the bridge model in SeismoStruct.

Chapter 4 Results

The results obtained for the Methodology employed in this thesis which is described in Chapter 3 are explained here along with a brief discussion.

4.1 Sub-subsurface Material Detection Using GPR

The results obtained from the laboratory experimental arrangements explained in ***Section 3.2*** are discussed below:

4.1.1 Amplitude Values for Sheets

The thickness of sheets was measured with a Vernier caliper scale with the least count of 0.02 mm since they were compressible. To determine the thickness of each sheet, five points were chosen on its periphery. The readings were averaged, and the thickness was calculated after being compressed with slab loads. Readings were taken with extreme caution to avoid further compression of the sheets. After the experiment, the thickness of paper sheets, cardboard sheets, and foam sheets was found to be 0.392 mm, 0.282 mm, and 0.496 mm, respectively. For each test, three random points were chosen at the desired depth (5 cm, 10 cm, or 15 cm) and their amplitude values were recorded and averaged in millivolts (mV). The amplitude of reflection for paper sheets was found to be the lowest, followed by cardboard sheets and foam sheets. Since the thickness of the paper was the thinnest, it was noticed that as sheet thickness increases, so does the amplitude of the reflection. When all these sheets were placed together, the amplitude of reflection was observed maximum. Although the amplitude value was slightly higher at 5 cm, for example, 1.4×10^6 mV for Paper Sheet at 5 cm depth, the difference between 10 cm (1.9×10^5 mV) and 15 cm (1.5×10^5 mV) depths was just a small difference. Finally, the loss of amplitude on average for all sheets decreases by 80% from 5 cm to 10 cm, whereas only by 9% from 10 cm to 15 cm. ***Figure***

25(a) depicts a graph of reflection amplitude for various sheets at depths of 5 cm, 10 cm, and 15 cm (Donda et al. 2021).

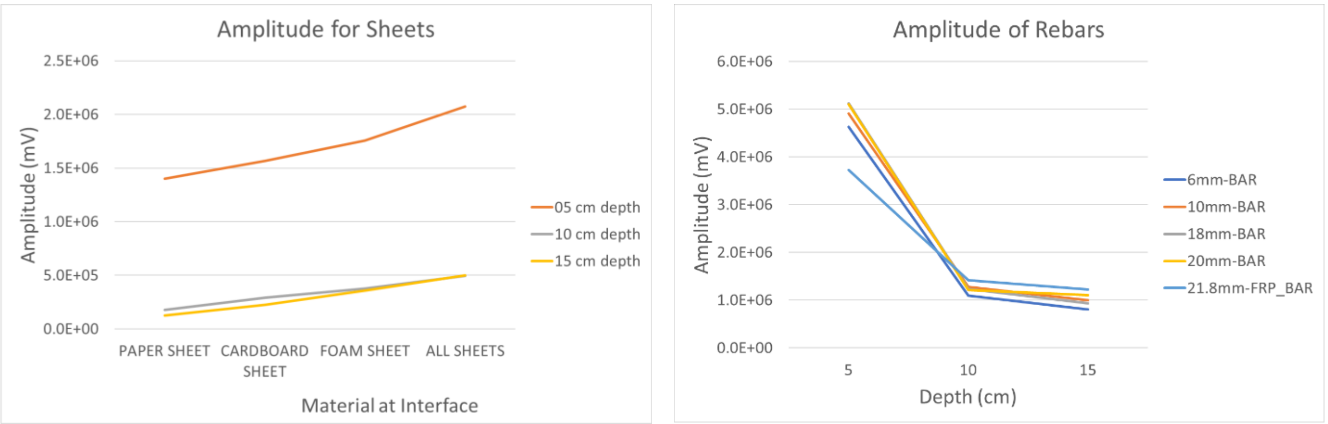

(a) (b)

Figure 25: *(a) Amplitude Values for Sheets, (b) Amplitude Values for Rebars (Donda et al. 2021)*

4.1.2 Amplitude Values for Rebars

Three GPR scans were conducted for each rebar size mentioned in ***Section 3.2.2*** at each depth (5 cm, 10 cm, and 15 cm) to verify lab test conformity. The reinforcement takes on a typical hyperbola form in B-Scan, and the amplitude value observed at its peak is averaged over three scans for each instance. It was observed that the amplitude value increases as the size of the rebar increases.

At a depth of 5 cm, the amplitude value rose from 4.6 x 10^6 mV for 6 mm rebar to 5.1 x 10^6 mV for 20 mm rebar (10% increase). The 21.8 mm diameter FRP bar was the outlier in the research results due to the different dielectric properties of this material compared to steel reinforcing bars. Similarly, the amplitude value for each rebar reduced from 5 cm to 10 cm, and when averaged, the value decreased by 76%. Furthermore, there is a notable reduction in amplitude for the depths greater than 10 cm (41% for 10 to 15 cm). While every size of rebar has a substantial variation in amplitude drop with regard to depth, the size of rebar has a much lesser influence on the amplitude value at a particular depth, making it difficult to analyze in a realistic scenario. ***Figure 25(b)*** shows the amplitude of reflection for various sizes of rebars including the FRP bar (Donda et al. 2021).

4.1.3 Amplitude Values for Air and Water Gaps

Similar to rebar, each test for compliance for both air and water gaps was done three times. ***Figure 26(a)*** shows the results for air gaps, whereas ***Figure 26(b)*** shows the results for water gaps.

Air Gaps: The amplitude value increased with the increase in gap size at all depths for air gaps. The amplitude value increased by 38% at a depth of 5 cm, from 3 mm (1.6 x 10^6 mV) to 8.8 mm (2.2 x 10^6 mV). When the depth was increased from 5 cm to 10 cm, there was a significant drop in amplitude (78%) for all air gaps. Moreover, the average increase in amplitude from 10 cm to 15 cm seemed inconsistent (17%). The skewed correlation can be explained by the poor signal reflection in air gaps at those depths compared to solid objects like rebar.

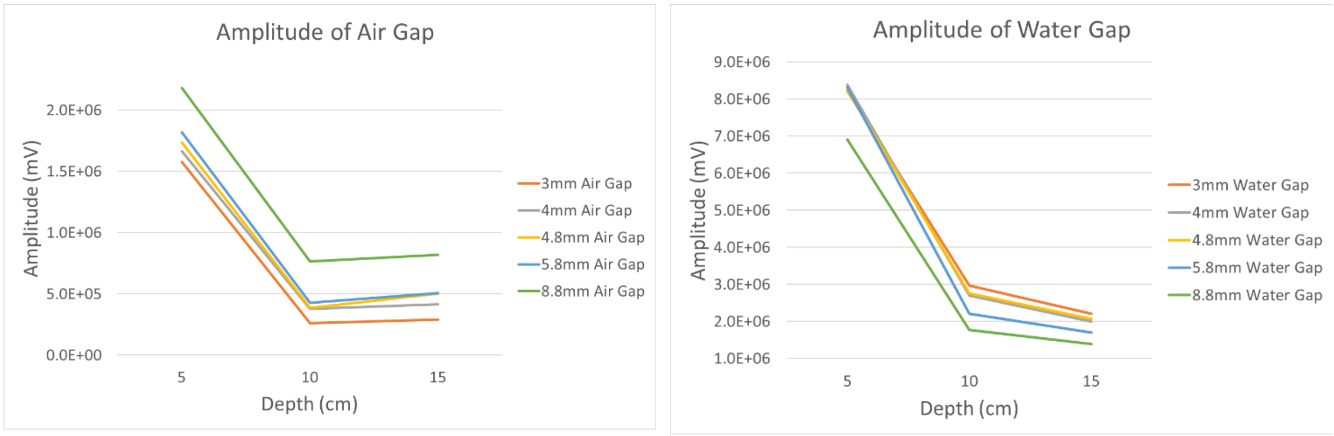

(a) (b)

Figure 26: *Amplitude for (a) Air Gaps, and (b) Water Gaps*

Water Gaps: The results of the water gap study differed significantly from those of other materials. The amplitude values for depths ranging from 3 mm to 5.8 mm were fairly consistent. The amplitude dropped for the water gaps from 5.8 mm to 8.8 mm (90% average averaged for all depths). The GPR signal is significantly influenced by water and/or the action of moisture, which explains the discrepancy. Small water gaps (3 mm to 5.8 mm) had less attenuation, as seen by higher amplitude values. Moreover, when the water gap widens the results show that the reflections weaken, as seen by the lower value for the 8.8 mm water gap. Meanwhile, for depths of 5 cm to 10 cm, a consistent significant average drop in amplitude (70%) was found across all water gaps. Similarly, across all water gaps, a constant but small drop in amplitude (24%) was found for depths of 10 cm to 15 cm.

4.1.4 Amplitude for Various Concentration of Salt Solution

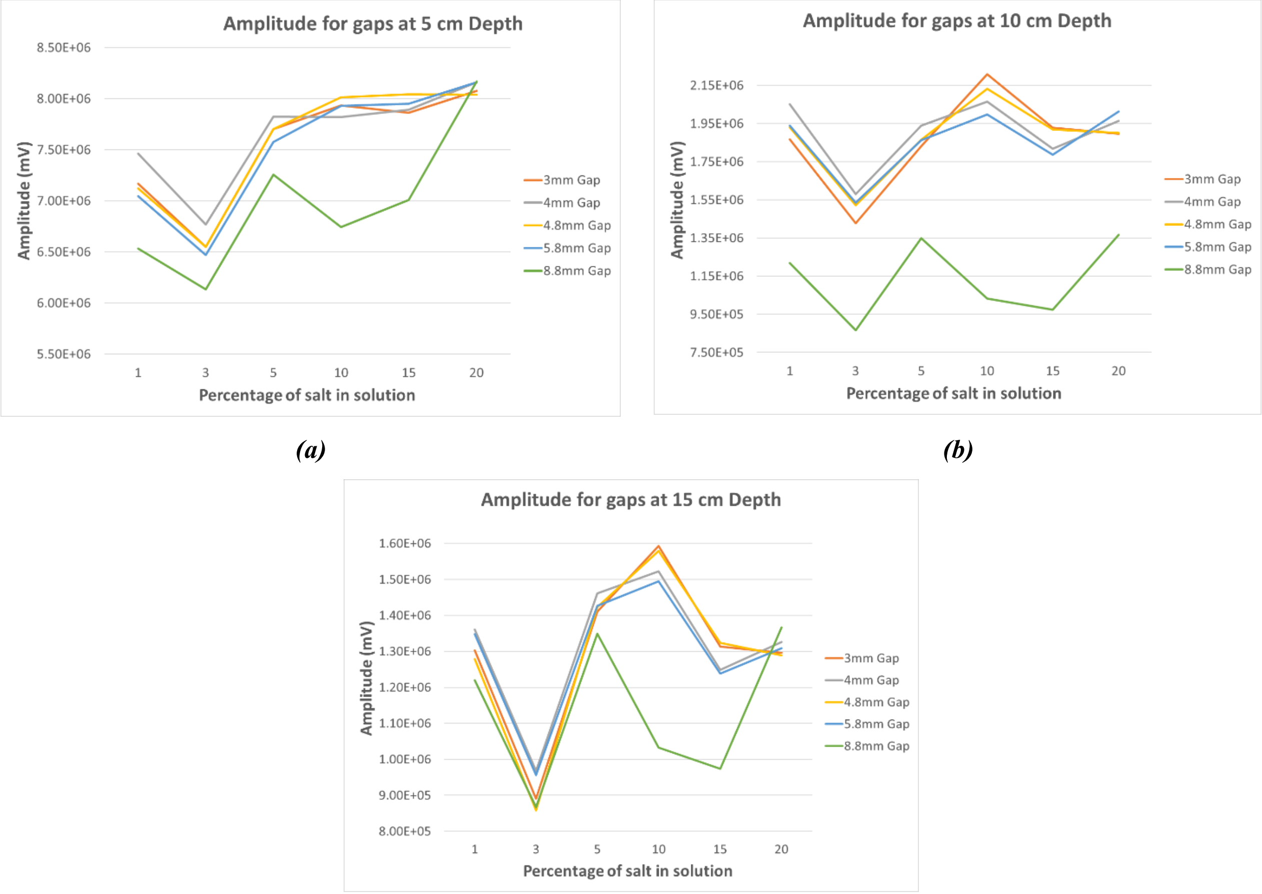

(a) ***(b)***

(c)

Figure 27: *Results of the amplitude of reflection for 1%, 3%, 5%, 10%, 15%, and 20% salt solution for (a) gaps at 5 cm depth (b) gaps at 10 cm depth, and (c) gaps at 15 cm depth*

Results of the amplitude of reflection for 1%, 3%, 5%, 10%, 15%, and 20% salt solution are shown in ***Figure 27(a)*** for the gap at 5 cm depth, ***Figure 27(b)*** shows the gap at 10 cm depth, and ***Figure 27(c)*** shows the gap at 15 cm depth.

With different concentrations of salt solution, an attempt was conducted to see if GPR can demonstrate consistent variance in the examined amplitude of reflection. For all salt solution percentages at any depth, the results found for all gaps were closer to each other. The amplitude values for a depth of 15 cm, for example, ranged from 0.87 x 10^6 mV to 1.64 x 10^6 mV. Hopefully, for all salt solutions, the values of amplitude must show an increasing trend as the gap size increases. However, a steady pattern with increasing percentages of salt solution could not be determined from observed values. As a result, GPR cannot reliably detect increasing salt concentrations in water. The reason for this disparity is that GPR signals are sensitive to the presence of water/moisture as well as soluble contaminants (salt), as previously noted. However, as in the case of air and water gaps, signal attenuation values decrease as depth increases in salt solutions.

4.1.5 Comparison of Different Materials

The amplitude data could be used to compare signal attenuation for different materials (rebars; air, water, and salt solution gaps). Because rebars and gaps varied in size, an average value was chosen for each material at each depth for a reliable comparison. For example, the amplitude values tested for all rebar sizes (6 mm to 20 mm) were averaged and obtained as 4.94 x 10^6 mV to provide a resultant amplitude value for different rebar sizes at 5 cm depth. Because the FRP rebar values were an exception due to their different dielectric properties than steel, they were ignored. ***Table 4*** displays the averaged amplitude values for all materials at each depth.

Table 4: *Amplitude comparison for various materials with variable depths*

Amplitude (mV)				
Depth↓	Rebars	Air Gaps	Water Gaps	Salt Solution
5 cm	4.94×10^6	1.80×10^6	8.02×10^6	7.46×10^6
10 cm	1.21×10^6	4.44×10^5	2.48×10^6	1.82×10^6
15 cm	7.12×10^5	5.06×10^5	1.87×10^6	1.27×10^6

Because deeper depths result in less reflected signals, the trend should be consistent across all materials. Because the amplitude values decrease with depth, they produce consistent findings for rebars and water gaps. However, as discussed in previous results, the amplitude values did not produce consistent results for air gaps and salt solution. The findings also show that at a given depth, water gaps produce the most reflections, followed by a salt solution, then by rebars, and finally air gaps. Using GPR, the range of these values might be used to distinguish between different subsurface materials. Furthermore, signal reflection loss is larger from a depth of 5 cm to 10 cm across all materials as compared to loss from 10 cm to 15 cm. This shows that the attenuated signals lose a lot of energy as they get closer to the surface. To summarize, GPR can be used to discriminate distinct subsurface materials at varying depths based on evaluated criteria.

4.2 Non-Linear Analysis of a Deteriorated Reinforced Concrete Bridge

Considering the value of surface chloride content of concrete (C_s) as 8.8 kg/m^3, effective chloride diffusion constant (D_c) as 84 mm^2/year, the depth of clear concrete cover of rebar as 60 mm, and the threshold chloride content for the initiation of corrosion (C_{th}) as 0.71 kg/m^3 by using ***Equation 2.2*** the time for initiation of corrosion obtained is 7.34 years. In this thesis, a constant current density (i_{corr}) of 1.5 µA/cm^2 is considered for the corrosion of reinforcement. This results in a constant corrosion rate (λ) of the reinforcement bars of 0.0174 mm/year. The reduction in diameter and area of rebars due to this corrosion rate for a time span of 100 years is shown in ***Figure 28***. It is clear from the figure that the diameter and area of the rebar reduce linearly from the assumed corrosion model. The initial diameter and the area of the reinforcement bars as well as those calculated at the age of 45 years for the rebars used are shown in ***Table 5***.

Table 5: *Area of Reinforcement Bars used at time 0 and 45 years.*

Rebar	At life t =0 year		At life t =45 year	
	Diameter (mm)	Area (mm^2)	Diameter (mm)	Area (mm^2)
15M	16	200	14.69	169.47
20M	19.5	300	18.19	259.85
30M	29.9	700	28.59	641.95

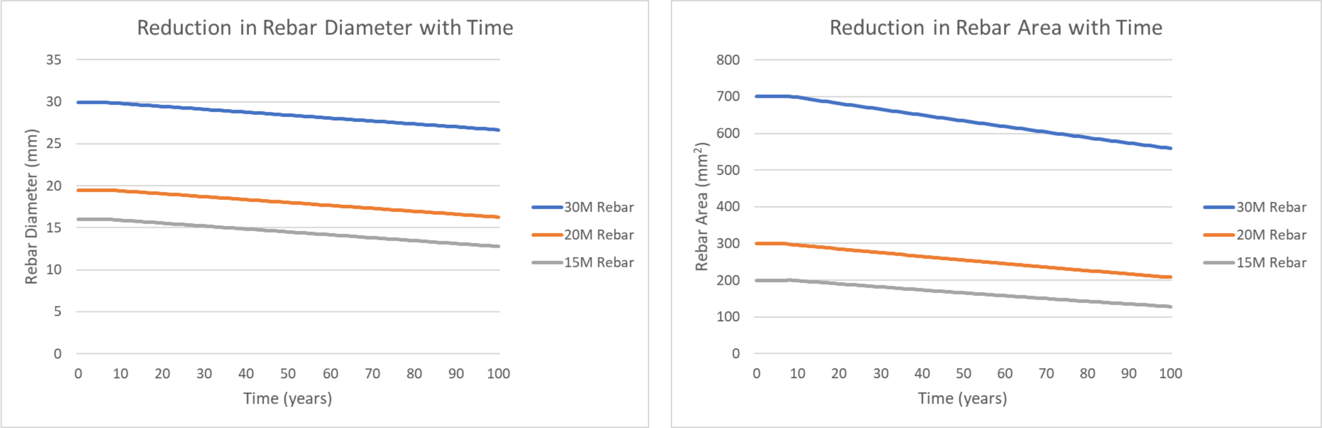

(a) (b)

Figure 28: *Reduction in (a) Diameter and (b) Area of Reinforcement bars due to Corrosion with Time*

It was observed in this model that the failure of the bridge superstructure occurs in serviceability due to excessive deflection rather than a failure in flexure. It was observed that the ultimate failure in flexure of the bridge model with the GPR map deterioration in SAP2000 was obtained at **1100.13 kN** and the failure in SeismoStruct was observed at **1165.16 kN.** The difference in the observed value of ultimate failure was only 5.91% which explains that the new finite element model in SeismoStruct is able to model the deterioration with ease and accuracy.

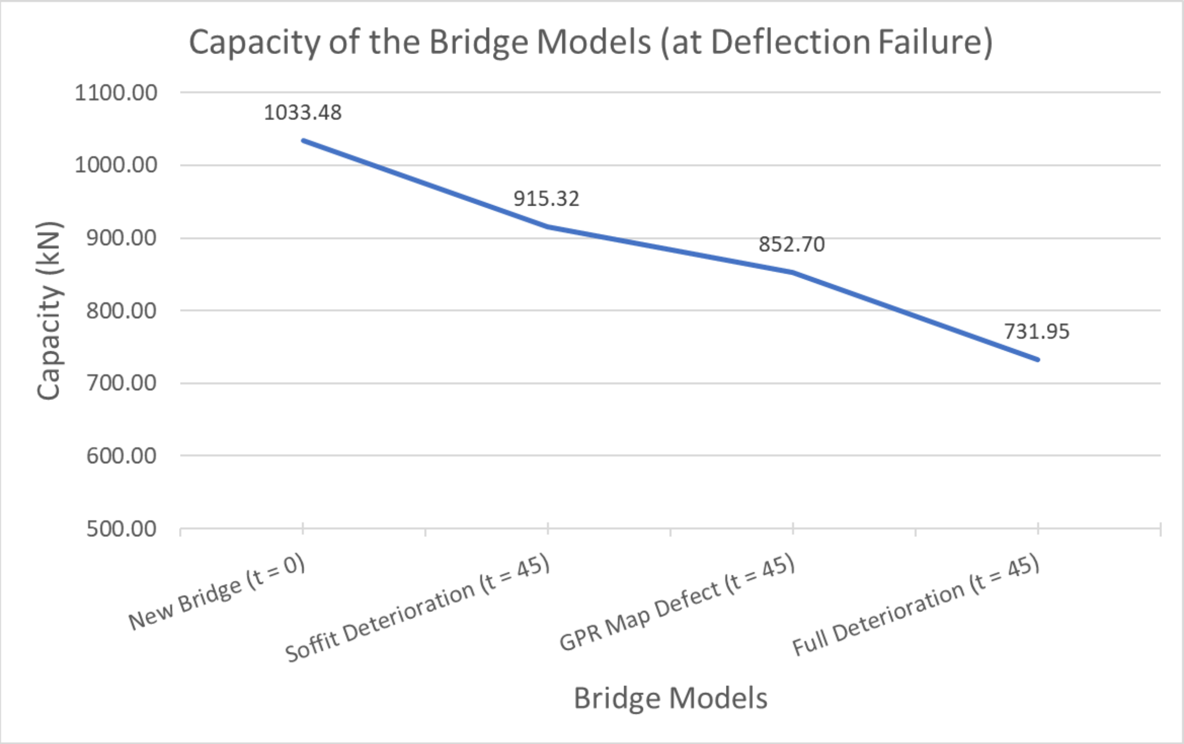

Figure 29: *The Capacity of Bridge Models Observed at Deflection Failure*

Figure 29 shows the capacity of the bridge models observed due to their failure in deflection. The X-axis gives the model details while the Y-axis represents its capacity. The new bridge model mentioned in this graph is the model used for the calibration in ***Section 3.4.1***. The capacity of the bridge model with the GPR map deterioration is higher than the full deterioration bridge model and lower than the soffit deterioration bridge model which is the expected result.

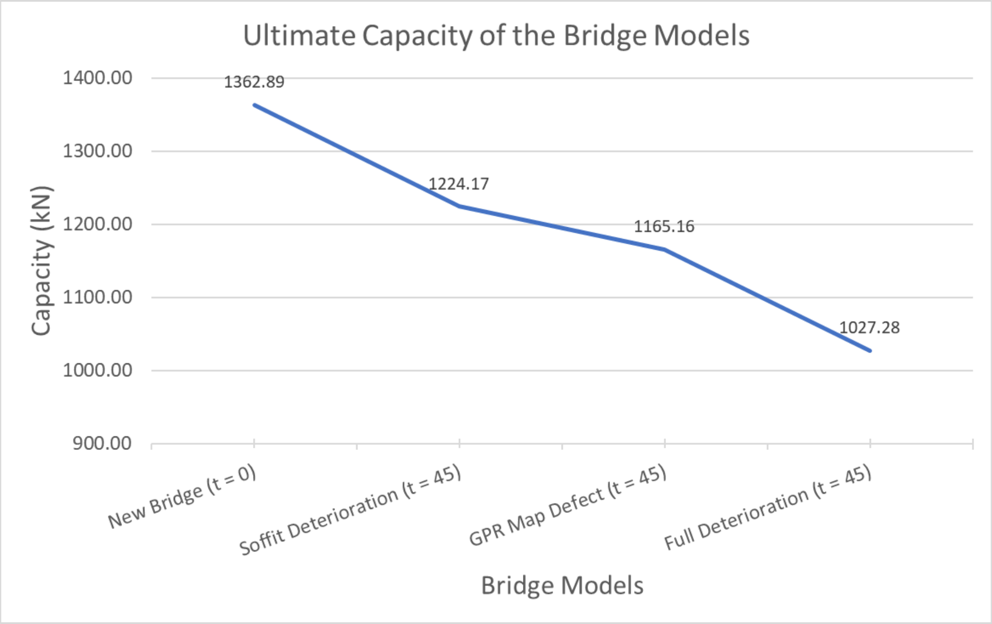

Figure 30: *Ultimate Capacity of the Bridge Models*

Figure 30 shows the ultimate capacity of the bridge models obtained due to the failure in flexure. The graph has a similar pattern to the one obtained at deflection failure. It was observed as an average for all models that the ultimate capacity is 35.65% higher than the failure obtained from the deflection failure.

Chapter 5 Conclusions and Recommendations

5.1 Summary and Conclusions

5.1.1 Summary

The structural health monitoring of the bridges is very important as if they remain uninspected the damage will add up and result in the reduction of the structural capacity. Hence, the Non-Destructive Evaluation techniques provide ease in monitoring without damaging the structure. The data obtained from the NDE techniques need a thorough analysis to find the location and amount of damage that occurred. Ground Penetrating Radar Imaging is becoming popular in the past decade as it allows the collection of data over a large portion faster and easily. With the data obtained from GPR after postprocessing, experts can pinpoint the location of severe damage which is due to corrosion of steel reinforcement bars as well as resulting delamination in concrete. The data obtained from the GPR can be used for the finite element model updating of the structure which can be an effective tool in evaluating and predicting the structural strength. This helps the decision-makers in planning a cost-effective strategy in the repair and rehabilitation of the structure.

The experimental observations in this research have shown us that the amplitude of GPR changes with materials as well as its depth or thickness. This will be helpful in the future to improve the post-processing of the GPR data and see delamination as a separate entity rather than always relating it with the rebar corrosion. The new finite element model of a simply supported steel-reinforced concrete bridge prepared here proves effective and saves time due to fewer calculations involved for the modeling and analysis. The model updating procedure discussed here using the GPR data will help to model the damage that occurred in the structure more precisely as well as estimate and predict its capacity, the results of which will help in planning the repair and retrofitting of the bridge infrastructure.

5.1.2 Conclusions

In this thesis, an experimental approach is devised to study the change in GPR amplitude with change in different materials, their thickness, and their depth of occurrences. This thesis also provides a model updating procedure of a simply supported reinforced concrete bridge superstructure using the Ground Penetrating Radar defect map. The following are some of the conclusions that can be drawn:

1. The experimental observation obtained in this thesis of simulated air, water, and salt-solution gaps shows that these parameters affect the amplitude of the GPR signals which should not be interpreted as structural deterioration. As the moisture contents reduce the attenuation of the signal reduces. The rate of such reduction is highest when the concrete is saturated. The addition of salt further attenuates the signal. This type of experimental data could be used for calibration of GPR images of concrete slabs to remove the effects of moisture and salt and contain the actual measure of deterioration or delamination.

2. The data obtained for real structure from amplitude comparison will prove to be helpful in making a detailed defect map showing rebar corrosion as well as the cracks and/or delaminations. This detailed defect map in turn could be used for finite element model updating which is demonstrated in the thesis.

3. The finite element model made here in this thesis provided insight into the structural behavior of the bridge, which could not be determined only from the GPR data. Based on the capacity of the bridge its performance could be estimated objectively.

With the timely inspection of the bridge, the data obtained from the Ground Penetrating Radar could be used for the finite element model updating of the bridge structure. This will help in reevaluating its capacity and performance. The changes in the performance of the structure will be helpful in predicting the future reduction in its performance. This prediction can prove to be useful in planning a cost-effective repair strategy that can prevent the premature failure of the structure.

5.2 Research Contributions

This thesis demonstrates from the laboratory experiment that the horizontal cracks or delaminations present in the concrete could be detected with the help of the ground-penetrating radar whether they contain air, water, or salt solution. The presence of cracks or delamination can be inferred from the amplitude values. The amplitude of GPR varies due to the presence of the materials in the crack which varies with the depth of the crack, material present, and its thickness. This observation could be utilized for the bridge data to detect the possible presence of delaminations separately from the rebar corrosion. As the delaminations might be present due to other reasons apart from due to corrosion cracking. This will be helpful in analyzing the GPR data with more accuracy.

This thesis illustrates a novel finite element model updating procedure of the bridge superstructure which is simple and easy to update than a traditional grillage model to which the plasticity is assigned by means of hinges. The developed model is able to capture the behavior of load-deflection and moment-curvature more accurately than the previous grillage model having a bi-linear or tri-linear nature. It also eliminates the calculations involved in the calculation of the moment and curvatures for cracking, yielding, and ultimate in order to assign the plasticity to the plastic hinges. The model updating requires only the changing of the cross-section of the elements with deterioration while the plasticity of the model is calculated by the program itself while in traditional model involves not only changing of the sections but also assigning the spalled hinges and non-spalled hinges at their respective locations. This research provides an insight that the entire bridge superstructure could be modeled and deterioration can be implemented to measure its capacity and captures the response of the structure. Hence this model proves to be very easy to use as well as more efficient which has a great potential to be used for a real bridge.

In the finite element model developed the data from other Non-Destructive Evaluation methods could also be implemented or the combined results of many methods can be used in order to make the model more precise based on the actual condition of the bridge. This helps decision-makers for assessing the condition of the bridge.

5.3 Research Limitations

The limitation of the laboratory experiment discussed in this thesis are:

1. The slabs used in this experiment were plain concrete slabs with small dimensions. This limits the depth of study of the experiment due to the fact that GPR has a reflection near the edges of the slab. Hence, a similar experiment needs to be conducted with steel-reinforced concrete slabs of larger dimensions.

2. The gaps which are simulated to detect cracks and potential delamination in the concrete are uniform since they are present between two slabs while in actual case the cracks are irregular in shape. Hence further investigation is required to study the actual cracks.

The limitation of the proposed finite element bridge model are:

1. The same structural parameters are used here for the updated model as a new bridge however in reality this is not the case there is some variance in the structural properties of concrete and steel. Hence, an additional examination needs to be performed in order to model the deterioration

accurately.

2. The accuracy of the results is directly related to the accuracy of the deterioration pattern and defect maps obtained from the GPR. The inability to detect the accurate material deterioration can result in a less accurate developed GPR map. Thus, this defect map affects the final results of the analysis.

3. The parameters used for the calculation of corrosion initiation as well as the corrosion rate may vary in actual cases and are very complex to analyze. Here a uniform corrosion rate is assumed however in real cases the corrosion rate is high initially and then reduces with time. To discover the amount of possible steel corrosion further data from assessment methods such as coring, half-cell potential, chloride analysis, or other analytical techniques are required.

4. Here the finite element model of bridge superstructure is updated by considering the GPR defect map only, however, the data obtained from other NDE methods could be implemented in order to obtain a more accurate model.

5. The results obtained from the FE model are conservative because of the uniform reduction of rebar area due to corrosion, uniform spalling of the bridge soffit as well as assignment of section reduction to an element despite the fact only a small portion was spalled.

6. In this finite element model, the reduction in the area of rebar is considered with corrosion however the change in the bond strength between steel and concrete is not discussed.

5.4 Potential Future Research

This research done in the laboratory could be enhanced by:

1. Using the reinforced concrete slabs of bigger dimensions with the study of similar or more parameters.

2. Simulating actual crack or delamination in concrete by means of any mechanical stimulus or by inducing corrosion in reinforced concrete by using galvanostatic methods.

3. The observations of this study must be applied to actual concrete structures and needs to verify the interpretation with other NDE techniques.

4. Due to the development of machine learning the amplitude analysis could be performed by computer programs in the future to provide a detailed defect map that includes rebar corrosion and cracks/delaminations along with the presence of air, water, or salt in those cracks.

The finite model updating understudy could be enhanced by:

1. Considering the actual structural parameters of the bridge structure in the model updating procedure. This will give a more precise updated model.

2. Using probabilistic methods to obtain deterioration prediction curves.

3. The parameters used for the prediction of corrosion initiation and rebar corrosion vary for particular bridges. Hence the data from the actual bridge must be used for calculating the corrosion and cracking phenomenon.

4. This method uses steel reinforcement, however, the model for Fiber Reinforced Polymer (FRP) bars can also be addressed in the future.

5. For old bridges, the actual structural design data are not available. This needs a thorough examination of getting the dimensions of members, concrete cover, rebars used, the grade of concrete used, grade of steel used, etc. This procedure involves developing the Finite Element model from the scratch with evaluated parameters.

References

Akiyama, Mitsuyoshi, Mohamed Soliman, Fabio Biondini, and Dan M. Frangopol. 2019. “Structural Deterioration Mechanisms.” *Life-Cycle Design, Assessment, and Maintenance of Structures and Infrastructure Systems*: 1–31.

Alani, Amir M, Morteza Aboutalebi, and Gokhan Kilic. 2013. “Applications of Ground Penetrating Radar (GPR) in Bridge Deck Monitoring and Assessment.” *Journal of Applied Geophysics* 97: 45–54.

Ali, U. 2019. “A Comparison of Seismic Behavior of Reinforced Concrete Special Moment Resisting Beam-Column Joints vs. Weak Beam-Column Joints Using Seismostruct.” *JOURNAL OF MECHANICS OF CONTINUA AND MATHEMATICAL SCIENCES* 14(3). http://www.journalimcms.org/journal/a-comparison-of-seismic-behavior-of-reinforced-concrete-special-moment-resisting-beam-column-joints-vs-weak-beam-column-joints-using-seismostruct/.

American Concrete Institute. 2013. “228: 2R-13 Nondestructive Test Methods for Evaluation of Concrete in Structures.”

Amezquita-Sanchez, Juan Pablo, and Hojjat Adeli. 2016. “Signal Processing Techniques for Vibration-Based Health Monitoring of Smart Structures.” *Archives of Computational Methods in Engineering* 23(1): 1–15.

Andrade, Carmen, and M Cruz Alonso. 1994. “Values of Corrosion Rate of Steel in Concrete to Predict Service Life of Concrete Structures.” In *Application of Accelerated Corrosion Tests to Service Life Prediction of Materials*, ASTM International.

Andrade, Carmen, M Cruz Alonso, and Jose Antonio Gonzalez. 1990. “An Initial Effort to Use the Corrosion Rate Measurements for Estimating Rebar Durability.” In *Corrosion Rates of Steel in Concrete*, ASTM International.

Ann, K Y et al. 2010. “Service Life Prediction of a Concrete Bridge Structure Subjected to Carbonation.” *Construction and Building Materials* 24(8): 1494–1501.

ASTM D6087. 2015. “Standard Test Method for Evaluating Asphalt-Covered Concrete Bridge Decks Using Ground Penetrating Radar.”

ASTM D6432. 2019. “Standard Guide for Using the Surface Ground Penetrating Radar Method for Subsurface Investigation.”

Barnes, Christopher L, Jean-François Trottier, and Dean Forgeron. 2008. “Improved Concrete Bridge Deck Evaluation Using GPR by Accounting for Signal Depth–Amplitude Effects.” *NDT & E International* 41(6): 427–33.

Bayane, Imane, Sai G S Pai, Ian F C Smith, and Eugen Brühwiler. 2021. “Model-Based Interpretation of Measurements for Fatigue Evaluation of Existing Reinforced Concrete Bridges.” *Journal of Bridge Engineering* 26(8): 4021054.

Benedetto, Andrea. 2013. “A Three Dimensional Approach for Tracking Cracks in Bridges Using GPR.”

Journal of Applied Geophysics 97: 37–44.

Benedetto, Andrea, and Lara Pajewski. 2015. *Civil Engineering Applications of Ground Penetrating Radar*. http://www.springer.com/series/13593 (July 8, 2020).

Bentz, E C. 2000. "Sectional Analysis of RC Members." The University of Toronto, Ontario, Canada. http://www.ecf.utoronto.ca/~bentz/r2k.htm.

Bertolini, Luca. 2008. "Steel Corrosion and Service Life of Reinforced Concrete Structures." *Structure and Infrastructure Engineering* 4(2): 123–37. https://doi.org/10.1080/15732470601155490.

Broomfield, John P. 2007. "Corrosion of Steel in Concrete. Understanding, Investigation and Repair."

Caldecott, R et al. 1988. "Underground Mapping of Utility Lines Using Impulse Radar." In *IEE Proceedings F (Communications, Radar and Signal Processing)*, IET, 343–53.

Cantor, T R. 1984. "Review of Penetrating Radar as Applied to Nondestructive Evaluation of Concrete." *Special Publication* 82: 581–602.

Çatbaş, F Necati, Tracy Kijewski-Correa, and A Emin Aktan. 2013. "Structural Identification of Constructed Systems: Approaches, Methods, and Technologies for Effective Practice of St-Id." In American Society of Civil Engineers.

Chang, Che Way, Chen Hua Lin, and Hung Sheng Lien. 2009. "Measurement Radius of Reinforcing Steel Bar in Concrete Using Digital Image GPR." *Construction and Building Materials* 23(2): 1057–63.

Chang, Peter C, Alison Flatau, and S C Liu. 2003. "Health Monitoring of Civil Infrastructure." *Structural health monitoring* 2(3): 257–67.

CHBDC-S6. 2014. "Canadian Highway Bridge Design Code." *S6-2014*.

Chen, Hua-Peng, and Yi-Qing Ni. 2018. *Structural Health Monitoring of Large Civil Engineering Structures*. Wiley Online Library.

Chesné, Simon, and Arnaud Deraemaeker. 2013. "Damage Localization Using Transmissibility Functions: A Critical Review." *Mechanical systems and signal processing* 38(2): 569–84.

Conde, Borja et al. 2017. "Structural Assessment of Masonry Arch Bridges by Combination of Non-Destructive Testing Techniques and Three-Dimensional Numerical Modelling: Application to Vilanova Bridge." *Engineering Structures* 148: 621–38.

Cosenza, Edoardo, and Gaetano Manfredi. 2000. "Damage Indices and Damage Measures." *Progress in Structural Engineering and Materials* 2(1): 50–59.

Cusson, D., Z. Lounis, and L. Daigle. 2011. "Durability Monitoring for Improved Service Life Predictions of Concrete Bridge Decks in Corrosive Environments." *Computer-Aided Civil and Infrastructure Engineering* 26(7): 524–41.

Czarnecki, A. A., and A. S. Nowak. 2007. "Reliability-Based Evaluation of Steel Girder Bridges."

Proceedings of the Institution of Civil Engineers: Bridge Engineering 160(1): 9–15. http://www.icevirtuallibrary.com/doi/10.1680/bren.2007.160.1.9 (March 15, 2020).

Dabous, Saleh Abu, Salam Yaghi, Sabah Alkass, and Osama Moselhi. 2017. "Concrete Bridge Deck Condition Assessment Using IR Thermography and Ground Penetrating Radar Technologies." *Automation in Construction* 81: 340–54.

Daniels, David J. 2005. "Ground Penetrating Radar." In *Encyclopedia of RF and Microwave Engineering*, Hoboken, NJ, USA: John Wiley & Sons, Inc. http://doi.wiley.com/10.1002/0471654507.eme152 (July 8, 2020).

Diamanti, Nectaria, Antonios Giannopoulos, and Michael C Forde. 2008. "Numerical Modelling and Experimental Verification of GPR to Investigate Ring Separation in Brick Masonry Arch Bridges." *NDT & E International* 41(5): 354–63.

Dinh, K, T Zayed, F Romero, and A Tarussov. 2014. "Method for Analyzing Time-Series GPR Data of Concrete Bridge Decks." *Journal of Bridge Engineering* 20(6): 4014086.

Donda, Dipesh, Fawzi Latosh, Mohammed Abdul Rahman, and Ashutosh Bagchi. 2021. "Detection of Subsurface Defects in Concrete Slabs Using Ground Penetrating Radar." In *Proc.SPIE*, https://doi.org/10.1117/12.2582807.

Ellingwood, Bruce R. 2005. "Risk-Informed Condition Assessment of Civil Infrastructure: State of Practice and Research Issues." *Structure and Infrastructure Engineering* 1(1): 7–18. https://www.tandfonline.com/action/journalInformation?journalCode=nsie20 (August 12, 2020).

Engelund, Svend, and John D. Sørensen. 1998. "A Probabilistic Model for Chloride-Ingress and Initiation of Corrosion in Reinforced Concrete Structures." *Structural Safety* 20(1): 69–89.

Farrar, Charles R, Scott W Doebling, and David A Nix. 2001. "Vibration–Based Structural Damage Identification." *Philosophical Transactions of the Royal Society of London. Series A: Mathematical, Physical and Engineering Sciences* 359(1778): 131–49.

Farrar, Charles R, and Keith Worden. 2010. "An Introduction to Structural Health Monitoring." *New Trends in Vibration Based Structural Health Monitoring*: 1–17.

François, R., and G. Arliguie. 1999. "Effect of Microcracking and Cracking on the Development of Corrosion in Reinforced Concrete Members." *Magazine of Concrete Research* 51(2): 143–50. http://www.icevirtuallibrary.com/doi/10.1680/macr.1999.51.2.143 (July 8, 2020).

Frangopol, Dan M, and James P Curley. 1987. "Effects of Damage and Redundancy on Structural Reliability." *Journal of structural engineering* 113(7): 1533–49.

Gattulli, Vincenzo, and Leonardo Chiaramonte. 2005. "Condition Assessment by Visual Inspection for a Bridge Management System." *Computer-Aided Civil and Infrastructure Engineering* 20(2): 95–107. http://doi.wiley.com/10.1111/j.1467-8667.2005.00379.x (July 8, 2020).

Ghodoosi, Farzad, Ashutosh Bagchi, Tarek Zayed, and M Reza Hosseini. 2018. "Method for Developing and Updating Deterioration Models for Concrete Bridge Decks Using GPR Data." *Automation in Construction* 91: 133–41. https://doi.org/10.1016/j.autcon.2018.03.014 (March 15, 2020).

Ghodoosipoor, Farzad. 2013. "DEVELOPMENT OF DETERIORATION MODELS FOR BRIDGE DECKS USING SYSTEM RELIABILITY ANALYSIS." Concordia University.

Gillott, J E, and H Asgeirsson. 1975. "Practical Implications of the Mechanisms of Alkali-Aggregate Reactions." In *Alkali–Aggregate Reaction Preventative Measures, Symposium*, Reykjavik, 213–30.

Gjørv, Odd E. 2014. *Durability Design of Concrete Structures in Severe Environments*. CRC Press.

Gómez-Ortiz, D et al. 2007. "Joint Application of Ground Penetrating Radar and Electrical Resistivity Imaging to Investigate Volcanic Materials and Structures in Tenerife (Canary Islands, Spain)." *Journal of applied geophysics* 62(3): 287–300.

Government of Canada. 2015. "Road Transportation." *Transport Canada*: 1. https://www.tc.gc.ca/eng/policy/anre-menu-3021.htm (July 8, 2020).

Gucunski, Nenad, and S Nazarian. 2010. "Material Characterization and Condition Assessment of Reinforced Concrete Bridge Decks by Complementary NDE Technologies." In *Structures Congress*, 2010, 429–39.

Guo, Guohui, David Darwin, JoAnn Browning, and Carl E Locke Jr. 2006. *Laboratory and Field Tests of Multiple Corrosion Protection Systems for Reinforced Concrete Bridge Components and 2205 Pickled Stainless Steel*. University of Kansas Center for Research, Inc.

Hasan, Md Istiaque, and Nur Yazdani. 2016. "An Experimental Study for Quantitative Estimation of Rebar Corrosion in Concrete Using Ground Penetrating Radar." *Journal of Engineering* 2016.

Hassan, Jinane El, Philippe Bressolette, Alaa Chateauneuf, and Khaled El Tawil. 2010. "Reliability-Based Assessment of the Effect of Climatic Conditions on the Corrosion of RC Structures Subject to Chloride Ingress." *Engineering Structures* 32: 3279–87. www.elsevier.com/locate/engstruct (August 12, 2020).

He, K, and W D Zhu. 2011. "Structural Damage Detection Using Changes in Natural Frequencies: Theory and Applications." In *Journal of Physics: Conference Series*, IOP Publishing, 12054.

Helmerich, Rosemarie et al. 2012. "Multi-Tool Inspection and Numerical Analysis of an Old Masonry Arch Bridge." *Structure and Infrastructure Engineering* 8(1): 27–39.

Herrmann, Andrew W. 2013. "Asce 2013 Report Card for America's Infrastructure." In *IABSE Symposium Report*, International Association for Bridge and Structural Engineering, 9–10.

Hironaka, M C, R D Hitchcock, and J B Forrest. 1976. *Detection of Voids Underground and under Pavements*. CIVIL ENGINEERING LAB (NAVY) PORT HUENEME CA.

Hong, Shuxian et al. 2017. "Long-Term Monitoring of Reinforcement Corrosion in Concrete Using Ground Penetrating Radar." *Corrosion Science* 114: 123–32.

Hong, Shuxian, Wai-Lok Lai, and Rosemarie Helmerich. 2015. “Experimental Monitoring of Chloride-Induced Reinforcement Corrosion and Chloride Contamination in Concrete with Ground-Penetrating Radar.” *Structure and Infrastructure Engineering* 11(1): 15–26.

Islam, A K M, Frank Li, Hiwa Hamid, and Amer Jaroo. 2014. *Bridge Condition Assessment and Load Rating Using Dynamic Response.* Ohio. Dept. of Transportation. Office of Statewide Planning and Research.

Jaffer, Shahzma J, and Carolyn M Hansson. 2009. “Chloride-Induced Corrosion Products of Steel in Cracked-Concrete Subjected to Different Loading Conditions.” *Cement and Concrete Research* 39(2): 116–25. https://www.sciencedirect.com/science/article/pii/S000888460800210X.

Jana, Dipayan. 2007. “Delamination–A State-of-the-Art Review.” In *Proceedings of the Twenty-Ninth Conference on Cement Microscopy*, Quebec City, QC, Canada, 135–67.

Jones, Casey, Sivakumar Ramanathan, Prannoy Suraneni, and W. Micah Hale. 2020. “Calcium Oxychloride: A Critical Review of the Literature Surrounding the Formation, Deterioration, Testing Procedures, and Recommended Mitigation Techniques.” *Cement and Concrete Composites* 113(April): 103663. https://doi.org/10.1016/j.cemconcomp.2020.103663.

JSCE, Japan Society of Civil Engineers. 2002. “Standard Specifications for Concrete Structures (Materials and Construction).”

Kaouk, Mohamed, and David C Zimmerman. 1994. “Structural Damage Assessment Using a Generalized Minimum Rank Perturbation Theory.” *AIAA Journal* 32(4): 836–42.

Khatri, R P, and Vute Sirivivatnanon. 2004. “Characteristic Service Life for Concrete Exposed to Marine Environments.” *Cement and concrete research* 34(5): 745–52.

Kim, Namgyu, Sehoon Kim, Yun-Kyu An, and Jong-Jae Lee. 2021. “A Novel 3D GPR Image Arrangement for Deep Learning-Based Underground Object Classification.” *International Journal of Pavement Engineering* 22(6): 740–51. https://doi.org/10.1080/10298436.2019.1645846.

Klemm, W A, and R L Berger. 1972. “ACCELERATED CURING OF CEMENTITIOUS SYSTEMS BY CARBON DIOXIDE Part I. Portland Cement.” *CEMENT and CONCRETE RESEARCH* 2(5): 567–76. https://doi.org/10.1016/0008-8846(72)90111-1 (August 10, 2020).

Kovacs, Austin, and Rexford M Morey. 1983. “Detection of Cavities under Concrete Pavement.”

Krause, Vincent, Ikhlas Abdel-Qader, Osama Abudayyeh, and Sherif Yehia. 2007. “An Image Segmentation Algorithm for the Detection of Rebar in Bridge Decks from GPR Scans.” *2007 IEEE International Conference on Electro/Information Technology, EIT 2007*: 114–19.

Kubat, Thamer, Riadh Al-Mahaidi, and Ahmad Shayan. 2016. “CFRP Confinement of Circular Concrete Columns Affected by Alkali-Aggregate Reaction.” *Construction and Building Materials* 116: 98–109.

Lahouar, Samer, and Imad L Al-Qadi. 2008. “Automatic Detection of Multiple Pavement Layers from

GPR Data." *NDT & e International* 41(2): 69–81.

Lam, H F, C T Ng, and M Veidt. 2007. "Experimental Characterization of Multiple Cracks in a Cantilever Beam Utilizing Transient Vibration Data Following a Probabilistic Approach." *Journal of sound and vibration* 305(1–2): 34–49.

Li, Hongyi. 2005. *Dynamic Response of Highway Bridges Subjected to Heavy Vehicles.* https://diginole.lib.fsu.edu/islandora/object/fsu%3A181267/datastream/PDF/view (July 8, 2020).

Liu, Hai et al. 2020. "Detection and Localization of Rebar in Concrete by Deep Learning Using Ground Penetrating Radar." *Automation in Construction* 118: 103279.

Liu, Lanbo, and Tieshuan Guo. 2005. "Seismic Non-Destructive Testing on a Reinforced Concrete Bridge Column Using Tomographic Imaging Techniques." *Journal of geophysics and engineering* 2(1): 23–31.

Liu, Youping, and Richard E. Weyers. 1998. "Modeling the Time-to-Corrosion Cracking in Chloride Contaminated Reinforced Concrete Structures." *ACI Materials Journal* 95(6): 675–81.

Loizos, Andreas, and Christina Plati. 2007. "Ground Penetrating Radar: A Smart Sensor for the Evaluation of the Railway Trackbed." In *2007 IEEE Instrumentation & Measurement Technology Conference IMTC 2007*, IEEE, 1–6.

Lynch, Jerome Peter et al. 2004. "Design and Performance Validation of a Wireless Sensing Unit for Structural Monitoring Applications." *Structural Engineering and Mechanics* 17(3–4): 393–408.

MacGregor, James G, Sher Ali Mirza, and B Ellingwood. 1983. "Statistical Analysis of Resistance of Reinforced and Prestressed Concrete Members." In *Journal Proceedings*, 1983, 167–76.

Mander, John B, Michael J N Priestley, and R Park. 1988. "Theoretical Stress-Strain Model for Confined Concrete." *Journal of structural engineering* 114(8): 1804–26.

Masi, Maurizio, D Colella, G Radaelli, and Luca Bertolini. 1997. "Simulation of Chloride Penetration in Cement-Based Materials." *Cement and Concrete Research* 27(10): 1591–1601.

Menegotto, Marco, and P.E. Pinto. 1973. "Method of Analysis for Cyclically Loaded RC Plane Frames Including Changes in Geometry and Non-Elastic Behavior of Elements under Combined Normal Force and Bending." In *Proceeding of IABSE Symposium on Resistance and Ultimate Deformability of Structures Acted on by Well Defined Repeated Loads*, 1973, 15–22.

Monteiro, Paulo J M, and Kimberly E Kurtis. 2003. "Time to Failure for Concrete Exposed to Severe Sulfate Attack." *Cement and Concrete Research* 33(7): 987–93.

Morey, R M. 1974. "Detection of Subsurface Cavities by Ground Penetrating Radar." In *Highway Geological Symposium, Proceedings*, 1974, 28–30.

Mullard, John A, and Mark G Stewart. 2009. "Corrosion-Induced Cover Cracking of RC Structures: New Experimental Data and Predictive Models."

Neville, Adam. 1995. “Chloride Attack of Reinforced Concrete: An Overview.” *Materials and Structures* 28(2): 63–70. https://link.springer.com/article/10.1007/BF02473172 (August 12, 2020).

Neville, Adam M. 1996. “Properties of Concrete. 4th and Final Ed.” *England: Addison Wesley Longman Limited*: 631–33.

Nowak, Andrzej S. 1993. “Live Load Model for Highway Bridges.” *Structural Safety* 13(1–2): 53–66.

Nowak, Andrzej S, Transportation Research Board, and National Research Council. 1999. *Calibration of LRFD Bridge Design Code.* Washington: National Academy Press.

Oh, Byung Hwan, Young Lew, and Young Cheol Choi. 2007. “Realistic Assessment for Safety and Service Life of Reinforced Concrete Decks in Girder Bridges.” *Journal of Bridge Engineering* 12(4): 410–18.

Olhoeft, Gary R. 1984. “Applications and Limitations of Ground Penetrating Radar.” In *SEG Technical Program Expanded Abstracts 1984*, Society of Exploration Geophysicists, 147–48.

Orlando, Luciana, Alessia Pezone, and Alessandro Colucci. 2010. “Modeling and Testing of High-Frequency GPR Data for Evaluation of Structural Deformation.” *NDT & E International* 43(3): 216–30.

Osumi, N, and K Ueno. 1988. “Detection of Buried Plant.” In *IEE Proceedings F (Communications, Radar and Signal Processing)*, IET, 330–42.

Papakonstantinou, K G, and M Shinozuka. 2013. “Probabilistic Model for Steel Corrosion in Reinforced Concrete Structures of Large Dimensions Considering Crack Effects.” *Engineering Structures* 57: 306–26. http://dx.doi.org/10.1016/j.engstruct.2013.06.038 (August 12, 2020).

Park, Robert, and Thomas Paulay. 1975. “Reinforced Concrete Structures.” : xvii, 769 p. : http://www.loc.gov/catdir/toc/onix03/74028156.html (March 15, 2020).

Parmar, D S, and S R Sharp. 2009. “Acoustic Emission for Non-Destructive Testing of Bridges and Other Transportation Infrastructure.” In *Beyond the Crossroads: A National Conference on Transportation Infrastructure & Regulatory Policy; University of Denver*, Denver, CO, USA.

Pérez-Gracia, V. 2016. “Ground Penetrating Radar: Fundamentals, Methodologies and Applications in Structures and Infrastructure.” In *Non-Destructive Techniques for the Evaluation of Structures and Infrastructure*, CRC Press, 135–58.

Pérez-Gracia, V, F García García, and I Rodriguez Abad. 2008. “GPR Evaluation of the Damage Found in the Reinforced Concrete Base of a Block of Flats: A Case Study.” *NDT & e International* 41(5): 341–53.

Pines, Darryll, and A Emin Aktan. 2002. “Status of Structural Health Monitoring of Long-span Bridges in the United States.” *Progress in Structural Engineering and Materials* 4(4): 372–80.

Razaqpur, A G, and O B Isgor. 2009. “Prediction of Reinforcement Corrosion in Concrete Structures.”

Front. Technol. Infrastructures Eng. Struct. Infrastructures 4: 45–69.

Rehman, Sardar Kashif Ur, Zainah Ibrahim, Shazim Ali Memon, and Mohammed Jameel. 2016. "Nondestructive Test Methods for Concrete Bridges: A Review." *Construction and building materials* 107: 58–86.

Saarenketo, Timo, and Tom Scullion. 2000. "Road Evaluation with Ground Penetrating Radar." *Journal of applied geophysics* 43(2–4): 119–38.

Salam, Yaghi. 2014. "Integrated Remote Sensing Technologies for Condition Assessment of Concrete Bridges." https://spectrum.library.concordia.ca/979126/ (March 15, 2020).

Sánchez-Aparicio, Luis Javier et al. 2019. "Non-Destructive Means and Methods for Structural Diagnosis of Masonry Arch Bridges." *Automation in Construction* 104: 360–82.

Sbartaï, Zoubir-Mehdi, Denys Breysse, Mathilde Larget, and Jean-Paul Balayssac. 2012. "Combining NDT Techniques for Improved Evaluation of Concrete Properties." *Cement and Concrete Composites* 34(6): 725–33.

SeismoSoft. 2018. "SeismoStruct 2018 - A Computer Program for Static and Dynamic Nonlinear Analysis of Framed Structures." https://seismosoft.com/.

"SeismoStruct User Manual." 2020: 325. https://seismosoft.com/ (March 15, 2020).

Shaw, M R et al. 2003. "Assessing Bar Size of Steel Reinforcement in Concrete Using Ground Penetrating Radar and Neural Networks." *Insight-Non-Destructive Testing and Condition Monitoring* 45(12): 813–16.

Solla, M, H Lorenzo, A Novo, and J C Caamaño. 2012. "Structural Analysis of the Roman Bibei Bridge (Spain) Based on GPR Data and Numerical Modelling." *Automation in Construction* 22: 334–39.

Stallings, J M, and C H Yoo. 1992. "Analysis of Slab-on-Girder Bridges." *Computers & structures* 45(5–6): 875–80.

Stewart, Mark G., and David V Rosowsky. 1998a. "Structural Safety and Serviceability of Concrete Bridges Subject to Corrosion." *Journal of Infrastructure Systems* 4(4): 146–55.

Stewart, Mark G, and David V Rosowsky. 1998b. "Time-Dependent Reliability of Deteriorating Reinforced Concrete Bridge Decks." *Structural safety* 20(1): 91–109.

Tarussov, Alexander, Marc Vandry, and Aldo De La Haza. 2013. "Condition Assessment of Concrete Structures Using a New Analysis Method: Ground-Penetrating Radar Computer-Assisted Visual Interpretation." *Construction and Building Materials* 38: 1246–54.

Tennyson, R C et al. 2001. "Structural Health Monitoring of Innovative Bridges in Canada with Fiber Optic Sensors." *Smart Materials and Structures* 10(3): 560–73. https://iopscience.iop.org/article/10.1088/0964-1726/10/3/320 (July 8, 2020).

Thakkar, S K, Goutam Ghosh, and Yogendra Singh. 2006. “Structural Damage Identification and Health Monitoring of Bridges.” In *Proc. National Conference on Advances in Bridge Engineering*, 2006, 11–30.

Tixier, Raphaël, and Barzin Mobasher. 2003. “Modeling of Damage in Cement-Based Materials Subjected to External Sulfate Attack. II: Comparison with Experiments.” *Journal of materials in civil engineering* 15(4): 314–22.

Vu, Kim Anh T., and Mark G Stewart. 2000. “Structural Reliability of Concrete Bridges Including Improved Chloride-Induced Corrosion Models.” *Structural Safety* 22(4): 313–33. www.elsevier.nl/locate/strusafe (August 12, 2020).

Vu, Kim, Mark G. Stewart, and John Mullard. 2005. “Corrosion-Induced Cracking: Experimental Data and Predictive Models.” *ACI Structural Journal* 102(5): 719–26.

Wacker, James P, and James Groenier. 2010. “Comparative Analysis of Design Codes for Timber Bridges in Canada, the United States, and Europe.” *Transportation research record* 2200(1): 163–68.

Washer, Glenn A. 1998. “Developments for the Nondestructive Evaluation of Highway Bridges in the USA.” *NDT and E International* 31(4): 245–49.

Weyers, Richard E. 1998. “Service Life Model for Concrete Structures in Chloride Laden Environments.” *Materials Journal* 95(4): 445–53.

Wilson, Justin, and Tzuyang Yu. 2013. “Accelerated Artificial Corrosion Monitoring of Reinforced Concrete Slabs Using the Half-Cell Potential Method.” In *Symposium on the Application of Geophysics to Engineering and Environmental Problems 2013*, Society of Exploration Geophysicists and Environment and Engineering …, 287–94.

Wiwatrojanagul, Pongsak, Raktipong Sahamitmongkol, and Somnuk Tangtermsirikul. 2017. “A New Method to Determine Locations of Rebars and Estimate Cover Thickness of RC Structures Using GPR Data.” *Construction and Building Materials* 140: 257–73.

Wolert, Patryk Jerzy, Marek Karol Kolodziejczyk, James Michael Stallings, and Andrzej S Nowak. 2020. “Nondestructive Testing of a 100-Year-Old Reinforced Concrete Flat Slab Bridge.” *Frontiers in Built Environment* 6: 31.

Xiang, Zhongming, Ge Ou, and Abbas Rashidi. 2020. “An Innovative Approach to Determine Rebar Depth and Size by Comparing GPR Data with a Theoretical Database.” In *Construction Research Congress 2020: Computer Applications*, American Society of Civil Engineers Reston, VA, 86–95.

Yang, Yong et al. 2020. “Small-Scale Void-Size Determination in Reinforced Concrete Using GPR.” *Advances in Civil Engineering* 2020.

Yehia, S, N Qaddoumi, S Farrag, and L Hamzeh. 2014. “Investigation of Concrete Mix Variations and Environmental Conditions on Defect Detection Ability Using GPR.” *NDT & E International* 65: 35–46.

Yehia, Sherif, Osama Abudayyeh, Saleh Nabulsi, and Ikhlas Abdelqader. 2007. "Detection of Common Defects in Concrete Bridge Decks Using Nondestructive Evaluation Techniques." *Journal of Bridge Engineering* 12(2): 215–25.

Yi, Tinghua, Hongnan Li, and Ming Gu. 2010. "Full-Scale Measurements of Dynamic Response of Suspension Bridge Subjected to Environmental Loads Using GPS Technology." *Science China Technological Sciences* 53(2): 469–79. https://link.springer.com/content/pdf/10.1007/s11431-010-0051-2.pdf (July 8, 2020).

Yu, Tzuyang, and Sanjana Vinayaka. 2020. "Quantification of Surface Crack Depth in Concrete Panels Using 1.6 GHz GPR Images." In *Nondestructive Characterization and Monitoring of Advanced Materials, Aerospace, Civil Infrastructure, and Transportation IX*, eds. Peter J. Shull, Tzu-Yang Yu, Andrew L. Gyekenyesi, and H. Felix Wu. SPIE, 6. https://www.spiedigitallibrary.org/conference-proceedings-of-spie/11380/2558952/Quantification-of-surface-crack-depth-in-concrete-panels-using-16/10.1117/12.2558952.full (July 8, 2020).

Yuan, Yingshu, Yongsheng Ji, and Surendra P Shah. 2007. "Comparison of Two Accelerated Corrosion Techniques for Concrete Structures." *ACI Structural Journal* 104(3): 344.

Zaki, A, Y Jusman, M A M Johari, and WMAW Hussin. 2020. "Image Processing for Corrosion Quantification in Concrete Slabs Using GPR Data." In *Journal of Physics: Conference Series*, IOP Publishing, 12049.

Zaki, Ahmad, Megat Azmi Megat Johari, Wan Muhd Aminuddin Wan Hussin, and Yessi Jusman. 2018. "Experimental Assessment of Rebar Corrosion in Concrete Slab Using Ground Penetrating Radar (GPR)." *International Journal of Corrosion* 2018.

Zimmerman, David C, and Mohammed Kaouk. 1994. "Structural Damage Detection Using a Minimum Rank Update Theory."

Appendix A: Plastic Hinge Calculations

The plastic hinge calculations for the internal girder of a new bridge are given below:

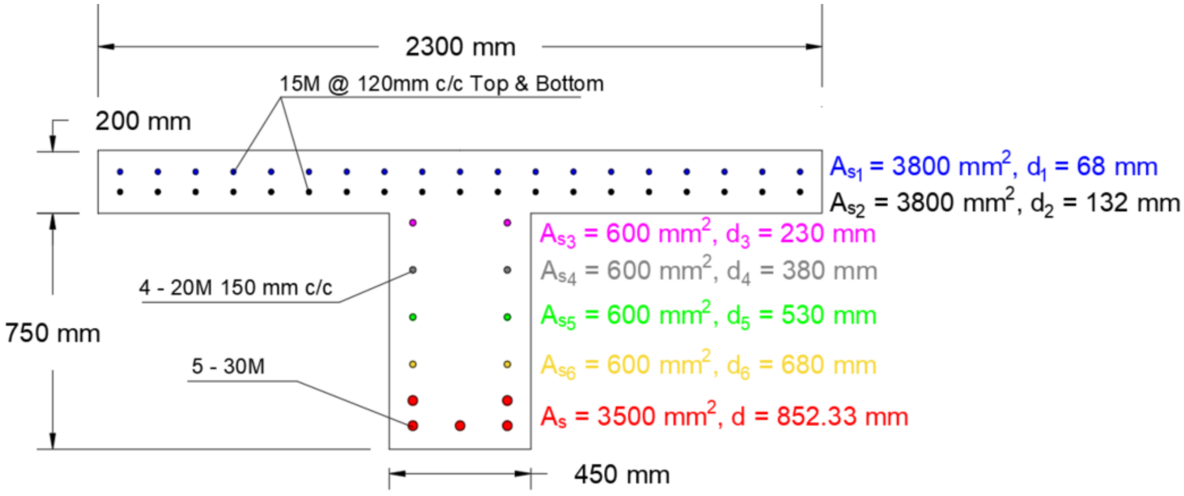

Internal Girder of New Bridge

- ***Reinforcement Properties***

Yield strength of Reinforcement steel, f_y = 400 MPa

Modulus of elasticity of steel, E_s = 200000 MPa

Reinforcement Details

Location	Area of Rebar (mm^2)	Depth from Top (mm)
Top Rebars in Deck	3800	68
Bottom Rebars in Deck	3800	132
1st Layer Side Face Rebars in Web	600	230
2nd Layer Side Face Rebars in Web	600	380
3rd Layer Side Face Rebars in Web	600	530
4th Layer Side Face Rebars in Web	600	680
Bottom Rebars in Beam	3500	852.33

- ***Concrete Properties***

Compression strength of concrete, f_c' = 40 MPa

Concrete mass density, γ_c = 2400 kg/m^3

Modulus of elasticity of concrete (As per CHBDC-S6 2014),

$$E_c = \left(3000 \times \sqrt{f_c'} + 6900\right) \times \left(\frac{\gamma_c}{2300}\right)^{1.5} = 27579.29 \text{ MPa}$$

Section Properties

Flange width, $b_f = 2300$ mm

Beam thickness, $b_w = 450$ mm

Slab thickness, $h_f = 200$ mm

Total height of the section, h = 950 mm

All concrete covers, c = 60 mm thick.

Modular Ration, $n = E_s/E_c = 7.25$

I. Cracking Moment and Curvature

The geometric centroid of the section from the top,

$$\bar{y} = \frac{b_f \cdot \frac{h_f^2}{2} + b_w \cdot (h-h_f) \cdot \frac{\{h_f + (h-h_f)\}}{2}}{b_f \cdot h_f + (h-h_f) \cdot b_w} = 301.02 \text{ mm}$$

The gross moment of inertia,

$$I_g = b_f \cdot \frac{h_f^3}{12} + b_f \cdot h_f \cdot \left(\bar{y} - \left(\frac{h_f}{2}\right)\right)^2 + \frac{b_w \cdot (h-h_f)^3}{12} + b_w \cdot (h-h_f) \cdot \left[\left(h_f + \frac{(h-h_f)}{2}\right) - \bar{y}\right]^2$$

$$\therefore I_g = 61.276 \times 10^9 \, mm^4$$

Stress in concrete at cracking, $f_{cr} = 0.4\sqrt{f_c'} = 2.53\,MPa$

The Cracking Moment of the section,

$$M_{cr} = \frac{f_{cr} \cdot I_g}{h - \bar{y}} = 238.86\, kN \cdot m$$

The Cracking Curvature, $\psi_{cr} = \frac{f_{cr}}{E_c \cdot (h - \bar{y})} = 1.413 \times 10^{-4}$ rad/m

II. Yield Moment and Curvature

For k_d = depth of neutral axis at yielding

Force in main steel $F_s = A_s \cdot f_y$

Strain in concrete, $\varepsilon_c = \frac{f_y}{E_s} \cdot \frac{k_d}{(d - k_d)}$

Force in steel $F_{si} = A_{si} \cdot \sigma_{si} = f_y \cdot \left|\frac{d_i - k_d}{d - k_d}\right|$ where i={1,2,3,4,5,6}

At Equilibrium compression equals tension:

For $k_d < h_f$ then,

$0.5 \cdot \varepsilon_c \cdot E_c \cdot k_d \cdot b_f = F_{s1} + F_{s2} + F_{s3} + F_{s4} + F_{s5} + F_{s6} + F_s$

Calculating k_d from excel sheet using goal seek, $k_d = 137.16$ mm $< h_f$, hence the neutral axis lies in the flange of the beam.

Taking moment about the bottom reinforcement the yielding moment of the section is:

$$M_y = \frac{f_c' \cdot k_d \cdot b_f \cdot \left(d - \left(\frac{k_d}{3}\right)\right)}{2} - \sum_{i=1}^{6} F_{s1} \cdot (\mathrm{d} - d_i) = 1431.36\ \mathrm{kN \cdot m}$$

Yielding Curvature, $\psi_y = \frac{f_y}{\left(\frac{E_s}{d - k_d}\right)} = 2.796 \times 10^{-3}$ rad/m

III. Ultimate Moment and Curvature

$$\propto_1 = 0.85 - 0.0015 \cdot f_c' = 0.79$$

$$\beta_1 = 0.97 - 0.0025 \cdot f_c' = 0.87$$

If the height of the compression zone is C,

Strain in steel, $\sigma_i = E_s \cdot \varepsilon_i = E_s \cdot \left|\frac{0.0035 \cdot (d_i - C)}{C}\right|$

If $\sigma_i < f_y$ then force in steel $F_i = A_{si} \cdot \sigma_i$ and if $\sigma_i > f_y$ then force in steel $F_i = A_{si} \cdot f_y$ where i={1,2,3,4,5,6}

The value of C can be found from the equilibrium:

$$\alpha_1 * \beta_1 * f_c' * C * b_f = F_1 + F_2 + F_3 + F_4 + F_5 + F_6 + F$$

Calculating C from excel sheet using goal seek, C = 60.80 mm

$$a = \beta_1 \cdot C$$

The ultimate moment capacity of the section is:

$$M_u = \propto_1 \cdot f_c' \cdot a \cdot b_f \left(d - \frac{a}{2}\right) - \sum_{i=1}^{6} F_{si} \cdot (\mathrm{d} - d_i) = 1916.65\ \mathrm{kN \cdot m}$$

Ultimate Curvature, $\psi_u = \frac{0.0035}{C} = 5.756 \times 10^{-2}$ rad/m

Appendix B: Conversion of Trilinear Moment Curvature Relationship to Bilinear

The bilinear representation of the Moment-Curvature relation is derived from the tri-linear curve where both the representations indicate an equal amount of absorbed energy. The yielding moment is kept the same while the new yielding curvature is calculated.

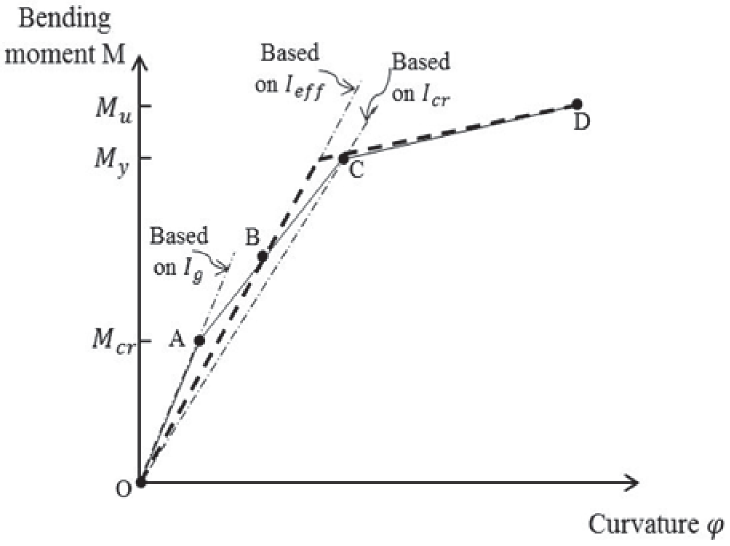

Figure *Idealized Bilinear and Trilinear Moment-curvature Relation (Ghodoosipoor 2013)*

Area Under Bilinear Moment-Curvature Curve = Area Under Trilinear Moment-Curvature Curve

$$\therefore\ \frac{1}{2}\cdot M_y \cdot \Psi_{y(new)} + \frac{1}{2}\cdot \left(M_u + M_y\right)\cdot\left(\Psi_u - \Psi_{y(new)}\right)$$

$$= \frac{1}{2}\cdot \Psi_{cr}\cdot M_{cr} + \frac{1}{2}\cdot (M_y + M_{cr})\cdot(\Psi_y - \Psi_{cr}) + \frac{1}{2}\cdot(M_u + M_y)\cdot(\Psi_u - \Psi_y)$$

$$\therefore\ \Psi_{y(new)} = 2.55 \times 10^{-3}\ rad/m$$

Appendix C: Calculation for Chloride Induced Corrosion Initiation and Rebar Area

Corrosion Initiation Time

For the calculation of the corrosion initiation period, Equation 2.2 is used.

Threshold chloride content, $C_{th} = C(x,t) = 0.71$ kg/m^3

Surface chloride content, $C_s = 8.8$ kg/m^3

Chloride diffusion coefficient, $D_c = 84$ mm^2/year

Depth of concentration i.e., the reinforcement cover depth, $x = 60$ mm

For these values, the time t equals the time of initiation of corrosion T_i.

Solving equation 2.2

$$C(x,t) = C_s\left[1 - erf\left(\frac{x}{2\sqrt{t\,D_c}}\right)\right]$$

$\therefore T_i = 7.34$ years

The Calculation for Rebar Area with Time

Where D_i is the initial bar diameter,

The corrosion current density $i_{corr} = 1.5$ µA/cm^2

Corrosion rate at the surface of rebar $\lambda \approx 0.0116 \bullet i_{corr}$ mm/year = 0.0174 mm/year.

$$D_t = \begin{cases} D_i & ; t \le T_i \\ D_i - 2\lambda(t - T_i) & ;\ T_i \le t \le T_i + \left(\frac{D_i}{2\lambda}\right) \\ 0 & ; t > T_i + \left(\frac{D_i}{2\lambda}\right) \end{cases}$$

Rebar	At life t =0 year		At life t = 45 year $D_t = D_i - 2\lambda(t - T_i)$	
	D_i (mm)	Area (mm^2)	D_t (mm)	Area (mm^2)
15M	16	200	14.69	169.47
20M	19.5	300	18.19	259.85
30M	29.9	700	28.59	641.95